DEVELOPMENT OF A MULTISCALE NUMERICAL MODEL WITH TWO HUMAN PULMONARY HEALTH APPLICATIONS

By

AHMADREZA HAGHNEGAHDAR
Bachelor of Science in Chemical Engineering
Shiraz University
Shiraz, Iran
2015

Submitted to the Faculty of the
Graduate College of
Oklahoma State University
in partial fulfillment of
the requirements for
the Degree of
MASTER OF SCIENCE
December 2018

DEVELOPMENT OF A MULTISCALE NUMERICAL MODEL WITH TWO HUMAN PULMONARY HEALTH APPLICATIONS

Thesis Approved:

Dr. Yu Feng

Thesis Advisor

Dr. Ashlee N. Ford Versypt

Dr. Arvind Santhanakrishnan

ACKNOWLEDGMENTS

The research presented in this report would not have been possible without the professional guidance, mentorship, and training of my advisor, Dr. Yu Feng. His unwavering support allowed me to pursue my interests and I appreciate the trust and encouragement he offered with his dedicated supervision. I am thankful to my thesis committee, Dr. Ford Versypt and Dr. Santhanakrishnan, as their guidance and support have been a backbone of this research.

None of this would have been possible without the love and support of my friends and family, especially my parents and my best friend Fermiko.

Name: AHMADREZA HAGHNEGAHDAR

Date of Degree: December 2018

Title of Study: DEVELOPMENT OF A MULTISCALE NUMERICAL MODEL WITH TWO HUMAN PULMONARY HEALTH APPLICATIONS

Major Field: CHEMICAL ENGINEERING

Abstract: Determination of the site-specific dosimetry and clearance of deposited aerosols in the human airways is critical in health risk assessment studies such as toxicant exposure evaluation and inhaled medication delivery with pulmonary topical or systemic actions. However, comprehensive evaluation still lacks informative data, i.e., high-resolution local dosimetry of inhaled aerosols in airways and systemic regions, due to the limited imaging resolutions, restricted operational flexibilities, and invasive nature of experimental and clinical examinations. Computational simulations, on the other hand, can provide a detailed explanation for the chemical dynamics in the respiratory system, intrapulmonary and extrapulmonary tissues, and systemic regions using multiscale platforms. In this study, two experimentally validated multiscale numerical analyses were developed for the post-deposition calculation of the respirable aerosols, which expands the application of mathematical models in the respiratory system to the health endpoint. First, computational fluid-particle dynamics (CFPD) is coupled with a physiologically based toxicokinetic (PBTK) model to predict the in tissue translocation and systemic disposition of inhaled volatile organic compound and toxicant constituents in an electronic cigarette (EC). The proposed framework can be used as a benchmark to identify drug or toxicant dynamics in the human body, significantly applicable in the fields of pharmacokinetics and toxicokinetics. Second, an epidemiological computational approach was programmed and optimized by connecting CFPD and host cell dynamics (HCD) models to simulate the transport and deposition of low-strain influenza A virus (IAV)-laden droplets in subject-specific human lung airways and to predict the regional responses of targeted host cells to IAV infection. Furthermore, the hygroscopic growth and shrinkage of multicomponent droplets were considered by examining the thermodynamic equilibrium between the phases. These frameworks overcome the limitation of the experimental studies by connecting levels of biological dynamics that are not measurable using clinical studies. The influence of repetitive exposure incidents on the post-deposition dynamics was determined, which is valuable for assessing the chronic health effects of inhaled airborne particles.

TABLE OF CONTENTS

Chapter Page

LIST OF TABLES

LIST OF FIGURES

NOMENCLATURE

$\dot{m}_d^0$	initial mass flow rate of discrete phase
$\overline{V}_s$	partial molar volume of solute
$\underline{A}$	antibodies
$\underline{B}$	B cell
$\underline{D}_M$	dendritic cell
$\underline{F}$	interferons
$\underline{I}$	infected cell
$\underline{R}$	refractory cell
$\underline{T}_C$	CD8+ T cell
$\underline{T}_H$	CD4+ T cell
$\underline{T}_T$	epithelial cell
$\underline{V}$	viral titer
$\vec{G}$	Gaussian random numbers
ξ_i	average face-cell centroid gradient obtained from the previous time step
A_d	droplet surface
A_f	surface area of the mesh element face
A_i	normal vector of the mesh element face
A_R	region surface area
C_C	Cunningham correction factor
C_D	drag force coefficient
C_d	cross-diffusion term
c_p	gas mixture specific heat
C_T	species concentration in the compartment outlet
$C_{p,u,s}$	uptake concentration in particle phase
$C_{s,t}$	tissue concentration
$C_{T,in}$	species concentration in the compartment inlet
C_{uptake}	total uptake concentration
$C_{V,u,s}$	vapor species uptake concentration
D_s^m	molecular diffusivity
d_d^V	mass equivalent droplet diameter
d_p	particle diameter
D_t	turbulent diffusivity
$D_{a,s}$	binary diffusivity of species in the air

$D_{s,b}$	diffusion coefficient in the subepithelium (blood) layer
$D_{s,t}$	diffusion coefficient in the tissue layer
$D_{w,s}$	diffusivity of the species in mucus layers
DE	deposition efficiency
de_{ij}	deformation rate tensor
DF	deposition fraction
dV	local control volume
e_i	cell-to-face centroid unit normal vector
$F_{p,i}^{D}$	drag force
$F_{p,i}^{G}$	gravity force
$F_{p,i}^{L}$	Saffman lift force
$F_{p,i}^{BM}$	Brownian motion induced force
$f_{R,V,s}$	regional bioavailability factor
G	generation of the κ
g_i	body accelerations acting on the continuum
h_i	sensible enthalpy
H_{lat}	latent heat of energy exchange between the phases
IC_H	intrinsic hepatic clearance
IC_R	intrinsic renal clearance
J_s	mass diffusion flux
k_B	Boltzmann constant
k_c	gas mixture conductivity
$k_{c,t}$	gas mixture turbulent thermal conductivity
K_{hc}	heat transfer coefficient
K_{mc}	mass transfer coefficient
$k_{s,f}$ and $k_{s,b}$	first order reaction constants
Kn	Knudsen number
m_d^0	mass of the injected discrete phase
m_p	particle mass
MW_s	molecular weight
$N_{d/parcel}$	number of droplets at each parcel
Nu	Nusselt number
p	pressure
$P^0(T)$	saturation vapor pressure
P_T	compartment partition coefficient
P_{bt}	blood-tissue partition coefficient
$P_{s,S}$	vapor pressure at the droplet surface
P_{ta}	tissue-air partition coefficient
Pr_t	turbulent Prandtl number
Q_T	compartment flow rate
R	universal gas constant
r_{cf}	cell-to-face centroid distance
Re_d	droplet Reynolds number
S_s^m	mass source term
S^T	volumetric energy source term

S_0	spectral intensity
S_f	control volume face surface
Sc_t	turbulent Schmidt numbe
Sh	Sherwood number
T	gas mixture temperature
t_d	unsteady discrete phase tracking time
t_f	continuous fluid time step
T_p	particle temperature
u_i	i-th component of the continuous phase velocity
u_i^d	droplet velocity components
$u_{p,i}$	i-th component of the particle velocity
V_T	compartment volume
$V_{s,max1}$, $K_{s,m1}$, $V_{s,max2}$, $K_{s,m2}$	saturable metabolism constants
x_i	direction component
Y	dissipation of the κ
Y_s	mass fraction of species
$Y_{s,\infty}$	mass fraction in the systemic region
$Y_{s,c}$	mass fraction on the local mesh cell
$Y_{s,f}$	mass fraction on the face centroid
$Y_{s,R}$	regional area weighted average mass fraction
$Y_{s,S}$	mass fraction at the droplet surface
z_m	mucus layer thickness
$\tilde{m}_{d,NaCl}$	molality of the solution

Subscripts/Superscripts

M	metabolizing sites
R	region
s	species
T	tissue

Greek Symbols

α_m	mass accommodation coefficient
γ_s	activity coefficient
κ	turbulence kinetic energy
λ	mean free path
$\mathcal{H}_{c,s}$	Henry's constant
μ	gas mixture mixture viscosity
μ_t	turbulent viscosity
$\mu_{d,S}$	gas mixture viscosity at the droplet surface temperature
ω	specific rate of the dissipation
$\Phi_{d,s}$	molal osmotic coefficient of the solute
Φ_{vd}	gas mixture viscous dissipation
ρ	gas mixture density
ρ_d	droplet density
σ_d	surface tension
$\vartheta_{d,s}$	stoichiometric dissociation number of the solute

PREFACE

Chapter I has been presented at the 5th International Conference on Computational and Mathematical Biomedical Engineering (2017) and has been published as: Haghnegahdar, A., Feng, Y., Chen, X., & Lin, J. (2018). Computational analysis of deposition and translocation of inhaled nicotine and acrolein in the human body with e-cigarette puffing topographies. Aerosol Science and Technology, 52(5), 483-493.

Chapter II has been presented at 2018 Biomedical Engineering Society (BMES) annual meeting and has been submitted to Journal of Aerosol Science and is currently under revision as: Haghnegahdar, A., Feng, Y. Deposition and Replication of Low-Strain Influenza A Virus in the Epithelium of a Subject-Specific Virtual Human Upper Airway Model.

CHAPTER I

Computational Analysis of Deposition and Translocation of Inhaled Nicotine and Acrolein in the Human Body with E-cigarette Puffing Topographies

1.1 Introduction

Electronic cigarettes (ECs), perceived as the safer alternatives to conventional cigarettes, are manufactured in a wide variety of designs with different nicotine concentrations and added flavors. Other components such as glycerol (VG) and propylene glycol (PG) exist in EC to imitate smoke *via* vaporization instead of combustion (Allen et al., 2016). Although studies showed that some e-cigarette products have immediate adverse physiological effects after short-term uses (e.g., an increase in impedance, peripheral airway flow resistance, and oxidative stress among healthy smokers who used an EC for 5 minutes (Alfi and Talbot, 2013)), the long-term health effects are still unknown and needed for further investigations. Recently, toxicants such as formaldehyde, acetaldehyde, acrolein, diacetyl, benzaldehyde, and vanillin were also detected in e-cigarette aerosols (Goniewicz et al., 2014; Allen et al., 2016). These toxicants are either generated by the low-level thermal degradation or exist in flavorings. Because of the potential health impact of the newly discovered chemical compounds listed above (Alarcon, 1976; De Woskin et al., 2003; Wang et al., 2008; Mishra et al., 2015; Morris et al., 2015; Abraham et al., 2011), it is imperative to conduct research and provide sufficient quantitative evidence to address the potential health risks for the optimization of e-cigarette product design or facilitate regulatory approval. Thus, it is critical to define reliable biomarkers and understand how those chemical compounds transport, translocate and accumulate in the human body. However, it is still a lack of informative data, i.e., high-resolution local dosimetry of inhaled aerosols in lung airways and other systemic regions. The knowledge and data gap are mainly due to the limited imaging resolutions, restricted operational flexibilities, and invasive nature of experimental and clinical studies. Indeed, since ECs have not been in widespread use sufficiently long, the human exposure studies until now are limited to very short-term health responses. Meanwhile, although animal studies were performed to investigate the health effects on mice and rats due to the exposure to EC aerosols, observations are very restrictive regarding imaging resolution and operational flexibility (Morris et al., 2015).

As an alternative, *in silico* study using high-fidelity numerical methods, i.e., Computational Fluid-Particle Dynamics (CFPD) plus Physiologically Based Toxicokinetic (PBTK) model (see Figure 1.1), are capable of providing valuable dosimetry data of multicomponent EC aerosols in subject-specific respiratory tracts (Chen et al., 2017; Haghnegahdar and Feng, 2017; Kleinstreuer and Feng, 2013). Furthermore, a high-quality CFPD-PBTK model is also a promising whole-body dosimetry prediction tool, which is noninvasive, cost-effective, and time-saving compared to*in vitro* and *in vivo* investigations. Compared to those lumped parameter approaches and semi-empirical models, the CFPD-PBTK model is developed based on the natural law of physics and chemistry with fewer assumptions and simplifications. Thus, an advanced noninvasive, reliable, and generalized engineering tool based on the multiscale CFPD-PBTK framework is developed and employed in this study to analyze the comparative health risk reductions of EC aerosol components, i.e., nicotine and acrolein, with different puffing topographies. This *in silico* study has relevance to public health because it will enable a major health question to be answered by simulations in a short period, i.e., what is the relationship between the chronic passive e-cigarette vaping of adolescents and their health risks. The integration of multiple disciplinary types of research will bridge the gap of EC aerosol exposure and cardiopulmonary health effect assessments, leading ultimately to a better understanding of the complexity and dynamics of EC aerosol transport, deposition and translocation in human bodies.

Efforts have been made towards the development of numerical models to predict the fates of inhaled tobacco products. The fundamental approaches to have a reliable model that can represent the essential governing physics are presented in the review by Kleinstreuer and Feng (2013). Simulations of the EC generated aerosol with the multipath particle deposition model (MMPD) approach developed by Manigrasso et al. (2015). The connection of the CFPD and the PBTK demands additional description that can present the rule of the interconnecting tissue layer. Kimbell et al. (1993) has completed the single-phase formaldehyde transport in Fisher rat nasal cavity. In this work, the complete water solubility of the formaldehyde led them to consider the zero concentration condition at the airway walls, and consequently, the diffusion process was uncoupled from those in the surrounding tissues. Deposition and mucosa layer translocation of vapor in the nasal cavity with hybrid CFD-PBTK simulations were studied by Morris et al. (1993). Bush et al. (1998) simulated non-reactive vapors uptake in the rat nasal cavity by including compartmental designs for respired air, the mucus layer, the epithelial cell layer, and the sub-epithelial layer containing blood vessels. Corley et al. (2015, 2012) have reported the connected CFD and PBTK model for a single vapor phase deposition of the cigarette constituent in the respiratory system of rat, monkey, and human considering mucus, epithelial, and submucosal layers with diffusion and associated reactions.

In this study, the new multiscale CFPD-PBTK model is developed and employed to predict the local fates of nicotine and acrolein from entering the human upper airways to the systemic regions. Since generated EC aerosol composition varies due to different puffing behaviors and EC products (Lisko et al., 2015). Hence, the parametric analysis of puff pattern influence on transport and translocation dynamics is

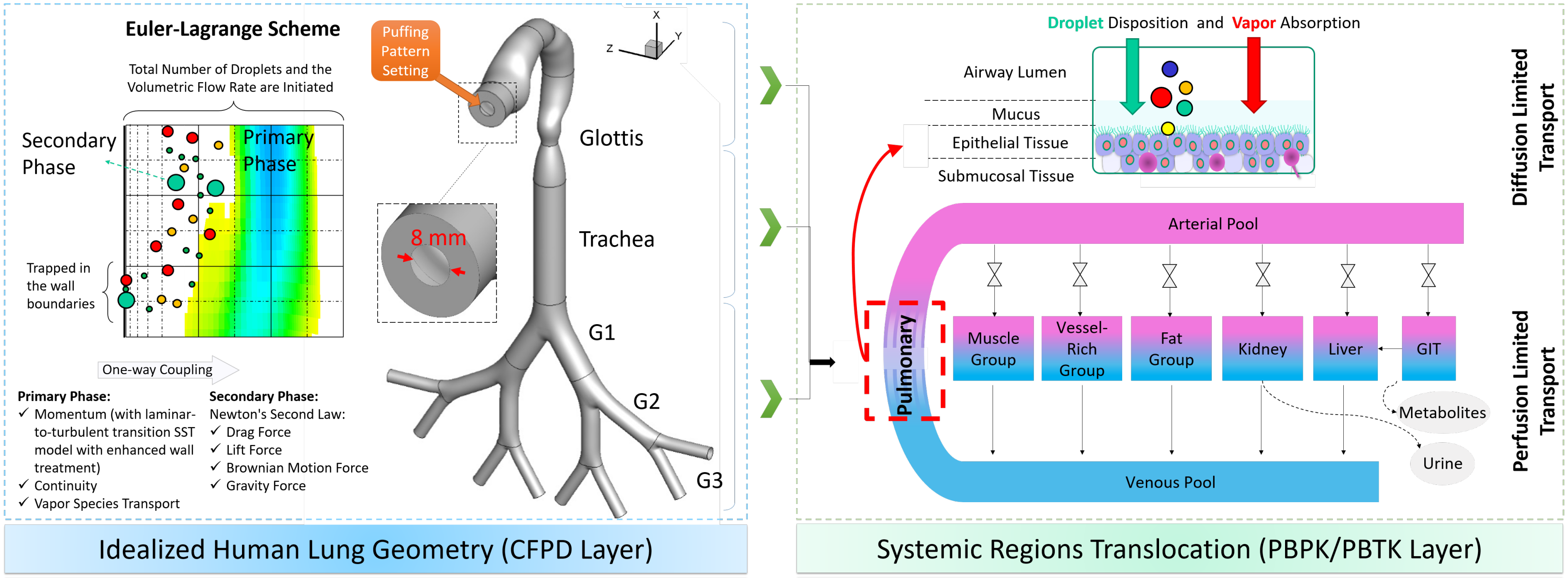

Figure 1.1: Framework of the CFPD-PBTK model.

performed for individualized health risk assessments. EC Puffing topographies were selected as inlet conditions based on existing investigations and standards (Cobb et al., 2010; Goniewicz et al., 2014, 2017; Shahab et al., 2017). Simulations of multiple puffs with holdings are enabled and performed for the first time using the CFPD-PBTK model.

The layout of this chapter is as follow: Section 1.2 introduces the framework of the multiscale CFPD-PBTK model followed by the numerical setup, mesh independence tests, and model validations. Section 1.6 contains the numerical results of multi-component EC aerosol transport, deposition, and translocation with insightful discussion and parametric analysis. Section 1.7 summarizes the findings of the present study. Section 1.9 proposes future work to improve the generalized feasibility of the CFPD-PBTK modeling framework.

1.2 Methodology

Governed by the conservation laws of nature, the Computational Fluid-Particle Dynamics (CFPD) and Physiologically Based Toxicokinetic (PBTK) model is a promising tool to assess the chronic exposure risks of EC aerosols and provide informative and high-resolution data promptly. The schematic of the CFPD-PBTK modeling framework is shown in Figure 1.1. Integrating the multiscale model validations and optimizations, the CFPD-PBTK model provides local information about how different levels of puffing may affect the deposition and translocation of toxicants in both lung and systemic regions. The CFPD model is developed based on Euler-Lagrange scheme (Feng et al., 2016) specifically for multi-component EC aerosol dynamics in an idealized human upper airway model from mouth to Generation 3 (G3). The existence of the dominant chemicals of the nicotine, acrolein, formaldehyde, vegetable glycerin (VG), and propylene glycol (PG) are tracked both in the particle and vapor forms. Also, the wall of the respiratory system is considered as a sink with fractional to complete absorption for the uptake of the chemicals into the systemic regions. The PBTK model for inhaled toxicants is developed and validated. It is assumed that the toxicant‘s distribution through blood flow with the biological structure of tissues which are homogeneous rate-limited diffusion (Robinson et al., 1992). The important mechanisms including absorption, distribution, metabolism, and excretion in each organ for each toxicant are considered. Physiologic parameters (cardiac output, ventilation rate, blood flow rate to the organs and organ volumes) are obtained and optimized accordingly. The system of governing equations and boundary conditions are evaluated based on the literature review and are provided in the following.

1.3 Governing Equations

1.3.1 Computational Fluid-Particle Dynamics (CFPD)

1.3.1.1 Air-Vapor Mixture

Assuming EC vapor species are diluted suspensions in the air, the air-vapor mixture can be modeled as a single continuous phase. Neglecting the evaporation effects of EC droplets, the governing equations of the air-aerosol mixture can be given as

$$\frac{\partial u_i}{\partial x_i} = 0 \tag{1.1}$$

in which u_i represents the i-th component of the continuous phase velocity.

$$\rho(\frac{\partial u_i}{\partial t} + u_j \frac{\partial u_i}{\partial x_j}) = -\frac{\partial p}{\partial x_i} + \frac{\partial}{\partial x_j}\left[(\mu + \mu_t)\frac{\partial u_i}{\partial x_j}\frac{\partial u_j}{\partial x_i}\right] + \rho g_i \tag{1.2}$$

where ρ and μ are the air-vapor mixture density and viscosity respectively. At typical puffing flow rates, airflow through the oral airway region and first few generations is incipient turbulent, becoming laminar again from G1 to G3. Therefore, the shear stress transport (SST) transition model (Menter et al., 2006a,b; Langtry and Menter,

2009) is adapted in this study, based on its overall good performance on the prediction of laminar-to-turbulent transition onset, computational efficiency, and reasonable accuracy when compared to large eddy simulation (LES). Based on the $k-\omega$ model, the SST transition model can be described as follows

$$\frac{\partial}{\partial t}(\rho\kappa)+\frac{\partial}{\partial x_i}(\rho u_i\kappa)=\frac{\partial}{\partial x_i}((\mu+\mu_t/\sigma_\kappa)\frac{\partial\kappa}{\partial x_i})+\tilde{G_\kappa}-Y_\kappa \tag{1.3}$$

$$\frac{\partial}{\partial t}(\rho\omega)+\frac{\partial}{\partial x_i}(\rho u_i\omega)=\frac{\partial}{\partial x_i}((\mu+\mu_t/\sigma_\omega)\frac{\partial\omega}{\partial x_i})+G_\omega-Y_\omega+Cd_\omega \tag{1.4}$$

$$\frac{\partial}{\partial t}(\rho\gamma)+\frac{\partial}{\partial x_i}(\rho u_i\gamma)=\frac{\partial}{\partial x_i}((\mu+\mu_t/\sigma_f)\frac{\partial\gamma}{\partial x_i})+G_\gamma-Y_\gamma \tag{1.5}$$

$$\frac{\partial}{\partial t}(\rho\widetilde{Re}_{\theta t})+\frac{\partial}{\partial x_i}(\rho u_i\widetilde{Re}_{\theta t})=\frac{\partial}{\partial x_i}(\sigma_{\theta t}(\mu+\mu_t)\frac{\partial\widetilde{Re}_{\theta t}}{\partial x_i})+G_{\theta t} \tag{1.6}$$

In Eqs. (1.3-1.6), G and Y represent generation and dissipation of the turbulence kinetic energy (κ) and the specific rate of the dissipation (ω). C_d parameter shows the cross-diffusion term, and σ is the Prandtl number. Also, the μ_t is the turbulent viscosity. The transported Reynolds number ($\widetilde{Re}_{\theta t}$) in Eq. (1.6) is used to find the intermittency generation term in Eq. (1.5).

1.3.1.2 Multi-component EC Particles

In this study, the one-way coupled Euler-Lagrange method is employed to predict the transport of inhaled EC particles (Feng et al., 2016). Due to the relatively small size of the particles, rotational motions are neglected. Particle diameter changes due to condensation, evaporation, or coagulation are not considered. The translation equation of particles can be given as

$$m_p \frac{du_{p,i}}{dt} = F^D_{p,i} + F^L_{p,i} + F^{BM}_{p,i} + F^G_{p,i} \tag{1.7}$$

where $F^D_{p,i}$, $F^L_{p,i}$, $F^{BM}_{p,i}$ and $F^G_{p,i}$ are drag force, Saffman lift force, Brownian motion induced force, and gravity. Basset force is neglected due to negligible size of particles compared to the fluid flow domain. Specifically, the drag force can be given as

$$\vec{F}^D_{p,i} = \frac{1}{8}\pi\rho(u_i - u_{p,i})\left|u_i - u_{p,i}\right| d_p^2 C_D / C_C \tag{1.8}$$

$$C_D = \frac{24}{Re_p}(1 + 0.15Re_p^{0.687}) \tag{1.9}$$

in which d_p is the particle diameter. In Eq. (1.9), C_D is the drag force coefficient. C_C is the Cunningham correction factor (Allen and Raabe, 1985) which is defined as

$$C_C = 1 = \frac{2\lambda}{d_p}(1.257 + 0.4e^{-1.1\frac{d_p}{2\lambda}}) \tag{1.10}$$

where $\lambda = 65$ nm represents the air mean free path. As long as the particle's diameter compared to the characteristic length of the continuous phase domain is significantly small, the particle Reynolds number Re_p based on the difference between the particle and the airflow velocity is small enough, and the Saffman lift force can be calculated by expression given by Li and Ahmadi (1992)

$$\vec{F}^L_{p,i} = \frac{2Kde_{ij}nu^{1/2}}{(\rho_p/\rho)d_p(de_{lk}de_{kl})^{1/4}}(\vec{u} - \vec{u}_p) \tag{1.11}$$

In Eq. (1.11), de_{ij} is the deformation rate tensor (Drew, 1976). K is the constant coefficient of Saffman‘s lift force equal to 2.594.

Employing the Gaussian white noise process model provided by Li and Ahmadi

(1992), The Brownian motion induced force is expressed as

$$\vec{F}_{p,i}^{BM} = \vec{G}\sqrt{\frac{\pi S_0}{\Delta t}} \tag{1.12}$$

$$S_0 = \frac{216\nu k_B T_p}{\pi^2 \rho d_p^5 (\frac{\rho_p}{\rho})^2 C_C} \tag{1.13}$$

In Eq. (1.12), $\vec{G}$ is a three dimensional vector consisting of three independent zero-mean, unit-variance Gaussian random numbers ranging from 0 to 1. In Eq. (1.13), S_0 is the spectral intensity, k_B is Boltzmann constant (1.38×10^{-23} J/K) and T_p is temperature which is equal to constant value of 310.15 K in this study.

For the simulation process, as suggested by Gupta and Peters (1985) the particle time step Δt_p should be larger than the time step needed for the particle and fluid molecules collision and smaller than relaxation time for interaction and external forces. Thus, Δt_p can be estimated using the following equation

$$\Delta t_p = (\frac{3\pi\mu d_p}{C_C m_p})^{-1} \tag{1.14}$$

The regional deposition of particles in human airways can be quantified using deposition fraction (DF) and deposition efficiency (DE), which are defined as

$$DF = \frac{Number\ of\ regional\ deposited\ particles}{Number\ of\ particles\ entering\ the\ mouth} \tag{1.15}$$

$$DE = \frac{Number\ of\ regional\ deposited\ particles}{Number\ of\ particles\ entering\ the\ region} \tag{1.16}$$

The deposition on the lung airway walls was considered to happen when the distance between the particle centroid and the airway wall is less than $d_p/2$.

1.3.1.3 Convection-Diffusion Equations for EC Vapor Species

The convection-diffusion equations are introduced for those EC chemical compounds in vapor forms to describe the transport dynamics by tracking the material mass fractions in human respiratory systems. The generalized equation can be given as

$$\frac{\partial Y_s}{\partial t} + \frac{\partial (u_i Y_s)}{\partial x_i} = \frac{\partial}{\partial x_i}(D_{a,s}\frac{\partial Y_s}{\partial x_i}) \tag{1.17}$$

where Y_s is the mass fraction of species s and $D_{a,s}$ is the binary diffusivity of species s in the air. The mixed boundary condition is developed for a more realistic vapor absorption boundary condition at airway walls, i.e.,

$$\int_f \frac{\partial Y_{s,c}}{\partial x_i}\, dS_f = \int_f \psi_s (Y_{s,f} - Y_{s,\infty})\, dS_f \tag{1.18}$$

in which $Y_{s,c}$ and $Y_{s,f}$ are the mass fraction of the species s on the local mesh cell and face centroid respectively and S_f is the control volume face surface (see Figure 1.2). $Y_{s,\infty}$ is the mass fraction of the species in the systemic region which is assumed to be zero at initial condition as long as the reaction of the acrolein and formaldehyde are suggested to be high at the first contacting site (ATSDR, 2007). The absorption coefficient ψ_s is defined as

$$\psi_s = \frac{D_{w,s}}{D_{a,s}\mathcal{H}_{c,s} z_m} \tag{1.19}$$

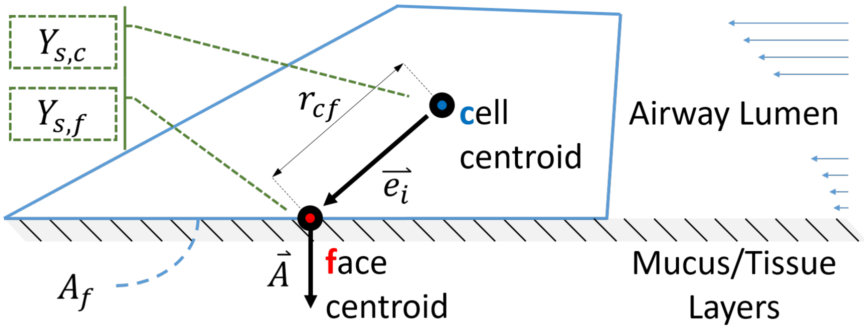

Figure 1.2: Implementation of the third-type boundary condition for species absorption at airway walls.

where $D_{w,s}$ and $\mathcal{H}_{c,s}$ denote the diffusivity of the species in mucus layers and the Henry's constant respectively. For defining Henry's constants, the vapor phase has been considered as air and the mucus layer tissue site was considered as water. In this way, the vapor liquid thermodynamic equilibrium for the air-water system was examined. This equation represents the air-mucus interphase mass balance based on the equality of the species chemical potential and is defined based on two assumptions, i.e., (1) the rate of transport is instantaneous and equilibrium prevails at all times at the interface, (2) the rate of transport is controlled by the rates of diffusion through the phases. Besides, z_m is the mucus layer thickness which is assumed to be constantly equal to the average value of 10 μm covering all around the geometry domain wall boundaries (ICRP, 1994).

Eq. (1.19) was further simplified using the midpoint rule of the Riemann summation. For transient simulations, the differential term on the left-hand side (LHS) of Eq. (1.19) was defined using the implicit gradient (at the current time step) and explicit gradient (at the previous time step) predictions, i.e.,

$$\frac{\partial Y_{s,c}}{\partial x_i} \approx \frac{(Y_{s,f} - Y_{s,c})A_i^2}{r_{cf} A_i e_i} + \left(\frac{\partial Y_{s,c}^{(t-1)}}{\partial x_i} A_i - \frac{\partial Y_{s,c}^{(t-1)}}{\partial x_i} e_i \frac{A_i^2}{A_i e_i} \right) \tag{1.20}$$

where A_f and A_i are the surface area and the normal vector of the mesh element face. r_{cf} and e_i are the cell-to-face centroid distance and unit normal vector respectively.

$\xi_i = \partial Y_{s,c}^{t-1}/(\partial x_i)$ is the average face-cell centroid gradient obtained from the previous time step. Eq. (1.20) can be further expanded as

$$Y_{s,f} = \left\{ \frac{A_i^2}{A_i e_i} \frac{Y_{s,c}}{r_{cf}} - \left(\xi_i A_i - \xi_i e_i \frac{A_i^2}{A_i e_i} + \quad {}_{s} Y_{s,\infty} A_f \right) \right\} / \left\{ \frac{A_i^2}{A_i e_i} r_{cf}^{-1} - \psi_s A_f \right\} \tag{1.21}$$

Eq. (1.21) implement the face value of the species transport as a function of cell value at the current and the previous time steps as it encloses the first and second terms of the Eq. (1.20), respectively. Also, $Y_{s,\infty}$ is the species mass fraction at the tissue compartment as it can be eliminated by the rapid removal of vapor chemicals via blood circulation.

1.3.2 Boundary Conditions

1.3.2.1 Airflow Inlet Conditions with Realistic Puffing Topography

To implement the most representative and realistic puffing topographies, puffing waveforms are proposed and employed based on experimental measurements in previous papers. Three standards available both for CCs and ECs for smoking machine setup are studied. Specifically, the pattern proposed by the world health organization ((WHO), 2012) is a square waveform with the flow rate of 35 ml per 2 seconds and the 60-second interval between two consecutive puffs, i.e., (35:2:60). The second CC puffing topography proposed by ISO and the Health Canada Intense (ISO, 2015) is 55 ml per 2 seconds with a 30-second interval between two consecutive puffs (55:2:30). Additionally, the third puffing standard for EC related research is 55 ml per 3 seconds with 30-second intervals between consecutive puffs (55:3:30) (CORESTA, 2014). Other efforts seeking EC puffing topography standards are summarized as follows. Goniewicz et al. (2013) claimed an average puff volume of 70 ml for EC puffing, while (Robinson et al., 2015) tested the puffing pattern of and reported that the mean puff duration is 3.5 seconds with a mean puff volume of 133 ml. Using the same experimental setup, Behar and Talbot (2015) provided the statistical results based on a 20-subject cohort. Their investigation shows that the average interval between two puffs is 179 seconds for puffs with an average duration of 2.65 seconds and a volume of 51 ml. Furthermore, Dautzenberg and Bricard (2015) discovered that the puff duration increases slightly from 3.79 seconds to 4.11 seconds with the increase of the familiarity to EC consumption. Arguments exist on whether the observed longer puff duration is realistic or not. Longer puff duration and shorter puff interval will cause the formation of an unpleasant taste known as "dry puffs", which prevents the users to inhale EC aerosols too long to avoid the uncomfortableness. (McAuley et al., 2012; Farsalinos et al., 2015). On the other hand, CC users intend to puff longer and milder to inhale more nicotine in their lung (Feng et al., 2016).

Based on the statistical data obtained from the open literature, three different inlet conditions are considered in this study. Specifically, two puffing volumes are considered, i.e., 55 and 80 ml, which are both with a 3-second puff duration. Moreover, the puffing interval (i.e., the holding and rest duration) also varies (see Table 1.1 for details). Poiseuille flow is assumed at the mouth inlet. Furthermore, constant body temperature $T = 310.15$ K is considered in the human respiratory upper airway model. Simulation of the transient, 3-second puffing duration followed by up to 7.0 s holding time is performed by discretizing the continuous particle injection. To find the best time interval between two consecutive particle injections, different time steps have been set up for the simulation, and the cumulative particle depositions in different regions were compared. Figures 1.3 (a) and (b) depict the simulated cumulative deposition data at outlets and mouth to trachea walls respectively. The difference of the depositions for time step sizes of 0.02 s and 0.05 s are within 1.0%, hence for better computational performance, 0.05 s is selected as the final particle injection interval.

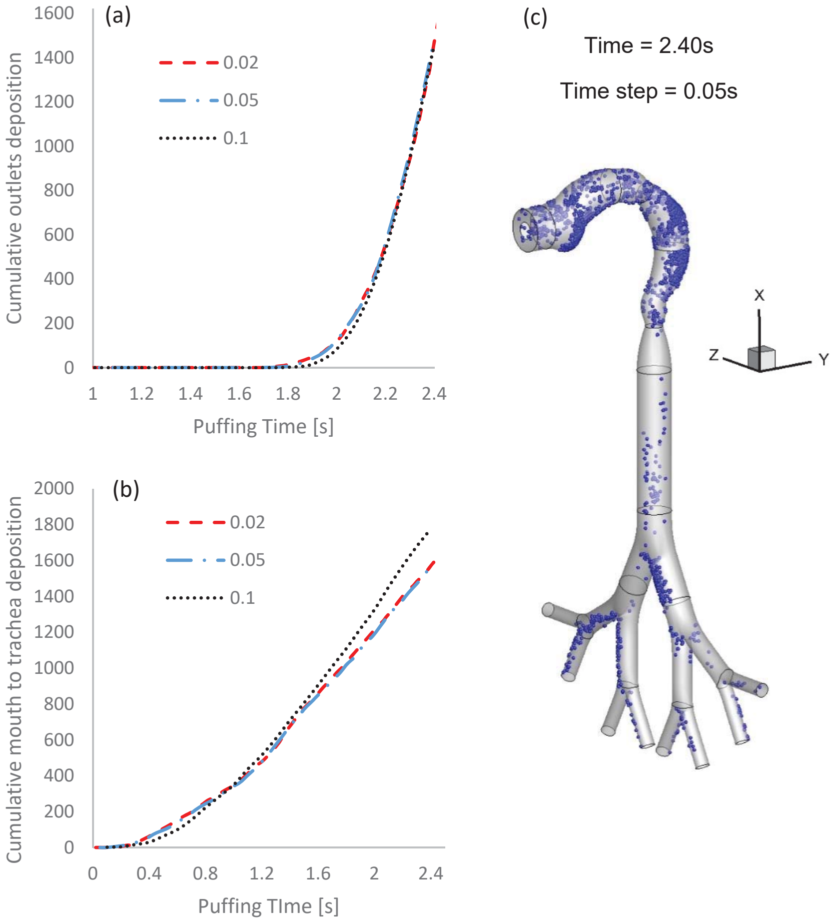

Figure 1.3: Cumulative particle deposition and escape numbers in the idealized human upper airway model for particle injection independence test: (a) particle escaping number at outlets (b) particle deposition number from mouth to trachea (c) particle deposition patterns at $t = 2.4$ s.

1.3.2.2 Particle and Vapor Inlet Conditions

Since the evaporation/condensation effects are neglected, the multi-component EC particles have the same composition as the e-liquid employed (Margham et al., 2016). Constant physical and chemical properties of EC chemical compounds are assumed. E-liquid composition provided by Margham et al. (2016) was used in this study. The EC aerosol mixture consists of 48.14% vegetable glycerin (VG), 25% of propylene glycol (PG), 25% water, 1.86% nicotine, and flavorings. The monodispersed particle diameter is assumed to be 410 nm, and the number concentration peak of 4.39e+9 particles per cm^3 is used. The choice of particle diameter and concentration are based on realistic EC aerosol measurements (Belka et al., 2017; Margham et al., 2016). The number concentration of EC particles is scaled down to enhance the computational efficiency. As long as the evaporation and condensation effect is considered to be negligible, the reduced total number of particles injected will have no impact on the accuracy of simulation results. A random-parabolic particle distribution was generated at the inlet, by an in-house MATLAB code.

For EC vapor species, the puffing topography presented by CORESTA (2014) has been used in the experiment by Margham et al. (2016). Data are also provided for the lab environment air known as a blank aerosol. In this study, the composition of the aerosol vapor is determined by the subtraction of the existing chemicals in the air. Moreover, the change in composition caused by different puff volumes (55 and 80 ml) was reported in the same work. The data are not provided for the volatile organics and nicotine. By considering the constant density for unavailable chemicals, the generated vapor composition is calculated. As long as the mass fraction of the formaldehyde and acrolein in the generated aerosol is much lower than other components, the influence of the puff volume on the aerosol composition is negligible. Additional data are provided in Table 1.1.

Nonslip boundary conditions are applied for airflow at the airway walls. The deposition of the chemicals is happening in two forms of vapor phase and the particle phase. For discrete particles, 100% trapped wall is implemented due to the presence of mucus layers. Since it is difficult to measure the flow or pressure at each airway outlets the uniform pressure outlet boundary condition with gauge pressure equal to zero is employed.

Particle diameter (nm)	410					
Temperature (K)	310					
Gas mean free path (nm)	65					
Puffing topography (ml, s, s)	55:3:30					
EC Cartridge component (wt/wt)	Acrolein	Formaldheyde	Nicotine	Glycerol (VG)	Propylene Glycol (PG)	Water
	0	0	1.86	48.14	25	25
Liquid mixture density (Kg/m^3)	1238.96					
Liquid mixture dynamic viscosity (Kg/m.s)	0.00278					
Generated vapor component per puff (wt/wt)	Acrolein	Formaldheyde	Nicotine	Glycerol (VG)	Propylene Glycol (PG)	Water
	9.04E-05	7.89E-05	4.59E-02	2.29E+00	1.02E+00	N/A
Vapor mixture density (Kg/m^3)	1.25E+00					
Vapor mixture dynamic viscosity (Kg/m.s)	1.81E-05					
Puffing topography (ml, s, s)	80:3:30					
Generated vapor component per puff (wt/wt)	Acrolein	Formaldheyde	Nicotine	Glycerol (VG)	Propylene Glycol (PG)	Water
	1.10E-04	1.07E-04	4.59E-02	2.29E+00	1.02E+00	N/A
Vapor mixture density (Kg/m^3)	1.25E+00					
Vapor mixture dynamic viscosity (Kg/m.s)	1.81E-05					

Table 1.1: Properties of the inhaled multicomponent EC aerosols (Margham et al., 2016).

1.3.3 Physiologically Based Toxicokinetic (PBTK) Model

The biological sketch of the compartments being considered in the present PBTK model is shown in Figure 1.1. There are two major types of PBTK models, i.e., perfusion-limited and diffusion-limited (Rosenbaum, 2016). Based on the lipophilic (hydrophobic) characteristics of nicotine and acrolein, perfusion-limited transport is dominant through all the compartments in the systemic region (Robinson et al., 1992). Furthermore, the division of compartments depends on the focus and goal of different studies. Since the PBTK model is designed to be combined with the CFPD model, the inputs of the nicotine and acrolein uptakes will be obtained from the lung deposition data. In the following equations, subscripts T and M represent tissue and metabolizing sites, respectively, of hepatic and renal compartments. The generalized time-dependent ordinary differential equation (ODE) for the perfusion-limited model can be given as

$$V_T \frac{d}{dt} C_T = Q_T(C_{T,in} - \frac{C_t}{K_T}) - IC_M \frac{C_T}{P_T} \tag{1.22}$$

where V_T, Q_T, and P_T are the compartment volume, flow rate, and partition coefficient, respectively. $C_{T,in}$ and C_T are the species concentration in the compartment inlet and outlet, respectively. For eliminations in the systemic regions, the intrinsic hepatic clearance (IC_H) and intrinsic renal clearance (IC_R) are considered for liver and kidney, respectively. The elimination term is equal to zero for the non-eliminating organs. For tissues other than the venous pool, arterial pool, lung, and liver the input concentrations are equal to arterial pool concentrations. Moreover, the input concentration for the venous pool is the average amalgamation of interconnected organs, which can be given by

$$C_{T,in} = \frac{1}{Q_{venous}} \sum_T Q_T(C_T/P_T) \tag{1.23}$$

where for the venous pool, Q_T is the cardiac output that represents total blood circulation flow rate and is identical for venous, arterial, and lung. For the liver, the same procedure as venous inlet can be used by combining gastrointestinal tract and arterial pool concentrations.

The accuracy of a PBTK model relies on the determination of parameters of each compartment including tissue volume, flow rate, blood-tissue partition coefficient, and alveolar flow rate at rest. Parameter values used in this study are listed in Table 1.2 (Ramsey and Andersen, 1984; Robinson et al., 1992). The optimized values for the renal and hepatic clearances are obtained from the validation that are tabulated in Table 1.7. To provide reliable predictions of toxicant translocations, we have optimized and validated the PBTK model by comparing our numerical predictions with the toxicant-plasma concentration data acquired from benchmark open literature (please see model validation).

Table 1.2: Physiochemical parameters of tissues for nicotine translocation (Robinson et al., 1992).

Compartment Name	V_T [L]	Q_T [L/min]	P_T
Arterial Pool	1.4	6.1	1
Venous Pool	4.0	6.1	1
Muscle Group	34.4	1.65	2.5
Fat Group	10	0.3	1
Vessel-Reach Group	1.55	1.35	3
Gastrointestinal Tract	2.4	1.25	2
Liver	1.5	0.3	9
Kidney	0.3	1.25	15
Lung	0.6	6.1	2

On the other hand, for formaldehyde and diacetyl the diffusion-limited PBTK model (Corley et al., 2015; Gloede et al., 2011) is adopted at the airway wall boundaries consisting of two layers: (a) epithelium plus mucus layer and (b) subepithelium (blood) layer (see Figure 1.1). The tissue-air partition coefficient (P_{ta}) provides the concentration balance between the mixture flow and the species concentration evolution profile in the epithelium plus mucus layer. The species transport in the epithelium layer is governed by

$$\frac{\partial C_{s,t}}{\partial t} = -\frac{(V_{s,max1}/V_{s,t}C_{s,t})}{K_{s,m1}+C_{s,t}} - \frac{(V_{s,max2}/V_{s,t}C_{s,t})}{K_{s,m2}+C_{s,t}} - k_{s,f}\,C_{s,t} - k_{s,b}\,C_{s,t} + D_{s,t}\frac{\partial^2 C_{s,t}}{\partial x^2} \tag{1.24}$$

where $C_{s,t}$ is the tissue concentration for species s, $V_{s,max1}$, $K_{s,m1}$, $V_{s,max2}$, and $K_{s,m2}$ are saturable metabolism constants. $k_{s,f}$ and $k_{s,b}$ are the first order reaction constants, and $D_{s,t}$ is the species diffusion coefficient in the tissue layer. Subsequently, the tissue-blood partition coefficient provides the concentration balance between the transferred species to the subepithelium layer, and the governing equation is given as

$$\frac{\partial C_{s,b}}{\partial t} = -k_{s,f}\,C_{s,b} - k_{s,b}\,C_{s,b} - (Q_{s,b}/V_{s,b})C_{s,b} + D_{s,b}\frac{\partial^2 C_{s,b}}{\partial x^2} \tag{1.25}$$

In Eq. (1.25), $(Q_{s,b}/V_{s,b})$ is the blood perfusion term and $D_{s,b}$ represents the species diffusion coefficient in the subepithelium (blood) layer. To solve Eqs. (1.24 and 1.25) implicitly, the central difference scheme is used for discretization, and tridiagonal matrices are generated at each time step (see Appendix A). Constants and coefficients of the CFPD-PBPK model were obtained from Corley et al. (2015) for formaldehyde, and from Gloede et al. (2011) for diacetyl (see Table 1.3).

1.3.4 Interconnection Model between CFPD and PBTK

Mucus, epithelial, and subepithelial layers are the barriers between lung and blood circulation. The interconnection model between CFPD and PBTK models presented in this study is addressed in the following. One-way exchange from the lung to blood is assumed due to the negligible amount of toxicants reentering the lung from the blood circulation. Bush et al. (1998), Corley et al. (2015), and Corley et al. (2012) used the physiological configuration concept of the mucosa bed including the mucus, epithelial,

Description	Parameters	Formaldehyde	Diacetyl
Diffusivity in Blood	D_b (cm^2/s)	1.62E-05	4.33E-06
Partition coefficients	P_{ta}	101.5	50
	P_{bt}	1	1
Metabolism (high affinity)	K_{m1} (g/l)	201	8.60
	V_{max1} (g/l/s)	1.96E+04	5.59E-02
Metabolism (low affinity)	K_{m2} (g/l)	N/A	5.59E+02
	V_{max2} (g/l/s)	N/A	0.158
Intrinsic binding with tissue	K_f (1/s)	1.80E-02	5.00E-03
Non-specific binding	K_b (1/s)	1.07E-07	N/A
Mass transfer coefficients for non-mucus coated squamous epithelium	K_s (cm/s)	4.10E-01	N/A
Site-specific adjustment factor of V_{max1}	Nose	1.00E+00	1
	Mouth to primary Bronchi	2.50E-01	1.41
	Bronchioles	5.00E-01	1.051
Site-specific adjustment factor of $Vmax2$	Nose	N/A	1
	Mouth to primary Bronchi	N/A	3.81
	Bronchioles	N/A	0.65

Table 1.3: Physiochemical parameters used for formaldehyde and diacetyl translocation in tissues (Corley et al., 2015; Gloede et al., 2011).

and subepithelial layers. Considering no reaction in the layers makes it possible to use Henry's law of vapor-liquid equilibria for estimating the uptake magnitude due to vapor phase deposition (Smith et al., 1996). The air and mucus phase diffusivity and Henry's law constant for the chemicals presented in this study are listed in Table 1.4.

Table 1.4: Properties of nicotine and acrolein in vapor forms.

Species (s)	$D_{a,s}$[cm^2/s]	$D_{w,s}$[cm^2/s]	$\mathcal{H}_{c,s}$	ψ_s[cm^{-1}]
Acrolein	0.105	1.12e-05	4.99e-03	2.14e+03
Formaldehyde	0.180	2.00e-05	1.38e-05	8.07e+05
Diacetyl	0.100	$D_{t,s}$ = 4.33e-06	1.33e-05	3.26e+06
Nicotine	0.065	$D_{t,s}$ = 8.60e-06	5.60e-08	2.36e+08
VG	0.088	9.30e-06	7.07e-07	1.506e+07
PG	0.106	1.23e-05	5.31e-07	2.18e+07

To estimate the available vapor species concentration entering the systemic region based on the absorption rate predicted by the CFPD model and boundary conditions, the regional area weighted average mass fraction $Y_{s,R}$ can be given as:

$$Y_{s,R} = \frac{\sum_{cells} Y_s A_c}{\sum_{cells} A_c} \tag{1.26}$$

In Eq. (1.26), subscript R represents "Region". For calculation of the vapor species uptake concentration ($C_{V,u,s}$), the following equation is utilized

$$C_{V,u,s} = \sum_{R} f_{R,V,s} \frac{0.05 \rho Y_{S,R} V_P}{3 A_R z_m} \tag{1.27}$$

where 0.05 denotes to the selected CFPD simulation time step, A_R is the region surface area, and $f_{R,V,s}$ is the regional bioavailability factor provided in Table 1.5. The lymph vein compartment connecting with the lung is assumed as a layer with a constant thickness (z_m). The surface area of the regions are provided in Table 1.5.

Table 1.5: The surface area of the regional sections and bioavailability factors of the idealized human upper airway.

Region Number	Name	Area [cm^2]	Bioavailability Factors		
			EC Particles	Nicotine in Vapor	Acrolein in Vapor
Region 1	Oral Cavity	0.3545	9	0.39	0.14
	Oropharynx/Larynx	0.4151	9	0.39	0.14
Region 2	Trachea	0.4240	12	0.79	0.29
Region 3	G1	0.2984	17	1.99	0.49
	G2	0.5209	17	1.99	0.49
	G3	0.4666	17	1.99	0.49

For the diffusion of the chemical compounds due to particle depositions, the transient regional number of deposited particles are recorded by considering the wall boundaries as 100% trapped wall. The species uptake concentration $C_{p,u,s}$ due to particle deposition is calculated by

$$C_{p,u,s} = \sum_{R} f_{R,p,s} SC \frac{nD_R \rho_{p,s} \pi d_p^3}{6 A_R z_m} \tag{1.28}$$

where $SC = 1.0\text{e}{+7}$ is the scaling factor selected to enhance the computational efficiency without losing precision. Specifically, particle numbers injected per time step are multiplied by SC, so that the regional particle number deposition (nD_R) reflects the actual number of particles carried by the generated aerosol. The bioavailability factors for the particle phase are provided in Table 1.5. It should be noted that these fractions will justify the influence of the lymph vein distribution concentration, diffusion, and reaction of the species.

Therefore, adding Eqs. (1.27-1.28) yields the total uptake concentration of the chemical compound ($C_{uptake} = C_{p,u,s} + C_{V,u,s}$). An example of concentration time course is shown in Figures 1.12 (a) and (b). To quantify the toxicant's average uptake, the area under the curve (AUC) and the time step size need to be known. The average uptake concentration can be calculated by

$$AUC = \frac{\int_{t_1}^{t_2} C_{T,inlet}}{t_2 - t_1} \tag{1.29}$$

In this study, the only input source of toxicants is from the EC aerosol inhalation via the pulmonary route. Dermatological absorption can be neglected. Additionally, by assuming that the equilibrium will always hold between inhaled air and the pulmonary blood circulation, the material mass balance equation for toxicants can be given as

$$C_{arterial} = \frac{\dot{Q}_{lung} C_{uptake} + \dot{Q}_{venous} C_{venous}}{\dot{Q}_{venous} + \dot{Q}_{lung}} \tag{1.30}$$

where is the deposition concentration predicted by the CFPD model.

1.4 Geometry and Mesh Independence Test

1.4.1 Idealized Human Upper Airway Model

In this study, an idealized upper human respiratory airway from the oral cavity to G3 with eight outlets is selected. The structure dimensions are based on the sizes presented by Cheng et al. (1999) with a revised 8-mm mouth opening (see Figure 1.1). Despite the simplification of the geometry, it contains the most important anatomical features of the human upper airway that is essential in the study of the EC aerosol deposition and mass exchange at airway walls. Based on the physiological characteristics of the respiratory system, the current geometry has been divided into three sections based on the thickness of the mucus layer in different regions and also the existence of the lymph veins after the sub-epithelium layer. Region 1 includes the oral cavity and the pharynx with the thickest mucus layer and lowest lymph vein concentration. Region 2 is the trachea with lower thickness and the higher existence of the lymph vein connected to the tissue. Region 3 consists of the tracheobronchial tree from G1 to G3 with the lowest mucus layer thickness and the highest lymph vein concentration (see Table 1.5).

1.4.2 Hexahedral Mesh Generation and Mesh Independence Test

Computational meshes were generated, using the commercial software ICEM CFD v. 18.0 (ANSYS Inc., Canonsburg, PA). The structured, multi-block mesh developed with the feature of hexahedral elements and refinement at the wall boundaries. The final mesh has the total elements number of 2,374,679, with 2,319,768 nodes. The mesh independence test has been performed by Feng et al. (2016) with the inlet volumetric flow rate of 27.5 ml/s. The mesh topology was determined by refining the mesh until grid independence of the flow field solution was achieved.

1.4.3 Numerical Setup

The numerical solution of the governing equations with appropriate boundary conditions was achieved by using a user-enhanced, commercial finite-volume based program, i.e., ANSYS Fluent and CFX 18.0 (ANSYS Inc., Canonsburg, PA). All variables, including velocity components, pressure, turbulence variables, and particle trajectories and deposition data are calculated and located at the centroids of the discretized mesh cells. Numerical simulations were performed on a local 64-bit Dell Precision T7910 workstation with 256 GB RAM and sixteen 3.1GHZ CPUs and the supercomputers in High Performance Computing Center at Oklahoma State University (e.g., Cowboy cluster machine with 252 standards compute nodes with dual Intel Xeon E5-2620 “Sandy Bridge” hex core 2.0 GHz CPUs, with 32 GB of 1333 MHz RAM). A second-order upwind scheme was used for the momentum equation calculation. For the calculation of the species transport, the first order upwind was employed, and for the pressure and velocity coupling in the finite volume solver, the semi-implicit method for pressure-linked equations (SIMPLE algorithm) has been selected. The system of ODEs of the PBTK model was solved using the 4th order Runge-Kutta method. The PBTK model has been written in C language in the form of user-defined functions (UDFs) and was attached to the CFPD model in ANSYS

Fluent 18.0. As a result at each puff, the translocation of the current toxicants has been tracked in systemic regions. The time delay of the translocation was neglected.

1.5 Model Validations

1.5.1 CFPD Model Validations

For particle dynamics model validations, regional deposition efficiencies (RDEs) were compared with benchmark experimental data in the idealized upper airway geometry (see Figures 1.4 (a) - (c)) with 1-cm mouth inlet (Cheng et al., 1999). The inlet conditions with uniform velocity condition and the volumetric flow rates of 15, 30, and 60 L/min are applied for the polystyrene latex fluorescent particles. As shown in Figure 1.4 (a), the extrathoracic RDE is a function of impaction parameter d_p^2Q [$\mu\text{m}^2\text{Lmin}^{-1}$]. The empirical curve and the numerical results show good agreement in mouth-to-throat RDE. The total DE of the present model sufficiently reaches an agreement with the published literature. Additionally, comparisons with experimental deposition data at various flow rates are plotted in Figure 1.4 (b). The numerical data also show the same trend for the particles in the same range. For the microparticles, DF increases with the increased particle diameter due to the enhanced inertial impaction. In contrast, higher RDEs are observed for nanoparticles compared to submicron particles due to the enhanced Brownian motion. Furthermore, Figure 1.4 (c) shows additional deposition data comparisons with good agreements. In summary, the CFPD model is well validated.

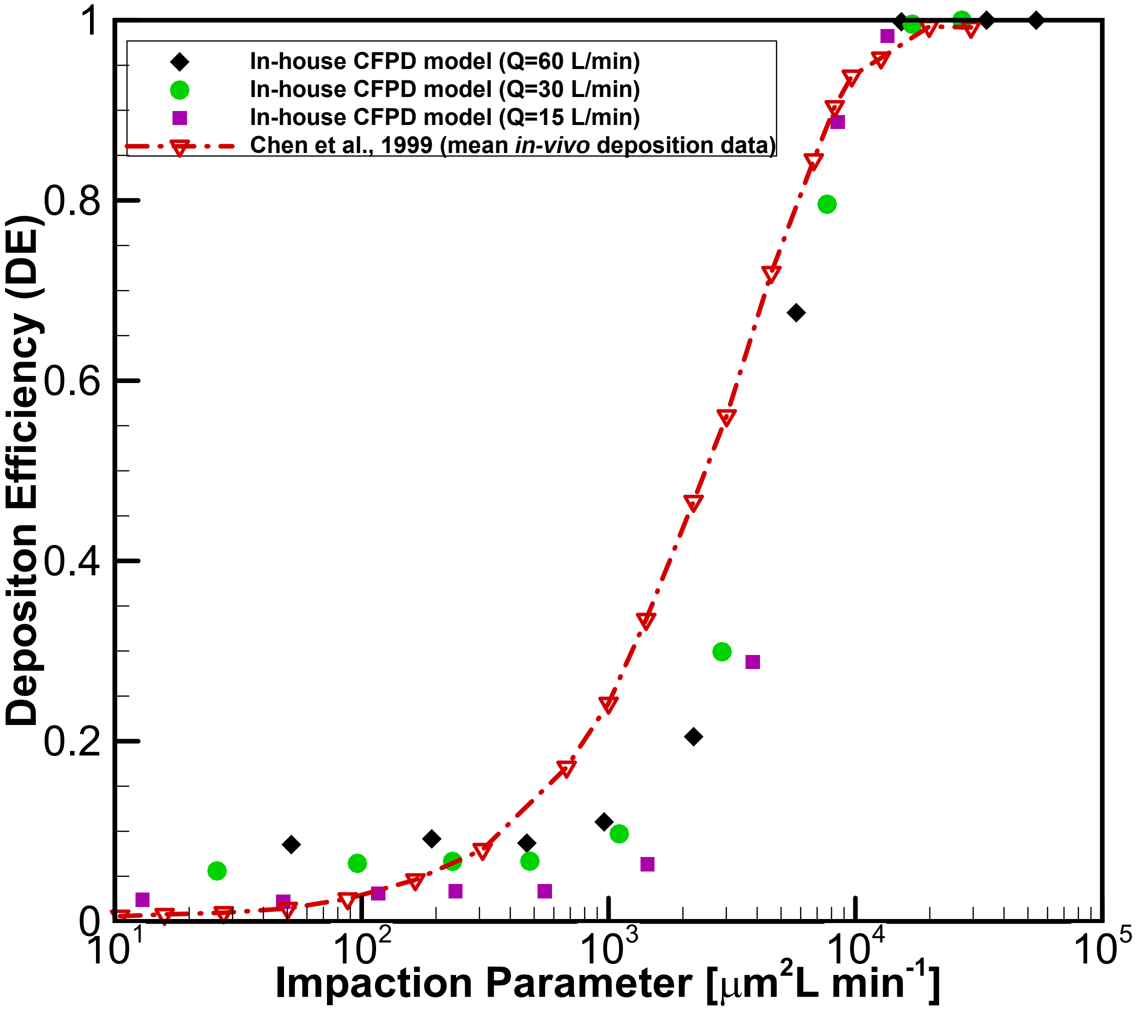

(a)

Figure 1.4: CFPD model validations: (a) deposition efficiency comparisons in the oral cavity with different mean impaction parameters (b) deposition efficiency comparisons in the oral cavity for different particle sizes (c) deposition efficiency comparisons in the oral cavity with different Stokes numbers.

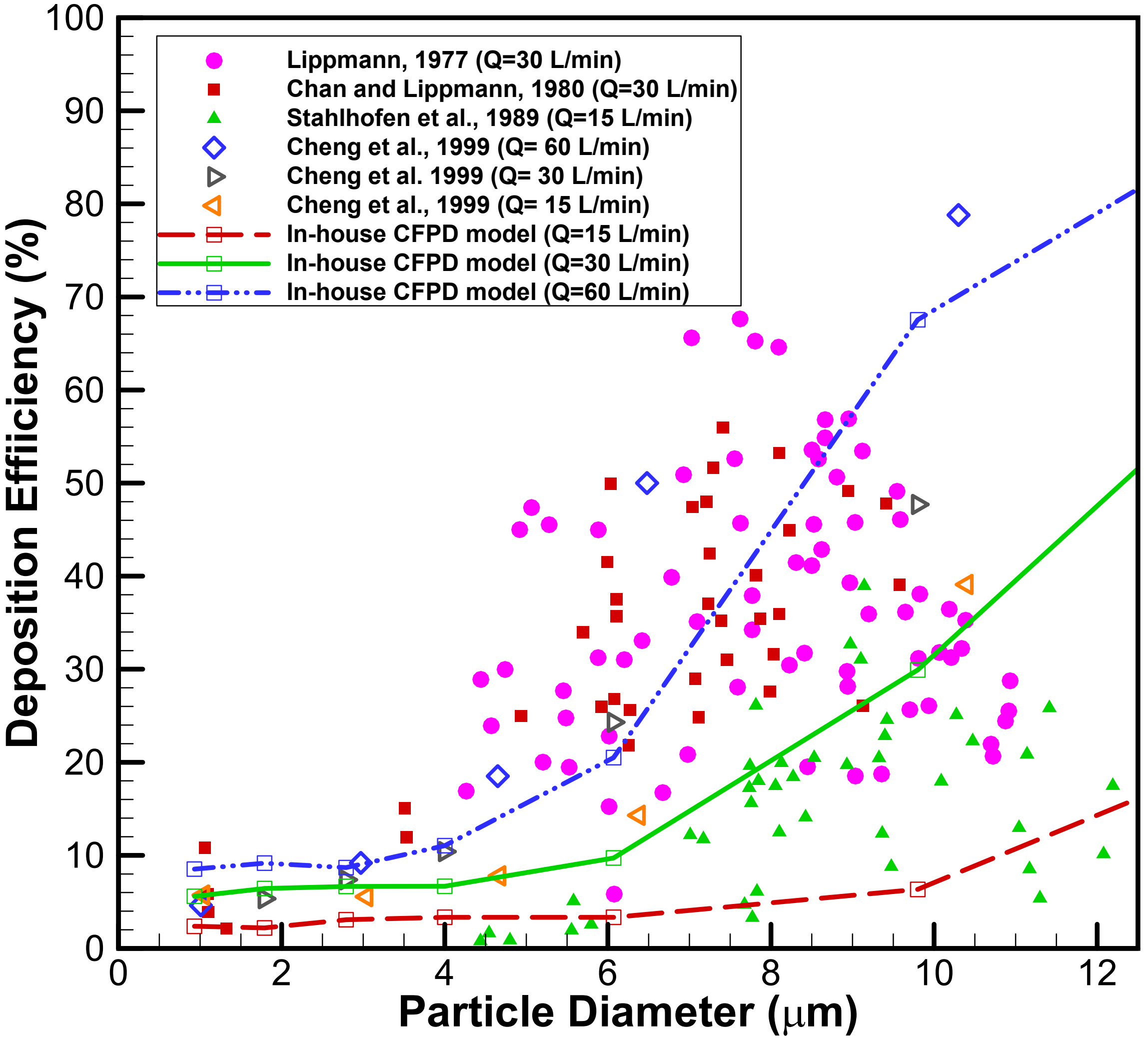
Deposition Efficiency (%)
Particle Diameter (μm)
0
10
20
30
40
50
60
70
80
90
100
0
2
4
6
8
10
12
Lippmann, 1977 (Q=30 L/min)
Chan and Lippmann, 1980 (Q=30 L/min)
Stahlhofen et al., 1989 (Q=15 L/min)
Cheng et al., 1999 (Q= 60 L/min)
Cheng et al. 1999 (Q= 30 L/min)
Cheng et al., 1999 (Q= 15 L/min)
In-house CFPD model (Q=15 L/min)
In-house CFPD model (Q=30 L/min)
In-house CFPD model (Q=60 L/min)

(b)

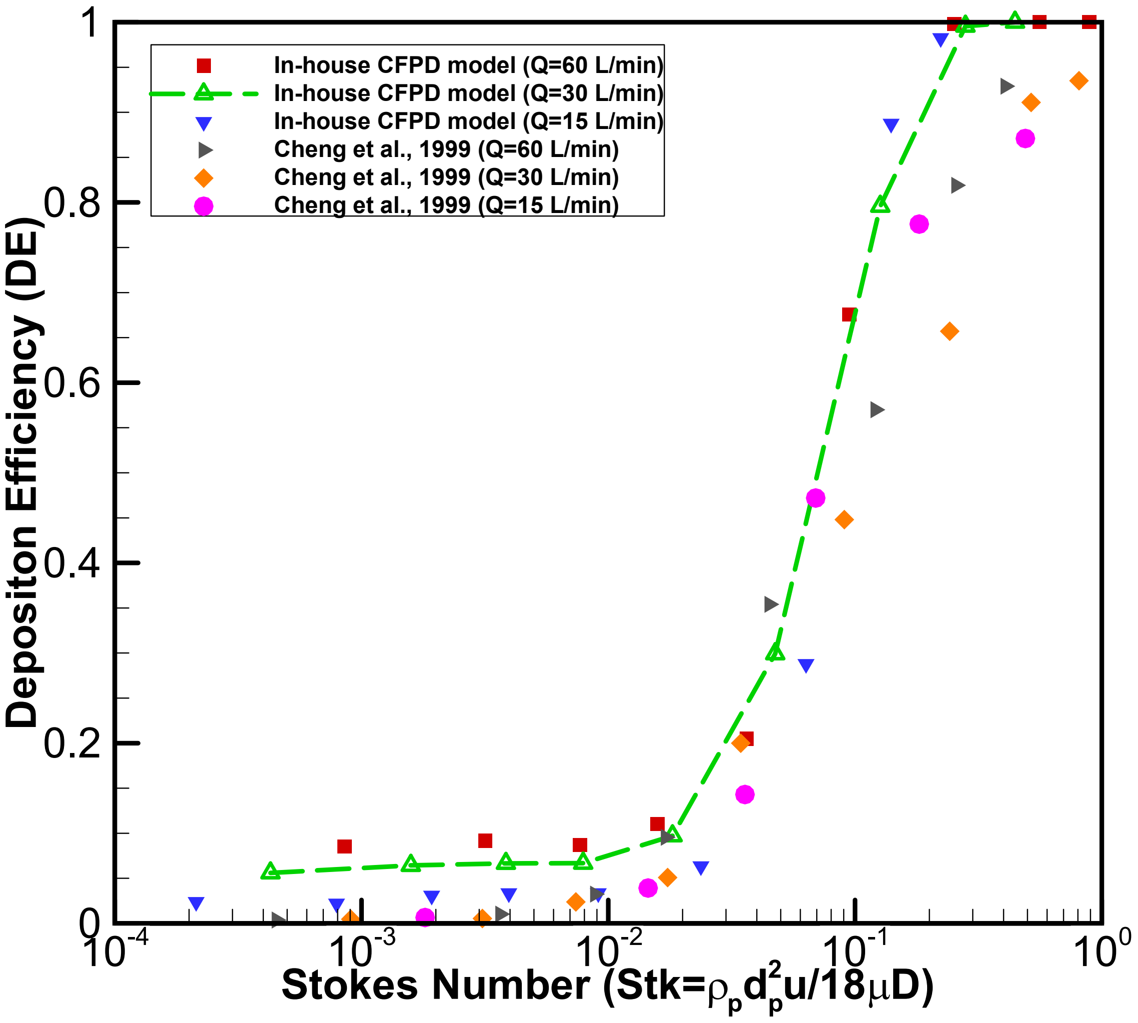

(c)

1.5.2 PBTK Model Optimizations and Validations

1.5.2.1 Nicotine

For nicotine PBTK model validation, plasma concentration vs. total volume is compared and presented in Figure 1.3. The details of this experiment are provided in Table 1.6. Benchmark experimental data of nicotine plasma concentrations due to CC smoking scenarios (Benowitz et al., 1982; Kyerematen et al., 1990) were employed first and used for two independent model validations for nicotine PBTK. Two different mass flow rates of nicotine infusion were employed, i.e., 40 μg/min for 30 minutes and

95 μg/min for 2 minutes. The PBTK model was also compared with nicotine plasma concentration data of an EC study by Dawkins et al. (2016). Specifically, E-liquid with 6-24 ng/ml nicotine has been used on 11 volunteers for 60 minutes, who were abstained from smoking for 6 hours before the clinical test. Additionally, numerical results generated by another PBTK model (Robinson et al., 1992) is also included in Figure 1.3. Employing the parameters provided by Dawkins et al. (2016), our nicotine PBTK predictions show good matches with experiments.

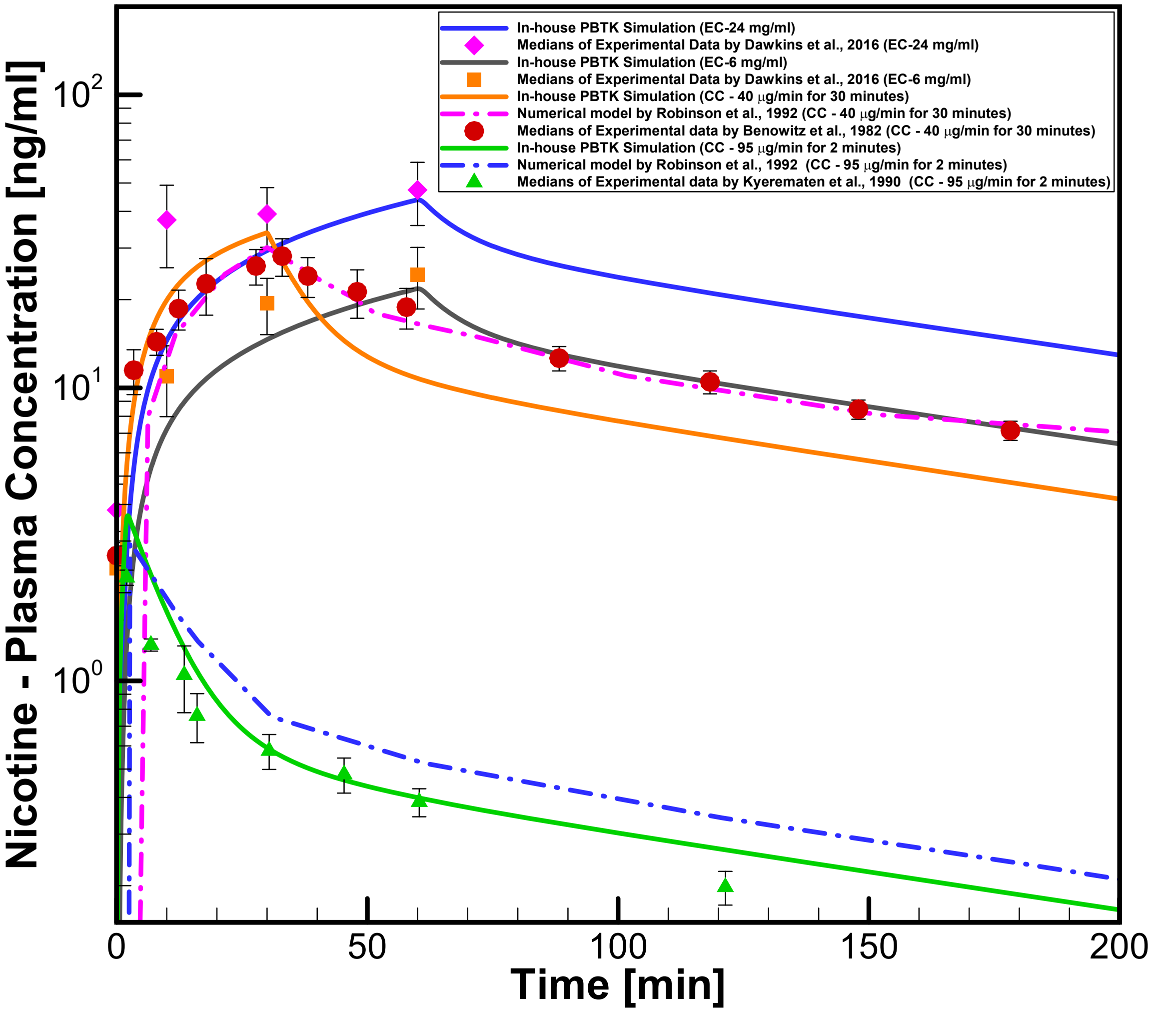

Figure 1.3: Nicotine PBTK model optimization and validations.

Volunteers	EC device	Nicotine solution	Study design	Uptake results	Puffing topography	Reference
11 (11 male)	eVic^{TM} supreme, with Nautilus Aspire tank, 3.9 V (8.5 W)	6-24 mg/mL	60 min ad libitum	nicotine concentrations of 8.59, 16.99, and 22.03 ng/ml at 10, 30 and 60 min	Mean number of puff: 70.73; Puff duration: 5.20 s	Dawkins et al. (2016)
				nicotine concentrations of 33.77, 35.48, and 43.57 ng/ml at 10, 30 and 60 min	Mean number of puff: 48.26; Puff duration: 3.84 s	
16 (15 male)	cartomizer, 3.3 V; 1.5 (7.26 W)	8 mg/ml	2 bouts with duration of 10 min; 10 puff; puff restriction on users	Bout 1: peak nicotine concentration 17.8 ng/ml	Bout 1: Mean puff volume: 208.4 ml; Puff duration: 6.1 s; Bout 2: Mean puff volume: 176 ml; Puff duration: 5.5 s	Ramoa et al. (2015)
				Bout 2: peak nicotine concentration 16.9 ng/ml		
		18 mg/ml		Bout 1: peak nicotine concentration 25.9 ng/ml	Bout 1: Mean puff volume: 124.2 ml; Puff duration: 5.35 s; Bout 2: Mean puff volume: 114.7 ml; Puff duration: 4.97 s	
				Bout 2: peak nicotine concentration 23.6 ng/ml		
		36 mg/ml		Bout 1: peak nicotine concentration 36 ng/ml	Bout 1: Mean puff volume: 84.3 ml; Puff duration: 4.17 s	
				Bout 2: peak nicotine concentration 24.7 ng/ml	Bout 2: Mean puff volume: 78.5 ml; Puff duration: 3.98 s	

Table 1.6: Benchmark experimental data on nicotine translocations for the nicotine PBTK model optimization and validation.

1.5.2.2 Acrolein

Exposure to acrolein in the human body has not been investigated due to the invasive nature of the test methodology (ATSDR, 2007). Animal studies (F-344 rat, mice) are employed in this study. There is a need to employ a scale-up factor from animal to human based on the body weight (BW) differences. The time scaling-up equation proposed and validated by Bailey et al. (1989) and Kreyling et al. (1998) are used to convert the animal data to human organ volume size.

$$\frac{Time_{human}}{Time_{animal}} = \left(\frac{BW_{human}}{BW_{animal}}\right)^{0.275} \tag{1.31}$$

For the comparison, data of creatinine with a density of 0.0024 mg/ml and 3-HPMA for 1 and 0.5 ppm inhalation of the pure acrolein by Conklin et al. (2017) in mice is introduced. To scale up between species, the weight comparison of 73 kg (human)/0.23 kg (mice) are quoted in the clearance phase. The optimized values of the hepatic and renal clearances are investigated for the case of the 1.0-ppm exposure, and the same values are employed for the comparison of the case with the 0.5-ppm exposure. As it is shown in Figure 1.4, the increase in intake amount shift the concentration profile to higher maximum uptake, and the clearance process of the higher concentration of the intake concentration is higher than the lower intake exposure.

The experience as the relative definition and influencing factor of acrolein uptake have been investigated in the study by Struve et al. (2008). Two groups of pre-exposed and naïve F344 rats are exposed to acrolein through inhalation and the influence of the parameters of acrolein concentration (0.6, 1.8 and 3.6 ppm) and constant velocity unidirectional inspiratory flow rate (100 and 300 ml/min) for 80 min exposure on the acrolein and glutathione uptake efficiency on upper respiratory are investigated. The experienced rats were previously exposed to acrolein for 6 hrs/day, 5 days/week in 14 days duration.

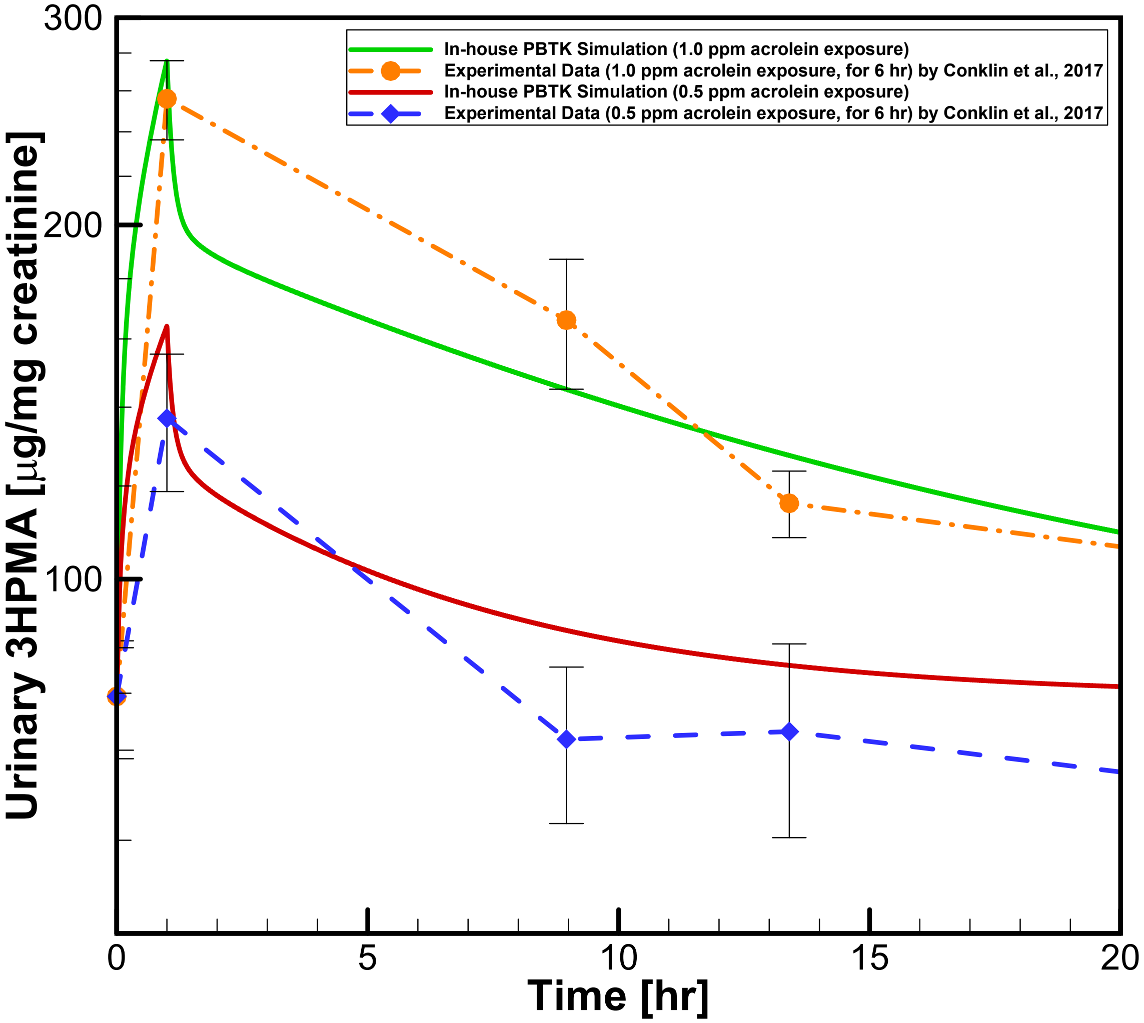

Figure 1.4: Acrolein PBTK model optimization and validations by the comparisons of 3-HPMA concentration in rats.

Studies on acrolein inhalation exposure using animals show no significant change in the hepatic and renal processes. It was proposed that liver weight will relatively increase in rats in the long-term exposure of 60-180 days (Kutzman et al., 1984). A similar pattern was investigated for an increase in kidney size in rats and hamsters exposed to 4-5 ppm for 60-90 days (Kutzman et al., 1985). All in all, the assumption for constant renal and hepatic clearance function seems reasonable. The optimized values of the renal and hepatic clearances of acrolein and nicotine are provided in Table 1.7.

Table 1.7: Optimized parameter values of hepatic and renal clearances.

Chemical (Objective Case)	Renal intrinsic clearance (IC_R) [L/min]	Hepatic intrinsic clearance (IC_H) [L/min]
Nicotine (Robinson et al., 1992)	0.170	1.090
Acrolein (Conklin et al., 2017)	0.226	0.946

1.5.2.3 Diacetyl and Formaldehyde

Understanding the dose response of the respiratory tissue to the exposed irritant aerosols is crucial to recognize the inspired vapor toxicity. Flavor chemicals such as diacetyl of EC that can be toxic presents high percentage of refilling and concentrated sample fluids (Allen et al., 2015). Inhaling butter flavoring vapors is expected to cause morphologic changes, e.g., air trapping, bronchial wall inflammation, and constrictive bronchiolitis (Akpinar-Elci et al., 2004). Inflammation of bronchioles and constrictive bronchiolitis are expected at high-concentration exposure incidents of diacetyl (Akpinar-Elci et al., 2004). Farsalinos et al. (2014) investigated 159 different EC samples (concentrated and refill samples), in which 78 has contained diacetyl with a median concentration of 20 μg/ml. Klager et al. (2017) investigated 24 EC flavors from four different brands in the U.S. and results showed the existence of diacetyl in 62% of products. Allen et al. (2015) examined 51 unique flavors and claimed a maximum mass of 238.0 μg/e-cigarette for Peach Schnapps flavor, which is significantly higher than the National Institute for Occupational Safety and Health (NIOSH) limit for occupational exposure to diacetyl, i.e., 65 μg/day, estimated by Farsalinos et al. (2014). Formaldehyde was found in the emitted vapor as 19.8 μg/10 puffs at 4.0 V, which is 32% lower than the CC daily exposure (Farsalinos et al., 2017). Higher voltage of EC device resulted in significantly higher formaldehyde concentration due to the formation of dry puff.

Corley et al. (2015) investigated the in tissue translocation of the formaldehyde generated from the CC smoke using a steady-state hybrid CFD-PBPK approach and compared the site-specific dosimetry in airways between rat and human. Gloede et al. (2011) performed a PBPK model for inspired vapor diacetyl dosimetry based on the Morris et al. (1993) model. In the absence of CFD simulation, the respiratory tract was modeled as a series of compartments, i.e., nose, trachea, main bronchi, large and small bronchi, bronchioles, and alveoli, and the subsequent tissue layers. Molecular diffusivity, reaction, and metabolism were employed for the simulation and the parameters were obtained from *in vitro* studies. The results showed 24% of the inspired chemical penetrates through the small bronchi and to the bronchioles during a lightly exercising human nasal breathing. However, the delivery dose to lower airways for both mouth and nasal breathing is less than 10% of the delivery to the upper airway and the trachea.

To validate the formaldehyde absorption by the airway tissues, the nasal extraction data of rat exposed to the unidirectional flow rate of 135 ml/min is compared at two formaldehyde concentrations of 6 and 15 ppm (Kimbell et al., 2001). The subject-specific human respiratory system with the nasal cavity (see Section 2.4.1 and Figure 2.1) is used and the absorption data are scaled by comparing the ratio of nasal cavity surface areas of F344 rat and human (Sharma and McNeill, 2009). For both inlet conditions, the difference between the in-house model prediction and the experimental data is less than 4.7% (see Figure 1.5). Using the same approach, the diacetyl absorption is validated by comparing F344 rat and human whole respiratory fractional uptake (Gloede et al., 2011) with the estimated uptake in the upper human airway model provided in Section 2.4.1. A realistic mouth breathing condition with a duration of 4.02 s is considered (see Section 2.4.3.1). Numerical results are compared with the experimental data at two diacetyl doses of 5 and 25 ppm, and the predicted values demonstrate the model's capability to simulate the non-linear relationship between the uptake efficiency and the inhaled diacetyl concentration (see Figure 1.5).

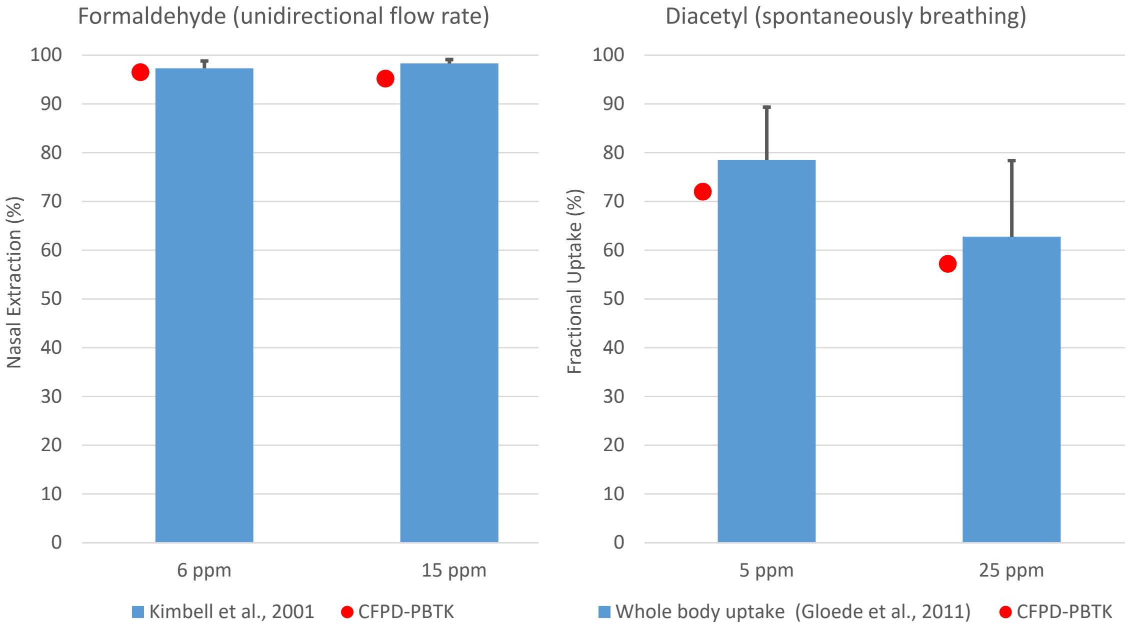

Figure 1.5: CFPD-PBTK model validation: (a) formaldehyde administration with unidirectional flow rate estimates by Kimbell and Subramaniam (2001) (b) diacetyl spontaneously breathing and nasal extraction data by Gloede et al. (2011).

1.6 Results and Discussion

1.6.1 EC Particle Transport and Deposition

The translocation of the EC toxicants including acrolein and nicotine are numerically investigated in the idealized human upper airway model. Three realistic puffing inlet conditions are applied (see Section 1.3.2.2 for details). As shown in Figures 1.6 to 1.10, the local EC particle deposition patterns are significantly influenced by the airflow regime determined by the average puff flow rate. Moreover, after the puffing duration, the holding time will result in increased deposition due to Brownian motion and the gravity sedimentation effects. The transient local airflow patterns with secondary flows and recirculation regions are shown in Figures 1.6 and 1.7.

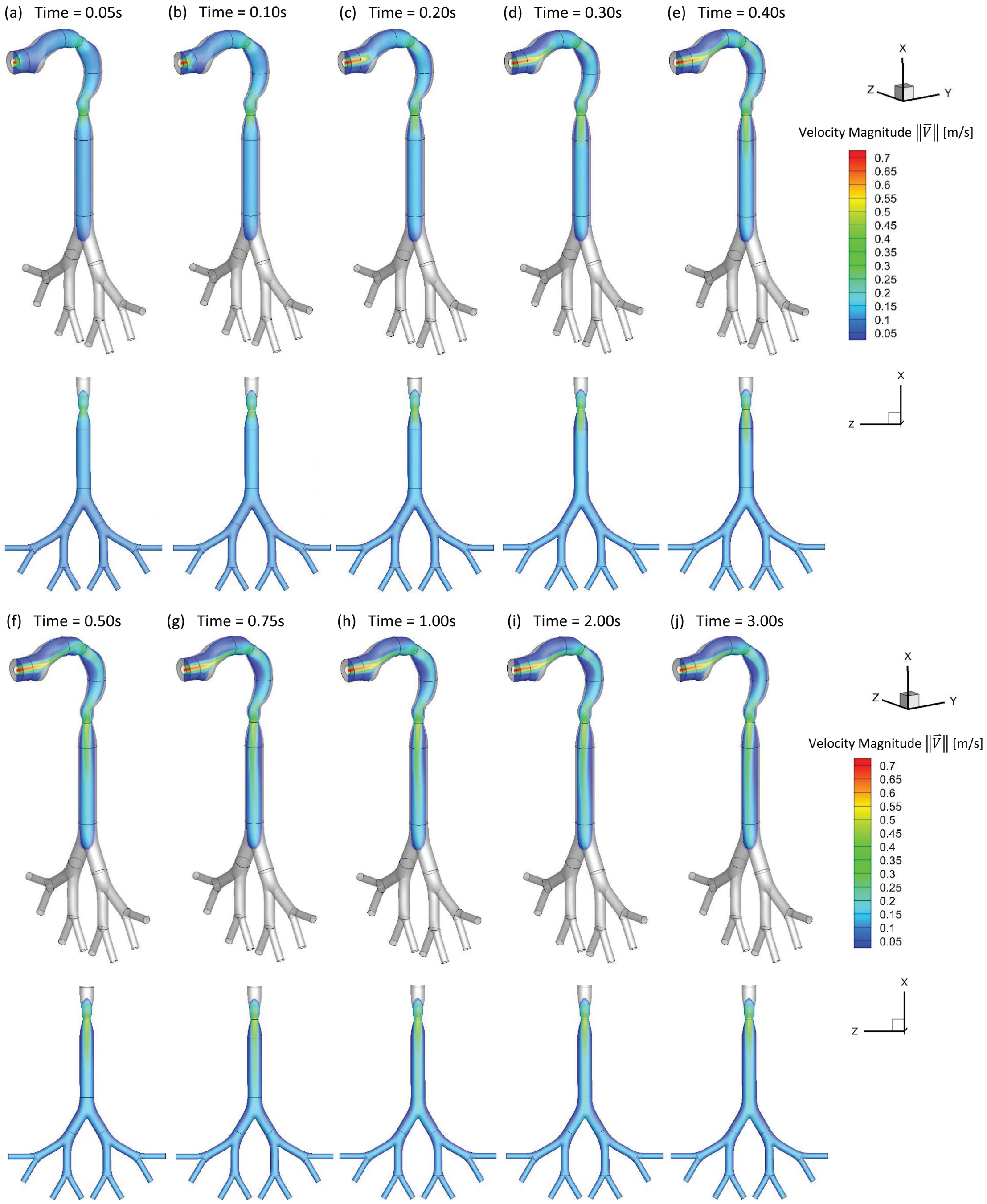

Figure 1.6: Transient airflow patterns in the idealized human upper airway model (Q_{in} = 55 ml per 3.0 s): (a) $t = 0.05$ s; (b) $t = 0.10$ s; (c) $t = 0.20$ s; (d) $t = 0.30$ s; (e) $t = 0.40$ s; (f) $t = 0.50$ s; (g) $t = 0.75$ s; (h) $t = 1.00$ s; (i) $t = 2.00$ s; (j) $t = 3.00$ s.

Specifically, Figures 1.6 (a)-(j) show the airflow pattern transition at the sagittal plane and frontal plane by visualizing velocity magnitudes at different time steps.

It can be observed from Figures 1.6 (a)-(d) that a jet flow is evolved from the EC mouthpiece at the beginning of the puff. At $t = 0.3$ s, the high-velocity jet impacts the lower palate forms the recirculation region in the oral cavity, and deviate the path towards pharynx and trachea. At $t = 0.40$ s the inlet jet is completely formed in the oral cavity and the pharynx (see Figure 1.6 (e)) and the second recirculation region at the front side of the pharynx is formed due to the centrifugal effects of the mainstream flow. At $t = 0.50$ s, the high-velocity jet reaches the trachea region. The third recirculation is formed at the back of the trachea due to the pressure variations induced by the glottis. Due to the small particle size, most particles will follow the high-velocity jet and have small chance to enter the recirculation regions. However, there is a small portion of the particles, which can enter the recirculation region. Those particles will have longer residence time and higher change to deposit induced by Brownian motion effects. It should be noted that the backflow will increase the residence time of particles entering the recirculating regions while reducing the local deposition avoid direct impaction of the particles carried by the mainstream flow (see Figure 1.7).

Additionally, Figures 1.7 (a)-(e) show the transient local deposition patterns of EC particles. The deposition of the particles at $t =$1.0 s, 2.0 s, and 3.0 s followed by 1.0 s and 2.0 s holdings are provided. Low deposition efficiencies (DEs) at the airway walls covered by recirculation regions. Enhanced local deposition efficiencies (LDEs) are found at the lower palate, pharynx, and bifurcating points because of inertial impaction and gravitational sedimentation. Figures 1.7 (d) and (e) demonstrate that particles continue to deposit at lung airways during the holding phase. Increased holding time will result in higher depositions. Therefore, it is necessary to simulate the holding duration to obtain accurate particle deposition patterns for EC vaping and passive exposure.

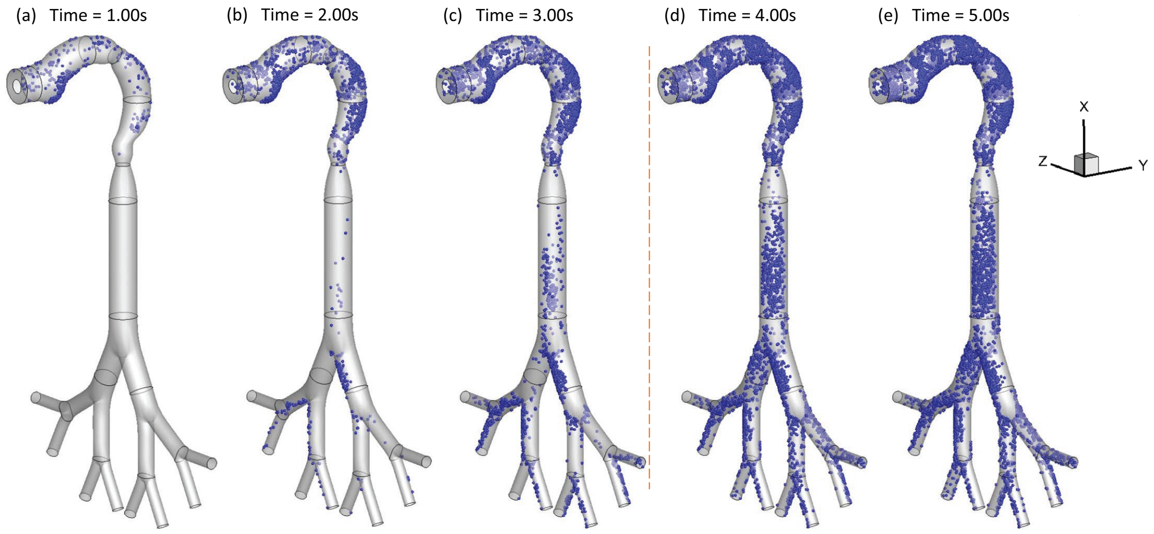

Figure 1.7: Local deposition patterns of EC particles ($Q_{in} = 55$ ml per 3.0 s with 2-sec holding): (a) $t = 1.0$ s; (b) $t = 2.0$ s; (c) $t = 3.0$ s; (d) $t = 4.0$ s; (e) $t = 5.0$ s.

1.6.2 EC Vapor Species Transport and Absorption

As an example, Figures 1.8 and 1.9 show the mass fraction contour evolution of acrolein and nicotine vapors at the sagittal plane for puff volume of 55 ml. After being inhaled, acrolein and nicotine vapors follow the airflow well to transport from the oral cavity to the tracheobronchial region gradually. Due to the high diffusion rates of both vapors into the airway tissues, most of the acrolein (99%) and nicotine (99%) in vapor forms are absorbed before reaching the glottis (see Table 1.4 for the binary diffusivities). Therefore, the translocation of both vapor species into the blood circulation happens at human upper airways.

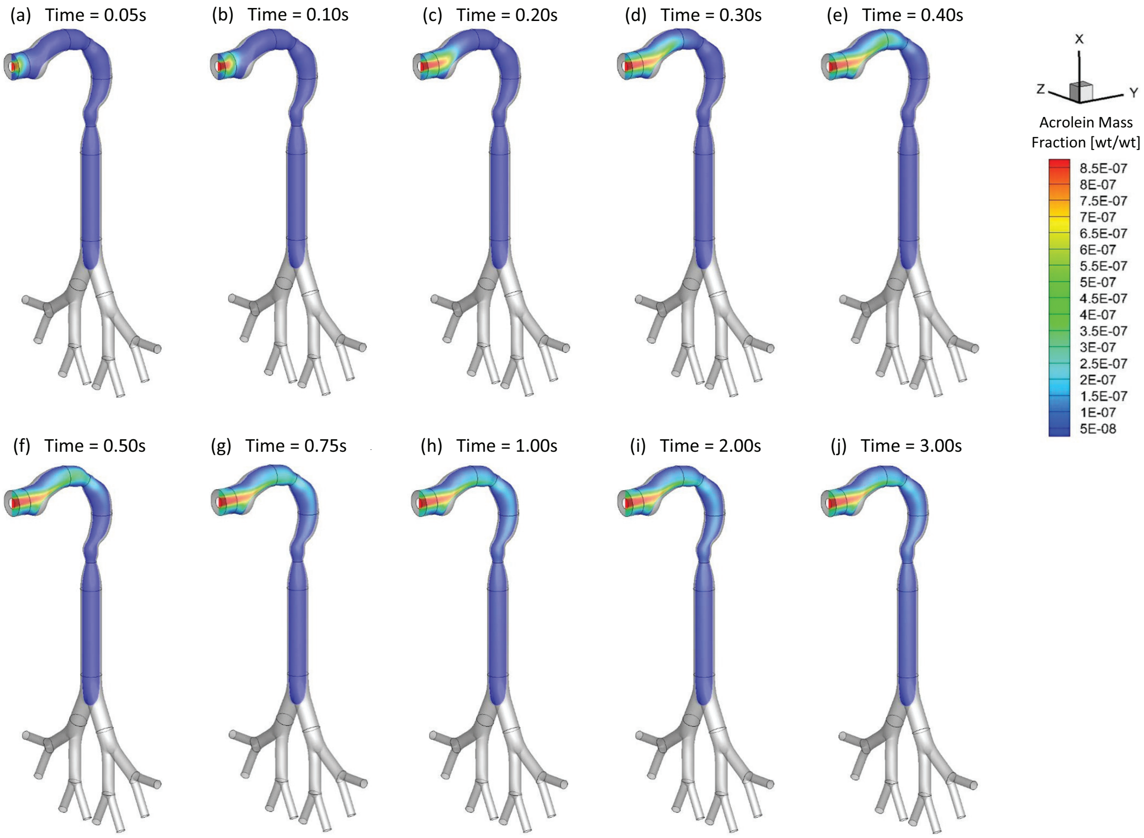

Figure 1.8: Mass fraction distribution of acrolein vapor at different ($Q_{in} = 55$ ml per 3.0 s): (a) $t = 0.05$ s; (b) $t = 0.10$ s; (c) $t = 0.20$ s; (d) $t = 0.30$ s; (e) $t = 0.40$ s; (f) $t = 0.50$ s; (g) $t = 0.75$ s; (h) $t = 1.00$ s; (i) $t = 2.00$ s; (j) $t = 3.00$ s.

1.6.3 Puff Topography Influence on EC Aerosol Transport Dynamics

The impact of puff topography on EC aerosol transport and deposition were investigated and shown in Figures 1.10 and 1.11. As shown in Figure 1.10 for two puff volumes, most particles deposit on the mouth to glottis region for both inlet puffing volumes. Higher puffing flow rate induces longer residence time of particles in G1 to G3, leading to higher deposition due to inertial impaction. "Hot spots" of particle deposition include lower palate, pharynx, glottis, and bifurcating points of each generation.

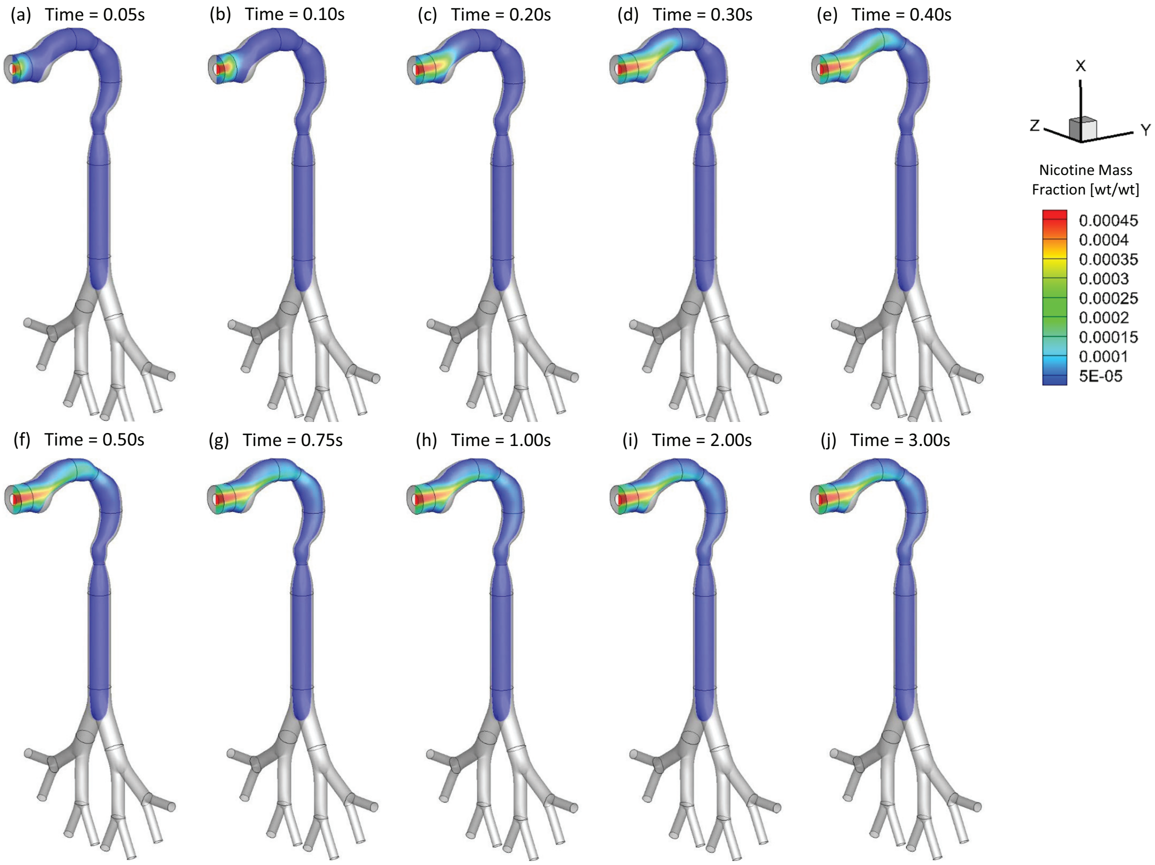

Figure 1.9: Mass fraction distribution of nicotine vapor at different ($Q_{in} = 55$ ml per 3.0 s): (a) $t = 0.05$ s; (b) $t = 0.10$ s; (c) $t = 0.20$ s; (d) $t = 0.30$ s; (e) $t = 0.40$ s; (f) $t = 0.50$ s; (g) $t = 0.75$ s; (h) $t = 1.00$ s; (i) $t = 2.00$ s; (j) $t = 3.00$ s.

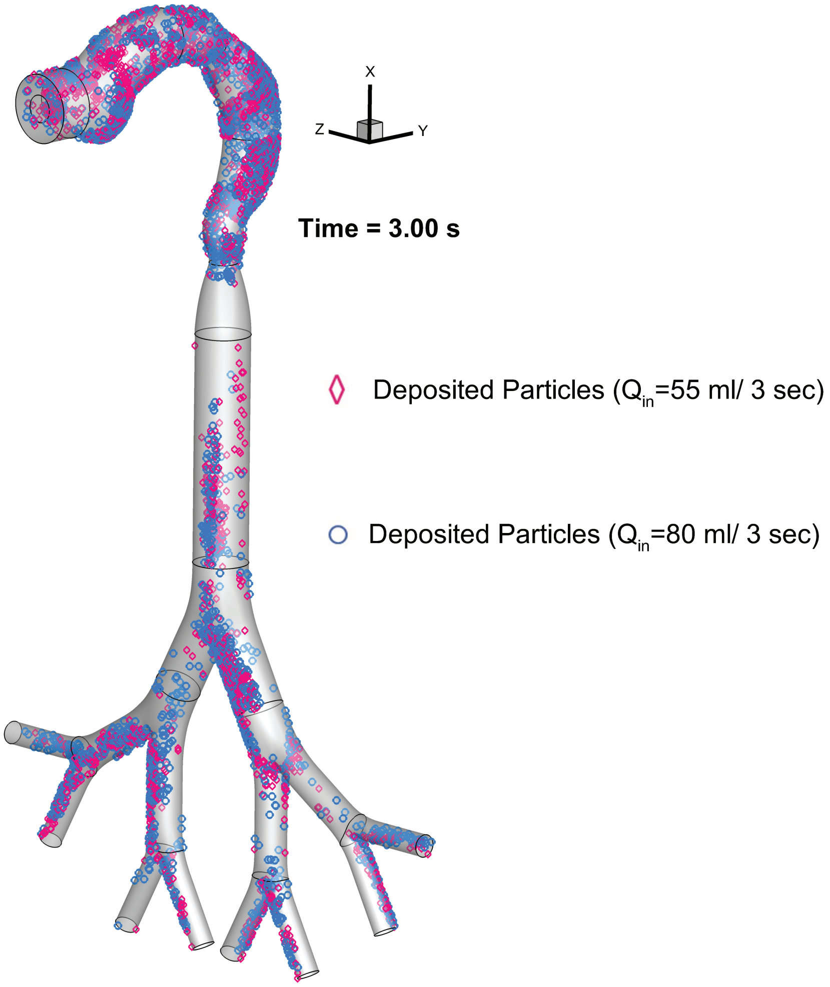

Figure 1.10: Comparison of the EC particle deposition patterns at $t = 3.0$ s between two puffing volumes.

Additionally, comparisons of regional deposition fractions (RDFs) for all cases with different inlet conditions are shown in Figure 1.11. The histogram indicates that high puff flow rate leads to enhanced RDFs due to the stronger inertial impaction effect and less EC particles will be able to transport into deeper airways. Increased holding time will also increase RDFs because of the increased particle residence time. The subsequent holdings to active puffs increase the residence time of the EC particles, which were still suspending in the lung. Hence, the regional deposition will continuously occur with the progress of holding time.

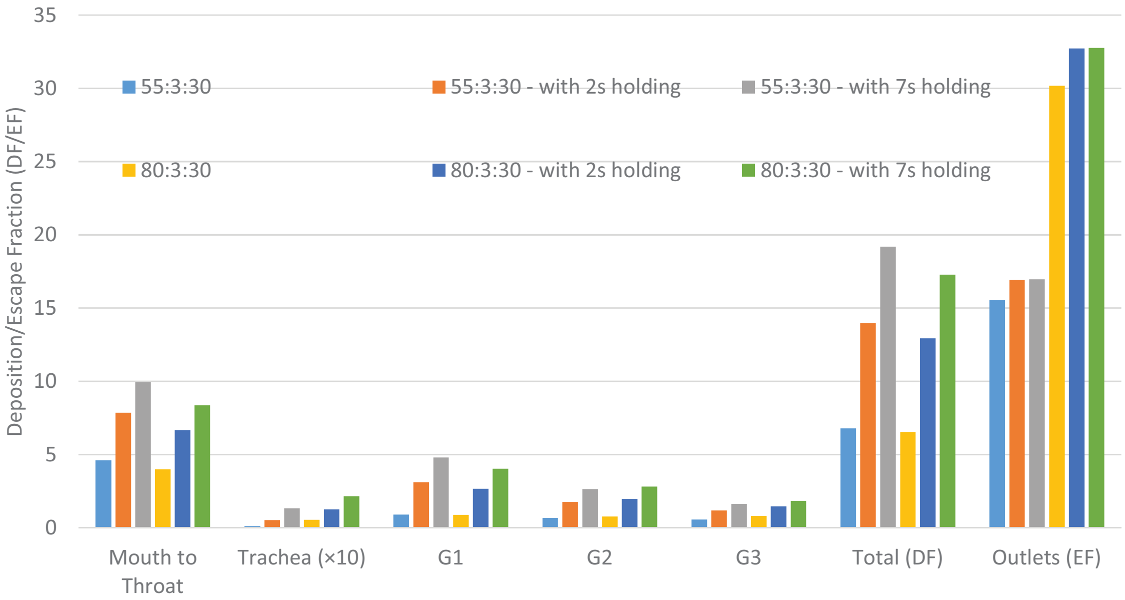

Figure 1.11: Comparisons of EC particle deposition fractions in the idealized human upper airway model.

1.6.4 Translocations of EC Toxicants in Systemic Regions

As the lung input to the PBTK model, total toxicant deposition was calculated by adding depositions of both particulate and vapor phases. Optimized values of bioavailability factors were determined for the simplified CFPD-PBTK connection model, by matching plasma concentration profiles from benchmark experiments (Ramôa et al., 2015; Shahab et al., 2017; Goniewicz et al., 2017). Since CFPD results indicate that the existence of the acrolein and nicotine in the region after trachea is negligible (see Section 1.6.2), it can be concluded that the total uptake of both nicotine and acrolein are mostly dependent on their absorption in human upper airways. Distribution and translocation of the toxicants are discussed separately in the following sections.

1.6.5 Nicotine Translocation

The concentration input profile in both vapor phase and particulate phase for nicotine are provided for all simulation cases with different puff topographies, i.e., two puffing volumes (55 and 80 ml per 3.0 s) and three holding times (0.0 s, 2.0 s, and 7.0 s). Figures 1.12 (a) and (b) show the concentration profiles for 10 seconds including 3 second puffing time followed by 2 and 7 seconds holding time for nicotine at two puffing volumes of 55 and 80 ml. The AUC over 30-second puffing duration for each case is also provided which shows the average uptake value of each puff. Particle depositions are scaled up based on the realistic particle number concentrations. Subsequently, nicotine input concentration due to particle deposition and vapor absorption are considered, and the correlation is generated using nonlinear regression by the least square method.

The AUCs show that for the case of 55 ml puffing volume the average uptake concentration per puff can be significantly higher for 2.0 s holding time (67.13 % increase) and for 7 seconds holding time (112.49% increase). Also for the case with 80 ml puffing volume, the increases are 57.52% and 95.57% respectively for 2 and 7-sec holding times. Moreover, increasing puff volume will increase vapor absorption. However, it has little influence on particle deposition. As a result, the total deposition of the nicotine and respectively its uptake has increased by 21.61% for the case without holding time. This difference between different puffing volumes is simulated as 14.62% and 11.93% for 2 and 7-sec holding times respectively in the course of 30.0 s puff duration. In this study, the influence of the exhalation has not been considered, and the deposition concentration after the holding time is set to zero. This assumption is reasonable since most deposition of nicotine in both vapor and particle forms occur before t=10.0 s (see Figures 1.12 (a) and (b)).

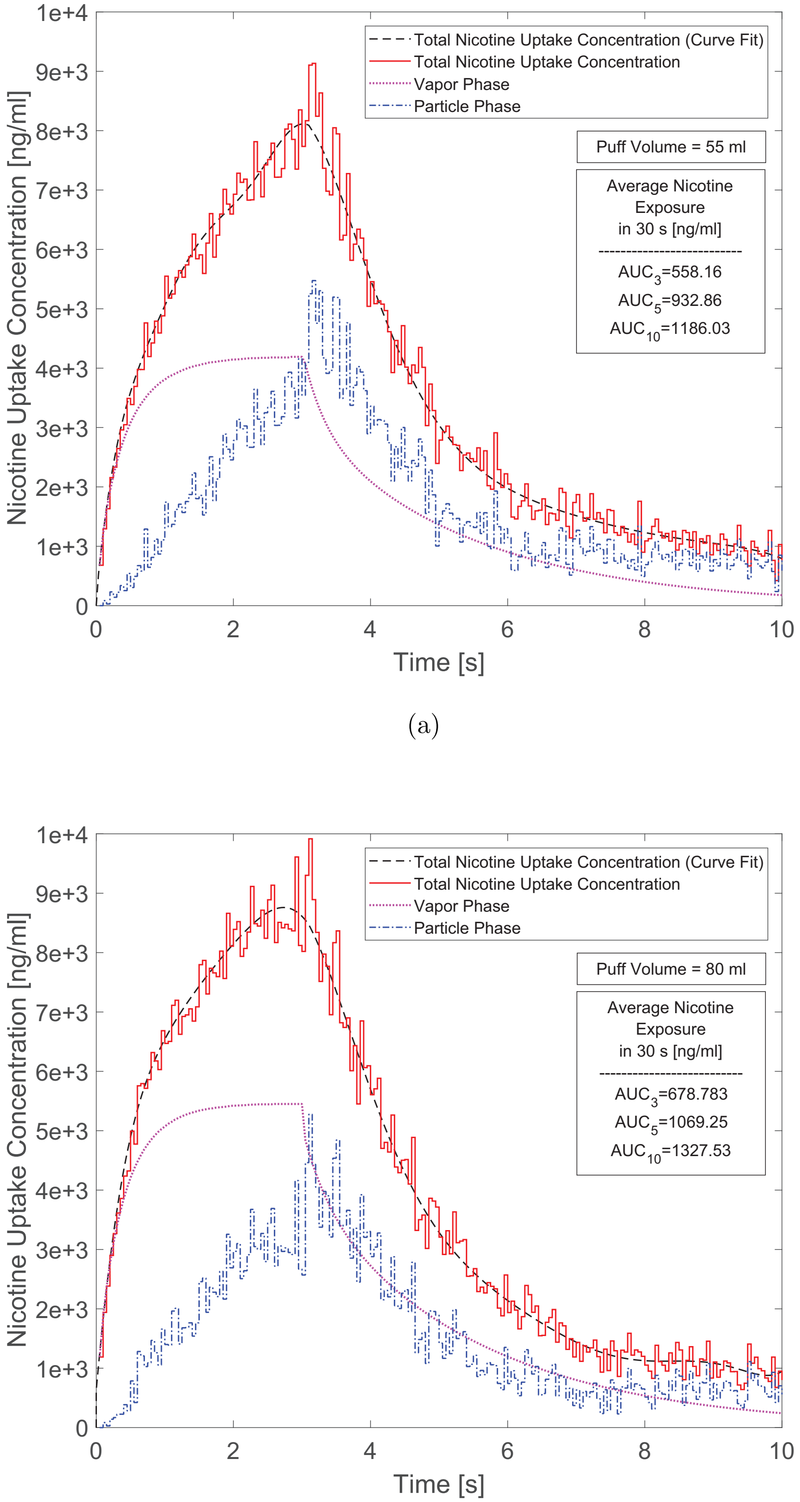

(a)

(b)

Figure 1.12: Time courses of nicotine uptake concentration after 3-sec puffing duration followed by 7 seconds holding time: (a) 55 ml puffing volume, (b) 80 ml puffing volume for 10 seconds of the total puffing duration (30 seconds).

The predicted nicotine plasma concentrations under different puff volumes are provided in Figures 1.13 (a) and (b). 10 puffs with 30.0 s puffing duration are considered. The first puff results in a sudden increase in nicotine concentration. The subsequent 9 puffs increase the concentration gradually at a slower rate. The peak plasma concentrations after 10 puffs for the case of 55 and 80 ml puffing volumes are 15.58 ng/ml and 18.88 ng/ml without considering holding time. It can also be observed that due to the higher absorption and deposition, the increase in holding time generates higher plasma concentrations. At the same time, the realistic holding time will result in a change of the exhalation time. Overall, the increase in holding times will contribute to the exponential increase of the nicotine bioavailability. Changing puffing volume only has a slight effect on nicotine plasma concentration compared to changing holding time.

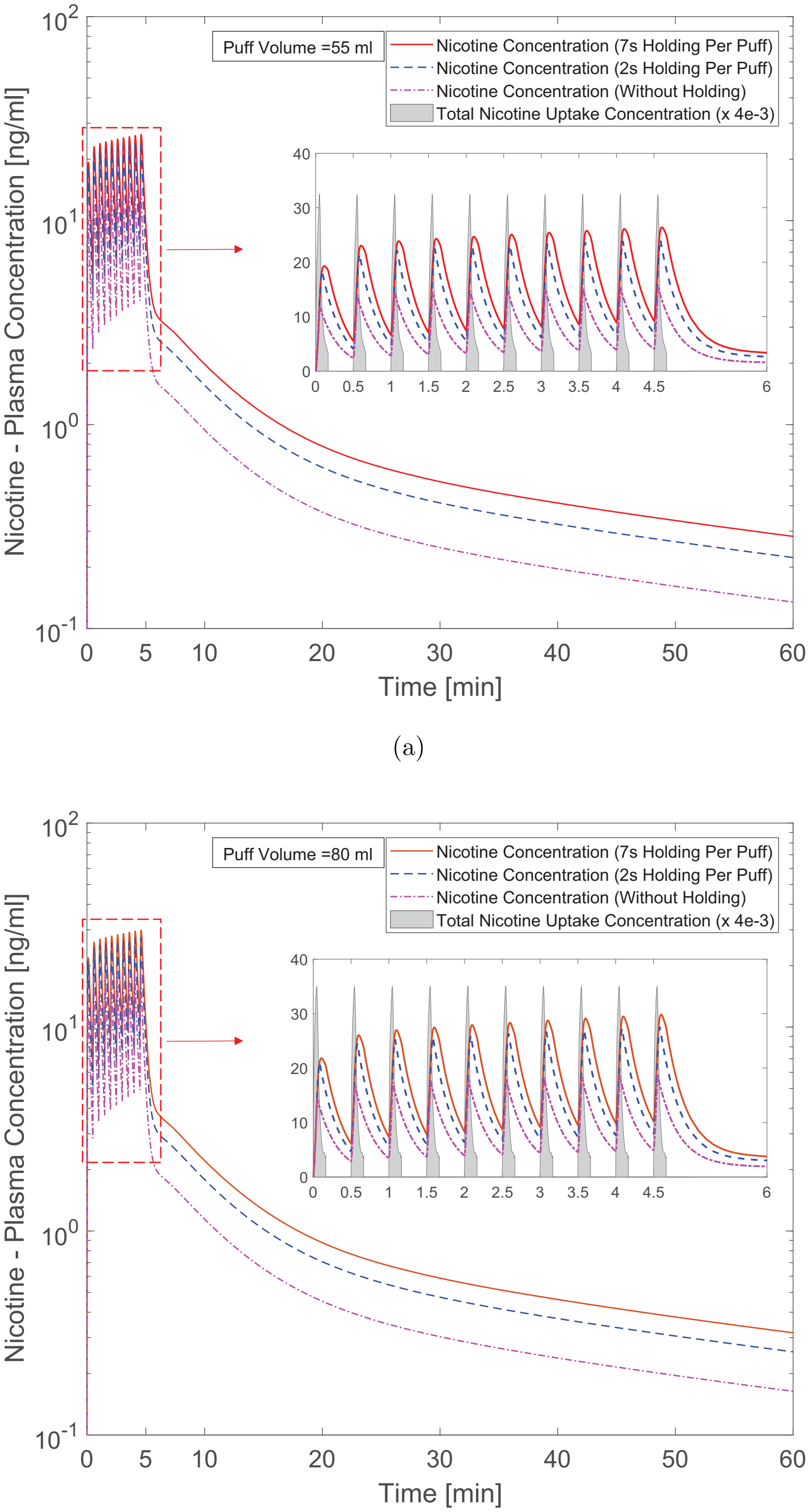

(a)

(b)

Figure 1.13: Time courses of nicotine plasma concentration: (a) 55 ml puffing volume, (b) 80 ml puffing volume (the nicotine uptake concentration has been scaled down for better visualization).

1.6.6 Acrolein Translocation

Acrolein exists only in the vapor phase based on the initial condition applied in this study. As a result, the uptake concentration will be induced by the vapor phase absorption, which is shown in Figure 1.14 for the two cases with 55 and 80 ml puff volumes. It is obvious that the increase in puff volume results in the increase of the peak value of the uptake concentration from 0.508 to 0.792 ng/ml. The average AUC for 30 seconds for different cases with different holding times are also provided. For the cases with of 55 ml and 80 ml puffing volumes, increases of AUC as representative of per puff exposure after considering two holding times of 2.0 s and 7.0 s are 45.51%, 83.27%, 44.45%, and 134.53 respectively.

Figures 1.15 (a) and (b) present the acrolein plasma concentration within 10 puffs. The puff by puff increase of the acrolein concentration can be observed. The first puff has resulted in a major increase in the concentration. After 10 puffs, peak concentrations of acrolein with different holding times from 0.0 s to 7.0 s are 0.001221, 0.001648, 0.001803 ng/ml for 55 ml puffing volume case and 0.001947, 0.002614, 0.002864 ng/ml for 80 ml puffing volume case. For better visualization effect, the acrolein uptakes were scaled down by 4e-3 for better visualization. The reason for the difference is that the difference of the considered lymph vein volume compared to the plasma volume.

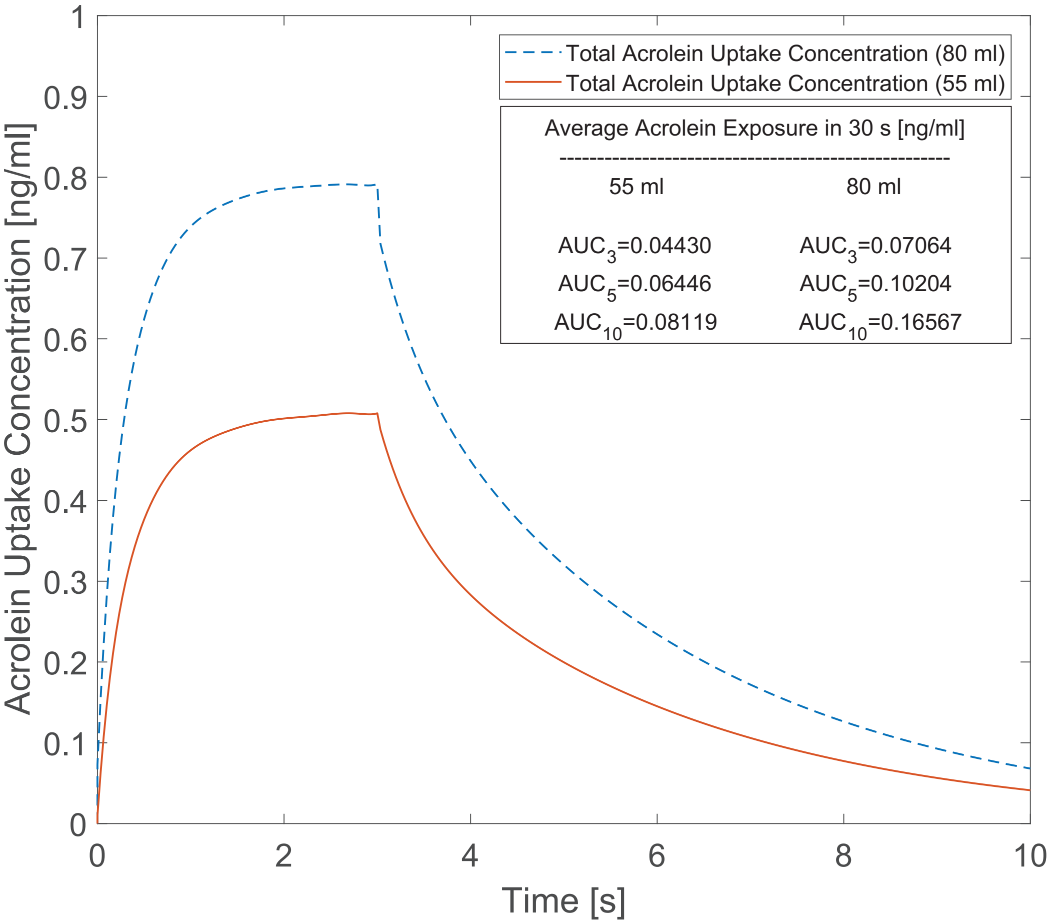

Figure 1.14: Time course of acrolein uptake concentration after 3-sec puffing duration followed by 7 seconds holding time at two puffing volumes of 55 and 80 ml for 10 seconds of the total puffing duration (30 seconds).

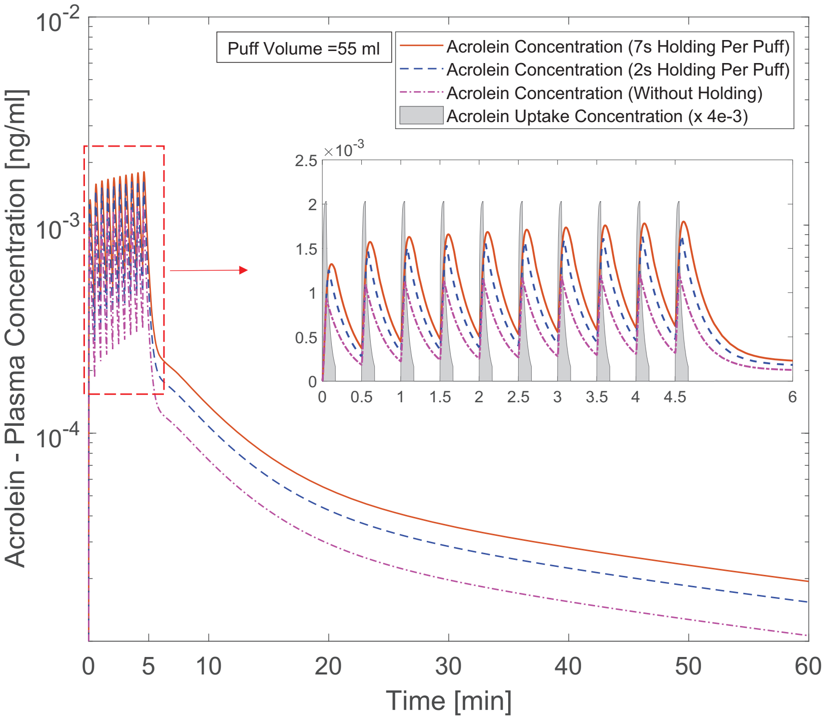

(a)

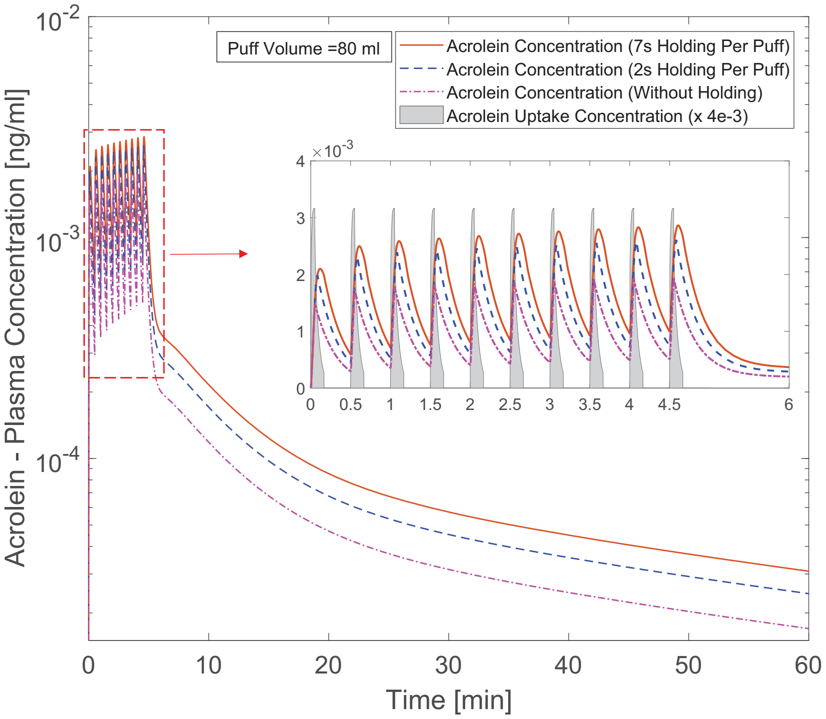

(b)

Figure 1.15: Time courses of acrolein plasma concentration: (a) 55 ml puffing volume, (b) 80 ml puffing volume (the acrolein uptake concentration has been scaled down for better visualization).

The formation of 3-HPMA produced by the binding between acrolein and glutathione has been identified in the urinary sample of rats (Alarcon, 1976). As a result, 3-HPMA is considered as the primary metabolite and possible biomarker of acrolein bioavailability. 3-HPMA concentration at the kidney is shown in Figure 1.16. It should be noted that in this study the regional bioavailability factors are considered as representative of reactions taking place to form the metabolites of the species. In this way, complete conversion of acrolein to 3-HPMA has been initiated to the PBTK model for the acrolein. It is worth mentioning that acrolein itself has lipophilic characteristic and the perfusion-limited models can be reliable prediction based on our simulation. However, it is also essential for future studies to investigate the fate of transport in the tissue for its main metabolites. In Figure 12, the puff-by-puff increase of the concentration in the kidney can be observed. Damped concentration profile in the kidney can be attributed to the configuration of the compartments. The peak concentration in excretion for 55 ml puffing volume are 110.74, 160.40, and 201.58 ng/mg creatinine for the three cases with 0.0, 2.0, and 7.0-sec holdings after the 3.0 s puff duration. Also, for cases with 80 ml puffing volume, the peak values are 176.78, 245.35, and 321.15 ng/mg creatinine respectively.

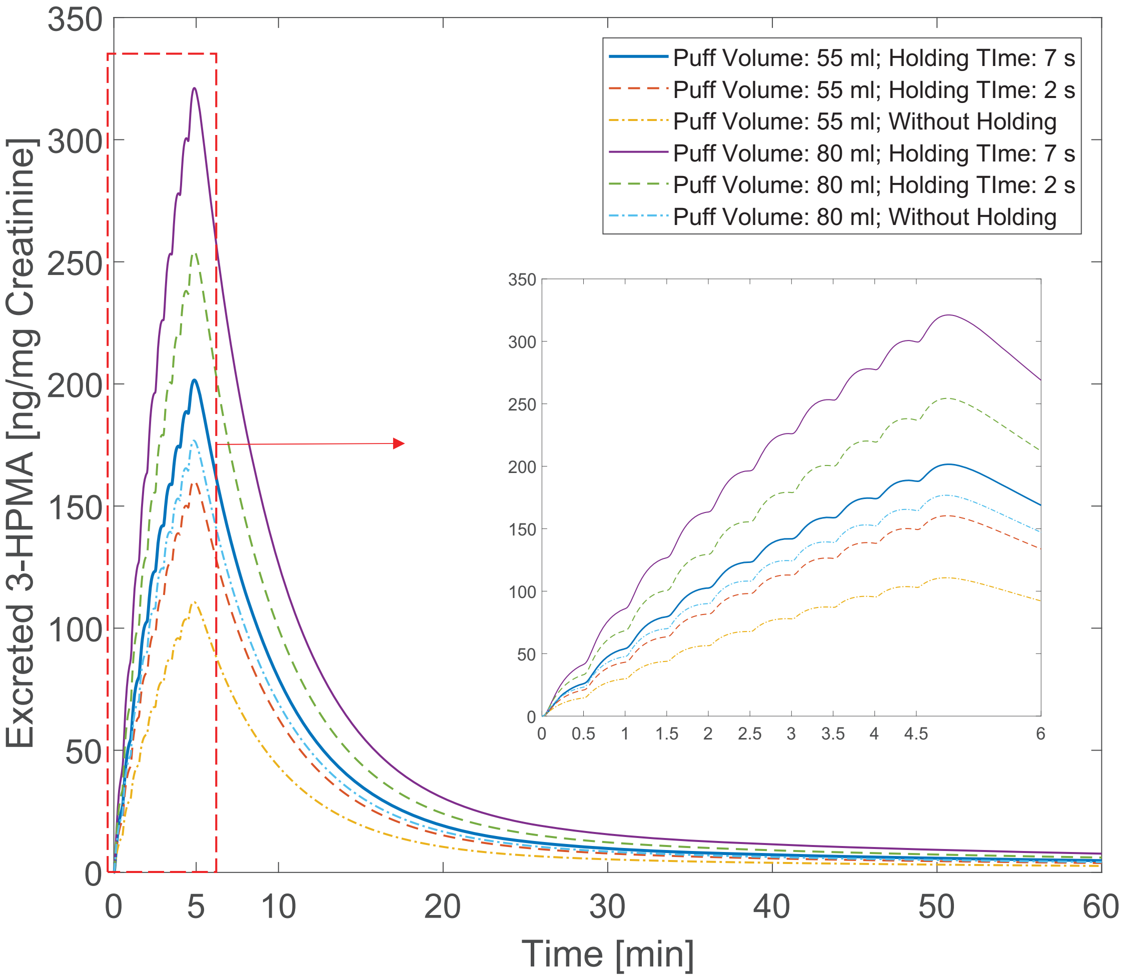

Figure 1.16: Time courses of the ratio between excreted 3-HPMA and creatinine in the kidney with different puff topographies

Based on the simulation the excretion profile shows a peak value that is suggested by the experiments (Shahab et al., 2017; Goniewicz et al., 2017). The increase in puff volume from 55 to 80 ml for a case without holding time has contributed to 59.63% increase. However, by increasing the holding time for the case with 55 ml puffing volume, the peak value increase is approximately 82.03%. This difference can depict the importance of the holding time that can contribute to a significant change in translocation magnitude in the human body. Existing standards of the puffing machines have focused mostly on three parameters: puff volume, duration and interval time. Therefore, the importance of the additional parameter that must also be investigated in the futural experiments. Other parameters may include EC product type (McNeill et al., 2015), and interaction between EC chemicals (Kane and Alarie, 1978).

1.7 Conclusions

In this study, a multiscale CFPD-PBTK model is developed and applied to accurately predict multicomponent EC aerosol transport, deposition, and translocation from the human respiratory system to systemic regions. Specifically, aerosol dynamics was modeled by the CFPD model established based on the Euler-Lagrange scheme. A 9-compartment PBTK framework subsequently simulates the translocation of nicotine and acrolein in systemic regions. Also, a diffusion-limited model was utilized to simulate the in tissue translocation of formaldehyde and acrolein at the epithelial and subepithelial layers. Employing the CFPD-PBTK model, it is the first time that *in silico* investigations can reflect realistic EC vaping scenarios, i.e., multiple puffs with real EC user behaviors. The model advances the field of aerosol exposure science to pave the way to a valuable computational simulation tool for assessing the long-term health effects of inhaled e-cigarette toxicants in the human respiratory pathway and systemic regions. Quantitative data of EC toxicant fates to the health endpoints are generated and discussed. Based on the numerical results, conclusions and novel insight are summarized as follows:

1. Most of the vaporized nicotine and acrolein are absorbed in the upper airway from mouth to G1. In contrast, EC aerosol particle deposition occurs in all regions from mouth to G3.

2. Both particulate and vapor forms of nicotine and acrolein contribute to the deposition and translocation in the human body.

3. The increase from 55 to 80 ml puffing volume results in a significant increase in

the peak nicotine and acrolein plasma concentration as 21.2% and 59.45% for the cases without holding.

4. With fixed puffing volume, increasing holding time will result in the increase of peak plasma concentration for both nicotine and acrolein.
5. Holding time between consecutive puffs has significant impacts on the EC aerosol deposition and translocation. Therefore, it is necessary to include holding time in both experimental and numerical studies to provide accurate predictions.

1.8 Limitations of the Study

Due to the complexity of the realistic EC aerosol dynamics in the human body, limitations exist for the current CFPD-PBTK simulations. The assumptions employed are:

1. Spherical particle with constant diameter is assumed
2. The effect of evaporation/ condensation is neglected.
3. The deposition and uptake due to exhalation cycle are not simulated.
4. The complete conversion of the acrolein to 3-HPMA is not modeled.
5. The Cotinine as the main metabolite of the nicotine is not modeled in PBTK simulation.
6. The bioavailability factors have been used to connect the CFPD to PBTK models. This fraction was hypothesized to combine the influence of the reaction, diffusion and the lymph vein concentration at regional contact with the lung tissue.
7. Square waveforms are selected as puffing inlet conditions.

8. The time delay effect of the closed loop system of the human body organs configuration is not considered.

1.9 Future Work

Future work will focus on the improvement of the CFPD-PBTK model considering more complex aerosol dynamics. The next generation CFPD-PBTK model will include the coagulation, condensation, and evaporation among phases. The interconnection model will be developed for different pulmonary regions, to reflect the different diffusion and reaction characteristics. Additionally, subject-specific human airway configurations will be used for vulnerable subpopulation groups to EC products, e.g., adolescents, and COPD patients. To improve the current PBTK model, the couplings among compartments will be considered to simulate the realistic time delay effects in different organs.

CHAPTER II

Deposition and Replication of Low-Strain Influenza A Virus in the Epithelium of a Subject-Specific Virtual Human Upper Airway Model

2.1 Introduction

Influenza virus (IV) can cause respiratory infection and fatal incidences among many species including humans, birds, swine, and horses. Fever, rhinorrhea, sore throat, and muscle aches are some of the common symptoms among IV infections (Boianelli et al., 2015). The airborne transmission and pulmonary deposition of virus-carrying droplets impose a warning sign to the preexisting cellular immune system, which is a complex and nonlinear interaction of the host cells and antigen structure. Meanwhile, the underlying principles of how various IV strains cause different pathogenic profiles is still unknown. Therefore, prediction of the anatomical compartments and the respiratory epithelium regional behaviors of IV replication is necessary for virus characterization and vaccine cultivation.

IV uses RNA as a genetic blueprint to synthesize DNA from other organisms. Its RNA protein structure defines the type of virus (Type A, B, C, and D). Type A transmits between species and has recorded severest diseases (Klenk et al., 2008). The subtypes of influenza A virus (IAV) depend on the response of the host antibody to the antigens hemagglutinin (HA) for binding the virus to the infected cell and neuraminidase (NA) for dispersing the virus progeny from the infected cell. Because of the variety of zoonosis and wildlife intermingling, it is complicated to study the origin of IAV and eliminate the chance for virus to transmit to human (Cox and Subbarao, 2000). Furthermore, binding of the virus replicase to the host cell, and the morphing of the virus strains can result in the synthesize of a novel generation. In addition, antigenic drifts and shifts influence the IAV replication (Carrat and Flahault, 2007). The IAV pandemic outbreaks in the last century showed that when a novel strain of virus transmits from animal to humans, it is resistant to the known antibody medications. Therefore, a severe and fatal infection can happen.

Among the IAV subtypes, the combinations of HA (1, 2, 3, 5, 7, 9) and NA (1, 2) proteins can construct different strains of IAV that infect human (Thompson et al., 2009; Zens, 2017). The U.S. Center for Disease Control and Prevention (CDC) recently examined a number of infected species with different subtypes of IV in a two-month period and indicated that IAV H3N2 and H1N1 caused noticeably higher infection rate (Dugan et al., 2017). The IAV subtype determines the infection site at the airway tissues, and its protein structure determines the proteases that cleave to the virus HA protein to activate the fusion precursors of IAV (Steinhauer, 1999). For lower strains IAV subtypes, cleavage happens in the upper airways, especially in the epithelial lining cells of pharynx and trachea. For highly virulent pathogenic strains, e.g., avian influenza H5N1, the HA protein can be cleaved by a wide variety of proteases and the virus can reach the distal sections of the respiratory system and subsequently spread to post-epithelial tissues (Korteweg and Gu, 2008; Van Riel et al., 2006). Assessing the infection site is essential to determine the tendency of the virus resuspension and transmission through an infected subject's cough or sneeze (Shinya et al., 2006; van Riel et al., 2007). For example, IAV subtypes with lower strains are distinguished by having the ability to pass among humans through the air in the droplet form targeting the upper airways as infection "hotspots". In contrast, negligible virus migration is expected for higher strain IAV subtypes.

The airborne transmission of IAV is possible, as long as the virus-laden droplets remain suspended in the air (Eames et al., 2009). Once the droplets deposit on the mucosa lining of the pulmonary tracts, they bind to the surface of targeted epithelial cells. The endocytosis of the virions inside the epithelial cell occurs after 20 minutes post-infection (Oguin et al., 2014). At this stage known as the incubation period, the virus binds to the epithelial cell for cloning and reproducing copies of RNA and viral proteins. The Eclipse phase (Pinilla et al., 2012) is the period between post-infection and reproducing stage, when the viral progenies leave the infected cell. The duration of this phase is predicted from 5 to 12 hours post-infection (Beauchemin and Handel, 2011) and can reach its peak value after 2 to 3 days post-infection (dpi) (Boianelli et al., 2015). Afterward, two different immune subsystems, i.e., innate and adaptive immune systems (IIS and AIS, respectively), will activate and interfere with the antigen replication.

Lymphoid tissues and leukocytes are responsible for the immune response. The main form of cellular immunity includes lymphocytes (e.g., natural killer (NK) cells) and phagocytes (e.g., macrophage and mast cells) (Male et al., 2006). The IIS has a fast response with non-specific antigens without selectivity. Physical and chemical barriers such as cellular defense and leukocytes are in the IIS group. The AIS is selective to the specific virus types and with antibody-mediated humoral, and cell-mediated immune response that is cytotoxic lymphocytes. The most critical factor in the IIS is the type I interferon (IFN)-I production (Baccam et al., 2006) by the invaded cells to hinder the viral replication. The released (IFN)-I works as a signal (De Andrea et al., 2002) to increase antiviral enzymes in the neighboring healthy cells. Likewise, interferon (IFN) indirectly helps the phagocyte and enhances the functionality of NK cells and cytotoxic T cells. NK cells are responsible for killing the infected cells and stop the virus reproduction. NK cells and cytotoxic T cells share similar functionality and performance that makes it possible to represent the effects of both cells using the same factor. The cytotoxic proteins bind to the infected cell membrane and degranulated to lysis the infected cells. Inactive AIS cells are available in peripheral lymphoid tissues. Bursal-equivalent lymphocyte (B cell) and thymus-derived lymphocyte (T cell) receptors bind to the antigen (through producing antibodies) and the infected cells, respectively (Miller and Mitchell, 1969). The receptor binding process needs T cells to detect the selected major histocompatibility complex (MHC) molecules for responding to the infection site. This process makes the selectivity of the T cells recognizable. There are three major types of T cells: T helper cells with surface protein CD4+, cytotoxic T cells that mostly contain CD8+ surface protein, and regulatory T cells. The surface protein CD4+ from T helper cells secrete cytokines that directly enhance the functionality of the macrophage and NK cells. Meanwhile, CD8+ cells directly lyse infected cells as NK cells by releasing perforin and granzymes. The regulatory T cells are responsible for deactivating AIS after IAV infection at the end of the viral life cycle. Altogether, (IFN)-I, NK cells, pathogen-specific antibodies due to B cells functionality (Abs), and cytotoxic CD8+ T cells are the most noticeable components in the immune system that control the IAV infection (Baccam et al., 2006). Immune subsystem responses and processes are in a collocative multi-directional state compared to each other that any changes in a factor would influence the enhancement or suppression of the others.

Mathematical models for the viral dynamics within the host were developed with various considerations for the interactions between the targeted cell, immune system, and viral agents (Beauchemin and Handel, 2011; Smith and Perelson, 2011). The first attempt to numerically represent the host cell dynamics (HCD) was done by Larson et al. (1976) after fitting the data from IAV H3N2 infected Swiss-ICR mice. The viral doses in the lung, trachea, and nasopharynx were investigated with five associated rate parameters. Formulating the HCD using target cell models (Nowak and May, 2000) was used for the IV infection study. Baccam et al. (2006) adopted target cell models by including susceptible cell, infected cell, and virus to fit a model with the *in vivo* data of the virus A/Hong Kong/123/77 (H1N1) infected human. Specifically, eclipse phase was included by considering a latent phase for the infected cell before becoming productive. Their numerical results indicate that the virus reproduction started at 6 hours post-infection, and the infected cells lifetime was 11 hours. Holder and Beauchemin (2011) investigated the same mathematical model for validation of *in vitro* study and suggested a more complex parameter for the infected cells in delayed phase. Petrie et al. (2013) developed a double target cell model for human infections with avian strain by differentiating target cells into two fractions, i.e., default and secondary cells. The response from the immune system by proposing the effect of antibodies (Abs) and CD8+ T cells was first introduced into the model by Bocharov and Romanyukha (1994). Baccam et al. (2006) included the (IFN)-I dynamics, and their results show double peaks in viral titer data. Moreover, the additional factor of NK cells was introduced to the target cell models by Canini and Carrat (2011), where the NK activation is induced by (IFN)-I. Specifically, the virus kinetics and symptom dynamics population have been utilized to estimate infection parameters. Including the AIS with CD8+ T cells and Abs into the cell population models were modeled by Lee et al. (2009). Specifically, a lymphatic compartment was considered to represent the activation of T and B cells. In this regard, 10 equations for the kinetic of AIS components at different stages were added to the target model, and the optimum time of antiviral drug administration was proposed to be at 2 dpi.

In vitro studies reduce the complexity of the biological system and help to develop mathematical models to fully represent the biological functions. However, validity and comparability of 2D and 3D cell culture systems with the realistic cell growth media is controversial. Furthermore, Baccam et al. (2006) identified interspecies variabilities of the IAV transmission and replication. The *in vitro* study on the primary IAV infection of mice showed the peak response and release of (IFN)-I after 7 dpi, and the peak population of CD8+ T cells were observed at 10 dpi (Tamura and Kurata, 2004; Hufford et al., 2012). For pig, the peak population of both CD8+ and CD4+ T cells were indicated at 5 dpi (Lange et al., 2009). In the nasal wash of H1N1 and

H3N2 infected ferret, with the closest similarity to human IAV infection, the peak viral population was determined at 2 dpi. In this regard, it is imperative to consider human *in vivo* studies for validation and parametric optimization. Previously *in silico* studies were developed for IIS (Beauchemin and Handel, 2011; Hancioglu et al., 2007; Le et al., 2015), and AIS (Antia et al., 2003; Bocharov and Romanyukha, 1994), and both sub immune systems by Handel et al. (2007) and Lee et al. (2009) that can be modified with care for the human infection studies.

Airborne transmission of the IAV-laden droplets occurs when the viral load migrates through nasal and mouth breathing or paranasal sinuses (ocular route) to the airways. The airborne transmission of infectious substances expelled by an infected subject is commonly known to be the decisive contagion mechanism. The respirable fomites carrying IAV are reported to be 1 to 100 μm in diameter (Blumenkrantz, 2014). Lambert et al. (2011) performed a multiphase computational fluid particle dynamics (CFPD) model for spherical rigid and pure water droplets, with a diameter of 2.5 μm. Exposure through mouth breathing showed a higher deposition at the upper airway and the primary bifurcation. The CFPD models determined the particles greater than 6 μm deposited in the upper respiratory tract. Those particles between 2 to 6 μm mostly deposited in the 2^{nd} generation (G2), and smaller particles would reach lower lobes (Darquenne, 2012; Ou et al., 2017).

The hygroscopic growth and shrinkage of particles in humid air have been investigated thoroughly in climate science (Kreidenweis et al., 2005; Mikhailov et al., 2004). Aerosol size change dynamics were studied in an idealized upper airway geometry up to G3 (Feng et al., 2016; Zhang et al., 2006), in the subject-specific human upper airway geometry excluding the nasal cavity (Worth Longest and Xi, 2008), and the nasal cavity only (Schroeter et al., 2016). The results showed the evaporation and condensation of droplets were dependent on the droplets composition and the ambient relative humidity (RH), temperature, and pressure. Droplet trajectory depends on the airflow patterns. In detail, breathing through mouth or nose changes the local airflow, and consequently, the droplet heat and mass transfer. To our knowledge, this study is the first *in silico* IAV transmission study integrating CFPD, HCD, the droplet size change dynamics due to evaporation and condensation.

2.2 Methodology

Here, we develop and validate a multiscale model using CFPD and HCD to simulate the transport of the respirable IAV-laden droplets and to predict the immune system response at a time span of 12 dpi. The proposed multiscale model contains two simulation layers connected at the airway mucosa lining as the viral replications start from the deposition of inhaled fomites on the epithelial cells. The virus deposits on the mucosa lining to bind to the targeted epithelial cells surface. Since the infection replication is significantly dependent on the host cell population and immune system agents at each region, a CFPD model with the Euler-Lagrange scheme is adopted to simulate the virus-laden droplets transportation and deposition. The deposition "hotspots" are calculated and coupled with the HCD model to determine the regional host dynamic information.

Figure 2.1 provides the context of the multiscale model. The polyhedral-core mesh is developed and compared with the tetrahedral-core mesh. The final mesh has 18,453,311 polyhedral-core plus prism layers elements. The inhaled number concentration of droplets after exposure to sneezing event by the infected subject is estimated based on a separation distance of 3 feet for a successful infection transfer (Hamborsky et al., 2015; Liu et al., 2017). The indoor condition with artificial heating at the winter time is set up for the inhalation condition (Knight, 1980). The unimodal virus carrying respiratory droplets number concentration and mean diameter are defined as 6 bins with average values reported by Duguid (1946). Two routes of inhalation, i.e., mouth and nasal breathings, are simulated using realistic human breathing patterns

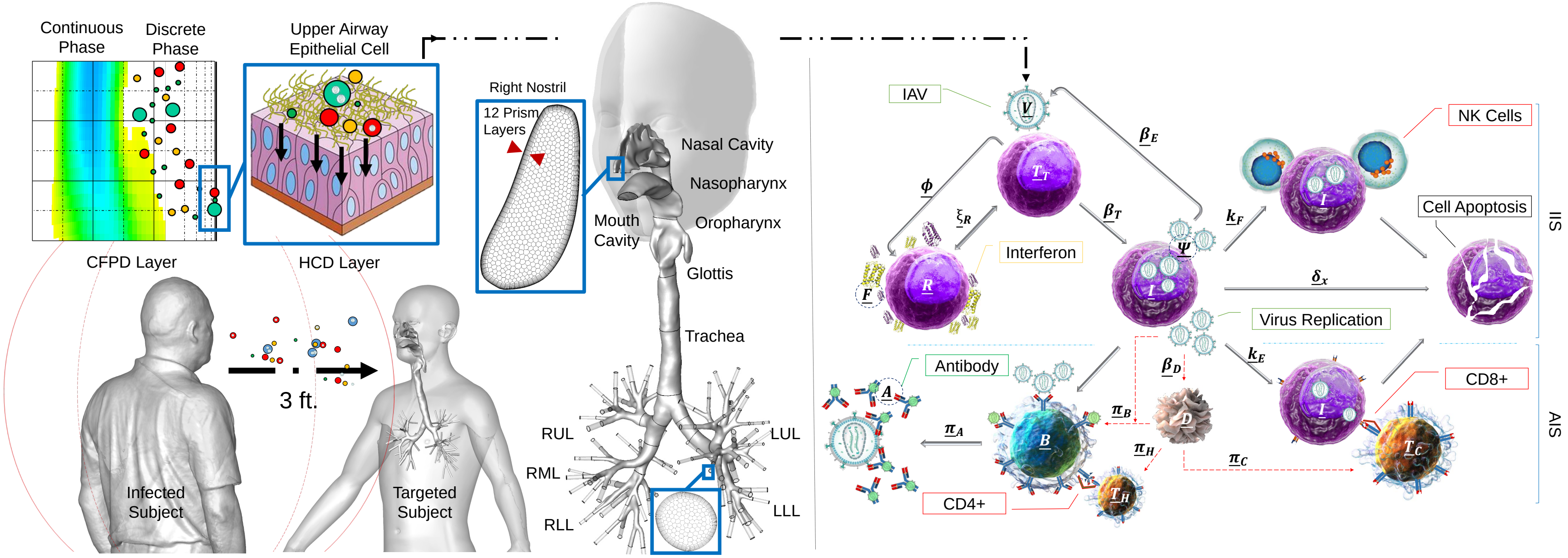

Figure 2.1: The framework of the multiscale CFPD-HCD model for the human-to-human IAV infection with a subject-specific airway geometry. The description of the HCD model is given in Section 2.3.2. The detail of the final polyhedral-core mesh is provided at the right nostril and a lobar outlet (RUL: right upper lobe, RML: right middle lobe, RLL: right lower lobe, LUL: left upper lobe, LLL: left lower lobe).

consist of a complete inhalation-exhalation cycle. Moreover, the mass and energy transfer between the respiratory droplet, i.e., the discrete phase, and the continuous humid air phase are considered to govern the droplets hygroscopicity. This consideration is made possible by applying the principles of cloud physics to the transported nanoscale sneezing event droplets. As the interphase transfer of droplets is extensively dependent on their compositions, three different concentrations were selected for NaCl and water, as major components of the coughing or sneezing droplets (Effros et al., 2002). The list of cases with different droplet compositions in mass fractions is as follows:

- Realistic nasal breathing (NB) exposed to a sneezing event:
    - Case 1: 100.0% water - 0.0% NaCl,
    - Case 2: 93.2% water - 6.8% NaCl (Schaffer et al., 1976),
    - Case 3: 89.6% water - 10.4% NaCl (Yang and Marr, 2011),
- Realistic mouth breathing (MB) exposed to a sneezing event:
    - Case 4: 100.0% water - 0.0% NaCl,
    - Case 5: 93.2% water - 6.8% NaCl,
    - Case 6: 89.6% water - 10.4% NaCl.

2.3 Governing Equations

2.3.1 Computational Fluid-Particle Dynamics (CFPD)

The transport of IAV-laden droplets from human-to-human is carried out by the airstream of an infected person's sneeze. Due to a low volume fraction of the droplets in the airstream, a Euler-Lagrange scheme is adapted. Moreover, the interaction of the phases is implemented by considering the hygroscopic growth (condensation) and shrinkage (evaporation) of droplets traveling through the pulmonary route. These effects append to the conservation equations of each phase as the mass and energy source terms.

2.3.1.1 Euler Phase: Airflow

The flow pattern in the subject-specific human respiratory system reconstructed from the computer tomography (CT) scans showed transitional flow patterns between turbulence and laminar, at the nasopharynx and the onset of the epiglottis (Feng et al., 2018). Accurate predictions of the airflow field is important to analyze the deposition patterns at the subglottal regions (Ma and Lutchen, 2009).

In this study, transition shear stress transport (SST) model (Menter, 1994) is employed that takes the ability of the $k - \omega$ model in representing the near-wall boundary layers and is combined with the $k - \epsilon$ model to solve the freestream airflow (Langtry and Menter, 2009). The 4-equation SST model is based on the transport equations for kinetic energy(k) and dissipation(ω). The governing equations for the momentum balance are provided in Section 1.3.1.1.

At the ambient temperature and pressure, governing equations for the mass conservation of the gas mixture are defined by the advection-diffusion equation:

$$\frac{\partial \rho Y_s}{\partial t} + \frac{\partial \rho u_i Y_s}{\partial x_j} = -\frac{\partial J_s}{\partial x_j} + S_s^m \tag{2.1}$$

in which Y_s is the species mass fraction. ρ is density of the Euler phase mixture, u_i is the mixture stream velocity components, and x_j is the direction components. The mixture is a combination of air, water vapor, and an insignificant amount of NaCl in vapor form, i.e., negligible detachment of NaCl molecules from the surface of the aqueous droplet. J_s shows the mass diffusion flux of species due to concentration gradient, and to calculate J_s, Fick's law in turbulent flow for the dilute vapor mixture can be written as

$$J_s = -\left(\rho D_s^m + \frac{\mu_t}{Sc_t}\right)\frac{\partial Y_s}{\partial x_j} \tag{2.2}$$

where D_s^m is the molecular diffusivity of the species in the Euler phase. $Sc_t = \frac{\mu_t}{\rho D_t}$ is the turbulent Schmidt number, and D_t is the turbulent diffusivity and μ_t is the turbulent viscosity. In this study, Sc_t is defined as a constant value of 0.9 (Zhang et al., 2012a). In Eq. (2.1) S_s^m [kg/m^3/s] is the mass source term, i.e., the rate of species mass transfer between the phases.

The conservation of energy for the air-vapor mixture is given by

$$\frac{\partial \rho c_p T}{\partial t} + \frac{\partial \rho u_i c_p T}{\partial x_j} = \frac{\partial}{\partial x_j}\left((k_c + k_{c,t})\frac{\partial T}{\partial x_j} - \sum_s h_s J_s\right) + \Phi_{vd} + S^T \tag{2.3}$$

where c_p, T, Φ_{vd}, k_c, and $k_{c,t}$ are the gas mixture specific heat, cell center temperature, viscous dissipation, gas mixture conductivity, and turbulent thermal conductivity, respectively. Moreover, $k_{c,t} = \rho c_p \mu_t / Pr_t$, in which the turbulent Prandtl number is $Pr_t = c_p \mu / k_c$. h_i is the sensible enthalpy of the species calculated by considering 298.15 K as the reference temperature. μ is the gas mixture molecular dynamic viscosity.

With the unsteady particle tracking in a local control volume (dV), two different time steps are defined. t_f is the continuous fluid time step at the current iteration of the implicit solver, and t_d is the unsteady discrete phase (DP) tracking time iteration. Transient calculation of the interphase source terms using implicit solver is performed by advancing the DP at the beginning of the continuous phase time step. For the mass source term

$$S_s^m = \sum_{parcels}\left(\left(\dot{m}_d^0/m_d^0\right) N_{d/parcel}\int_{t_f^0}^{t_f^0+\Delta t_d}\frac{dm_d}{dt_d}\,dt_d\right)/dV \tag{2.4}$$

where $N_{d/parcel}$ is the number of droplets at each "parcel", i.e., a combination of droplets with the same diameter existing in the same volume control. Also, $\dot{m}_d^0$ and m_d^0 are initial mass flow rate and mass of the injected DP. dm_d/dt_d shows the rate of mass transfer between the continuous phase and the DP (dm_d/dt_d is negative for condensation and positive for evaporation).

The energy source term S^T [W/m^3], i.e., the volumetric energy source, is calculated by defining the latent heat of evaporation and condensation between the phases:

$$S^T = \sum_{parcels} \left(\left(\dot{m}_d^0 / m_d^0 \right) N_{d/parcel} \left[H_{lat} \int_{t_f^0}^{t_f^0 + \Delta t_d} dm_d + E_{in-out} \right] \right) / dV \tag{2.5}$$

$$E_{in-out} = m_d^{t_f^0} \int_{298.15}^{T_d^{t_f^0}} c_p dT_d - m_d^{t_f^0 + \Delta t_d} \int_{298.15}^{T_d^{t_f^0 + \Delta t_d}} c_p dT_d \tag{2.6}$$

where H_{lat} is the latent heat of energy exchange between the phases. The subscripts of t_f^0 and $t_f^0 + \Delta t_d$ show the flow time step at the inlet and outlet of the control volume. In addition, to distribute the effect of the mass and energy source terms of the parcel to neighboring mesh nodes, the nodes-per-cell averaging was performed for the continuous phase by dividing S_i^m and S^T by the number of mesh nodes at each control volume. The advanced averaging technique results in better stability in the calculation of mass and energy equations.

2.3.1.2 Lagrange Phase: IAV-laden Droplets Transport

At the ambient condition, with the dilute suspension of droplets in the airflow phase and negligible droplet rotation, the multicomponent unsteady DP tracking is performed by calculating a series of equations: translational equation, recovery of turbulent fluctuations as encountered by the DP, and the mass and energy conservation equations. Translational equation of DP is given as

$$\frac{d}{dt_d}(m_d u_{d,p}) = F_p^D + F_p^L + F_p^{BM} + F_p^G \tag{2.7}$$

where subscripts of d and p are related to the DP and each droplet (or parcel), respectively. The superscripts of D, L, BM, and G represent the drag force, lift force, Brownian motion force, and gravity, respectively. The detail of each force acting on the spherical droplet is provided in Chapter I.

Calculation of forces on the droplets was accurately calculated by recovering the fluctuation velocity (Feng and Kleinstreuer, 2013). The so-called "eddy lifetime" model that assumes the interaction of particles with turbulence eddies is identified by the Gaussian probability distribution of fluctuation velocity ($u_i' = G_{u'}\sqrt{\overline{u_i'}^2}$) and the lifetime of the turbulence eddies given as (Daly and Harlow, 1970):

$$\tau_{E-L} = C_\mu \frac{\kappa}{(0.09\kappa\omega)} \approx \frac{0.30}{(0.09\omega)} \tag{2.8}$$

However, one should take caution when calculating the acting forces on the DP forces and subsequently, the DP deposition near the walls as the fluctuating velocity normals to the wall can be overestimated. This error is due to the assumption of turbulence isotropy, and the near-wall correction is required to be added to the "eddy lifetime" model for the accurate DP trajectory prediction. This correction is suggested by introducing a damping function to the u_i' components for cell elements that rely on $y^+ < 10$ (Wang et al., 1999).

Mass balance equation for droplets is

$$\frac{dm_d}{dt_d} = \rho K_{mc} A_d \ln\left(\frac{1 - Y_{s,\infty}}{1 - Y_{s,S}}\right) \tag{2.9}$$

where $Y_{s,S}$ and $Y_{s,\infty}$ are the mass fraction of species s at the droplet surface and at the surrounding continuous phase, i.e., the center of the cell where the droplet is residing. A_d is the droplet surface, and K_{mc} is the mass transfer coefficient [m/s] given as

$$K_{mc} = \left[\frac{1 + Kn}{1 + (\frac{4}{3\alpha_m} + 0.377)Kn + \frac{4}{3\alpha_m} Kn^2} \right] \frac{D_s^m}{d_d^V} Sh \tag{2.10}$$

In this equation, the first parameter shows the non-continuum effect for the sub-micron droplets, where $\alpha_m = 1$ is the mass accommodation coefficient (Hinds, 2012) and the Knudsen number is defined as $Kn = 2\lambda/d_d^V$, in which, λ is the mean free path of the continuous phase gas mixture, and d_d^V is the mass equivalent droplet diameter calculated from the volume of the droplet (volume of the droplet is derived by having the mass and density of the droplet).

In addition, Sherwood number, Sh, is specified as (Whitaker, 1972)

$$Sh = 2.0 + \left(0.4 Re_d^{1/2} + 0.006 Re_d^{2/3} \right) Sc^{0.4} \left(\mu/\mu_{d,S} \right)^{1/4} \tag{2.11}$$

where Re_d is the droplet Reynolds number ($Re_d = \rho_d \left| u_i - u_i^d \right| d_d^V/\mu$) in which ρ_d is the droplet density and u_i^d is the droplet velocity components. Also, μ and $\mu_{d,S}$ are the gas mixture viscosity at the temperature of the cell center where the droplet is residing and at the droplet surface temperature, respectively. In Eq. (2.9), $Y_{s,S}$ needs to be calculated by specifying the thermodynamic equilibrium state between phases.

The threshold between the evaporation and condensation processes is defined by the thermodynamic properties of the droplet, i.e., equilibrium partial vapor pressures, the temperature at the dew point, and mass fraction of droplet components. Any droplet that falls under d_d^V=0.01 nm, i.e., 0.05% of the IAV minimum diameter, is considered to be entirely evaporated and the stochastic tracking calculation is halted for the droplet.

At the continuous phase cell temperature, the equilibrium of partial vapor pressure over the spherical droplet is governed by two factors. The Kelvin effect, i.e., to include the impact of the curved liquid-vapor interface (droplet) over the vapor pressure, and the solute effects. Based on the cloud physics for the multicomponent droplet with an ionic solute the Köhler theory is given as (Mikhailov et al., 2004; Kreidenweis et al., 2005):

Hygroscopic growth and shrinkage dynamics of droplets is goverend by

$$Y_{s,S} = \frac{P_{s,S}}{P^0(T)} = \gamma_s \exp\left(\frac{4\sigma_d \overline{V_s}}{RT_d d_d^V}\right) \tag{2.12}$$

where $P_{s,S}$ and $P^0(T)$ are the vapor pressure at the droplet surface and the saturation vapor pressure of the transferred species at the temperature of the control volume where the droplet is located. σ_d is the surface tension of the droplet solution, R is the universal gas constant. Also, γ_s is the species activity coefficient and $\overline{V_s}$ is the partial molar volume of solute, i.e., NaCl, and is estimated by the following equations:

$$\overline{V_s} = \frac{MW_s}{\rho_{sol}}\left(1 + \frac{Y_{d,NaCl}}{\rho_{sol}} \frac{d\rho_{sol}}{dY_{d,NaCl}}\right) \tag{2.13}$$

$$\gamma_s = \exp\left(\vartheta_{d,s}\Phi_{d,s}MW_{d,water}\tilde{m}_{d,NaCl}\right) \tag{2.14}$$

In Eqs. (2.13 and 2.14), MW_s represents the species molecular weight, ρ_{sol} is the droplet solution density, $\vartheta_{d,s}$ is the stoichiometric dissociation number of the solute ($\vartheta_{d,s}$=2 for NaCl), and $\Phi_{d,s}$ is the molal osmotic coefficient of the solute in solution. Also, $\tilde{m}_{d,NaCl} = Y_{d,NaCl}/(MW_{d,NaCl}(1 - Y_{d,NaCl}))$ is the molality (m) of the solution. The solute effect is represented in the formulation of activity coefficient, and the Kelvin effect is shown in Eq. (2.12). For a dilute solution, Eqs. (2.13 and 2.14) can be simplified as

$$\overline{V_s} = \frac{MW_s}{\rho_{sol}} \tag{2.15}$$

$$\gamma_{water} = (1 - \varrho \frac{Y_{d,NaCl}\, MW_{d,water}}{x_{d,water}\, MW_{d,NaCl}})/x_{d,water} \tag{2.16}$$

where ϱ is the van't Hoff factor and $x_{d,water}$ is the mole fraction of water given as

$$x_{d,water} = Y_{d,water}/(MW_{d,water} \sum_{(d,s)} (Y_{d,s}\, MW_{d,s})) \tag{2.17}$$

In Eqs. (2.12 to 2.15), parameters are dependent on the temperature and composition of the droplet. In this order, the previously proposed correlations or experimental data are utilized to calculate these parameters (see Table 2.4).

Droplets energy balance is calculated as

$$\frac{dT_d}{dt_d} = \left(K_{hc} A_d (T - T_d) - \frac{dm_d}{dt_d} H_{lat} \right) / m_d c_{p,d} \tag{2.18}$$

where K_{hc} is the heat transfer coefficient. Assuming a unity Lewis number and a negligible influence of the evaporated/condensed species in DP on the gas mixture specific heat results in

$$K_{hc} = K_{mc} \frac{Nu\, k_c}{Sh\, D_s^m} \tag{2.19}$$

In Eq. (2.19), Nu is the Nusselt number given as

$$Nu = 2.0 + \left(0.4 Re_d^{1/2} + 0.006 Re_d^{2/3} \right) Pr^{0.4} \left(\mu / \mu_{d,S} \right)^{1/4} \tag{2.20}$$

Eq. (2.18) is based on the assumptions that the droplet is at a uniform temperature and that DP has a negligible internal resistance to the heat transfer. Also, detailed derivation and validation of Eqs. (2.9 and 2.18) are provided by Miller et al. (1998).

2.3.2 Host Cell Dynamics (HCD) Model

The epithelium cell, as the target cell, is the first contacting site of the IAV-laden droplets, and the AIS activation occurs in the lymphoid structure of the pulmonary system carried by the extra-pulmonary lymphatic vessels. Handel et al. (2007) studied the *in silico* IAV infection in humans and provided a model with seven variables for the virus, cell, and the combination of IIS and AIS. The parameter tuning was performed by fitting the virus titer experiments. In Handel et al. (2007) model, the uninfected cells were controlled by the infection rate and were decreased by a death rate, i.e., a factor of the lag time and the initial immune response. The inclusion of the IIS in the HCD model was proposed by Pawelek et al. (2012). The conversion of target cells to the refractory state, wherein cells are refractory to infection was represented by the infection decreasing frequency and the rate of antiviral release. The production of infected cells were presented by the rate of infection subtracted from the response from the NK cells. A constant AIS response rate was assumed before the emergence of AIS agents and then was exponentially increased to the maximum response. The virus growth rate was determined by the rate of change from the susceptible phase to the infected state, i.e., interfered by an increase in the population of (IFN)-I cytokines. Moreover, a simplified action of infected cell cytolysis by NK was introduced by considering a mass action term. The model proposed by Lee et al. (2009) showed the effect of AIS with considering dendritic cells as the intermediate agent between IIS and AIS. The similarity and incongruity of the three models are expressed in Figure 2.2.

In this study, the features of HCD models by Handel et al. (2007), Pawelek et al. (2012), and Lee et al. (2009) are combined (see Figure 2.2 for the underlying processes). The current HCD model variables and parameters are stated with an underbar to differentiate them from the CFPD-related parameters. The schematic of interactions between the host cells and the infectious agents is shown in Figure 2.1.

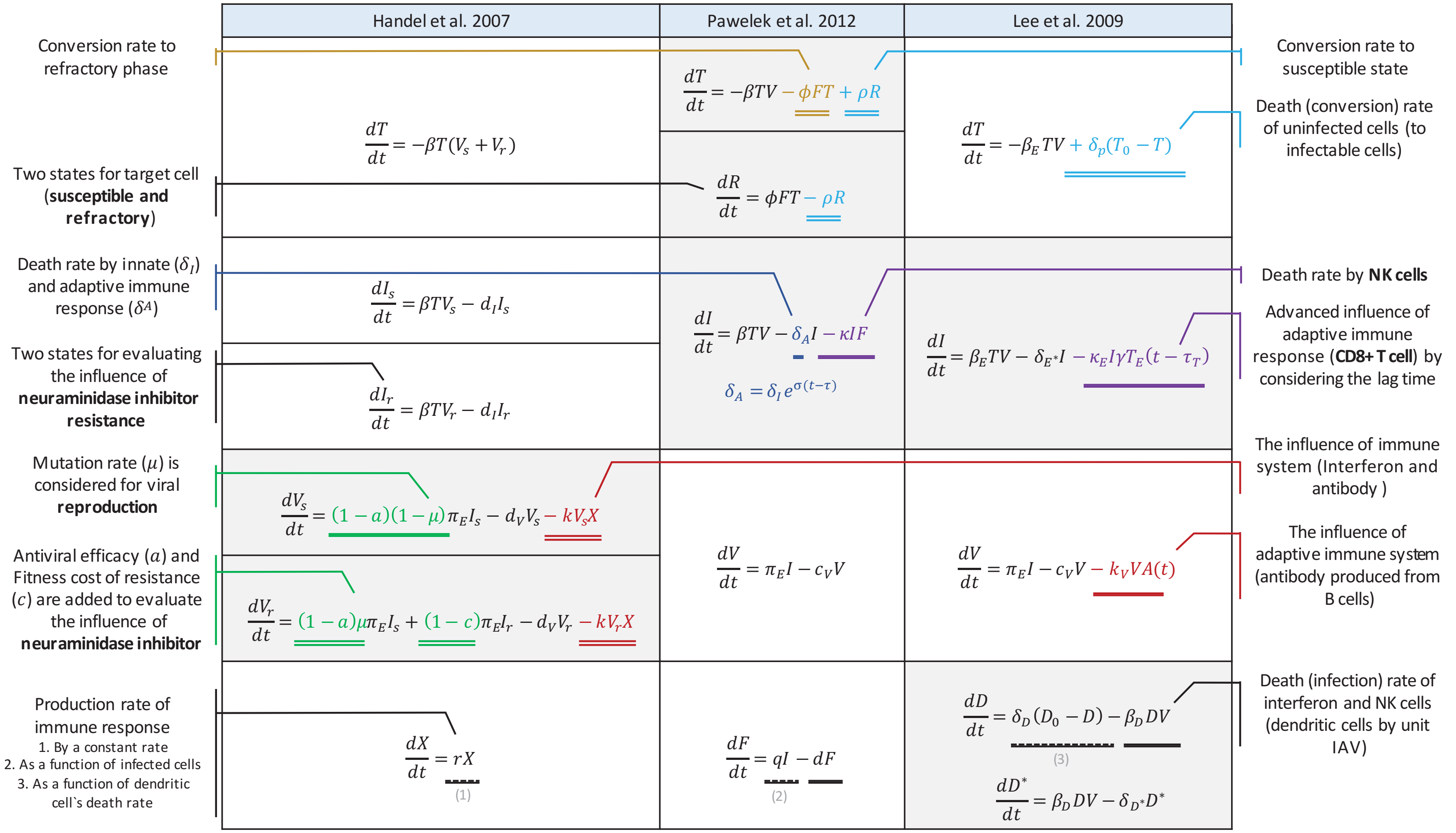

Figure 2.2: Comparison of selected IAV infection HCD models (Handel et al., 2007; Pawelek et al., 2012; Lee et al., 2009).

After the inhalation of the flu virus-load and contact with the epithelial cells ($\underline{T}_T$), viral reproduction starts. By the secretion of interferons ($\underline{F}$), the neighboring epithelial cells become refractory ($\underline{R}$) to the infection. The virus titer ($\underline{V}$) and the infected cell ($\underline{I}$) count are connected with the rate of virus replication ($\underline{\beta}_E$). $\underline{T}_T$ are infected at the rate of $\underline{\beta T_T V}$ and are converted to two states of $\underline{R}$ and susceptible ($\underline{T}_T$) which is controlled by the production of $\underline{F}$, represented as $\underline{\pi F T}_T$. In addition, to enhance the reverse action, a rate is introduced for conversion back to the susceptible phase ($\zeta_R \underline{R}$).

$$\frac{d\underline{T}_T}{dt_H} = -\underline{\beta}_T \underline{T}_T \underline{V} - \underline{\phi} \underline{F T}_T + \underline{\zeta}_R \underline{R} \tag{2.21}$$

$$\frac{d\underline{R}}{dt_H} = \underline{\phi} \underline{F T}_T - \underline{\zeta}_R \underline{R} \tag{2.22}$$

$$\frac{d\underline{I}}{dt_H} = \underline{\beta}_T \underline{T}_T \underline{V} - \underline{\kappa}_F \underline{I F} - \underline{\kappa}_E \underline{I} \underline{\gamma} \underline{T}_C - \underline{\delta}_X \underline{I} \tag{2.23}$$

$$\begin{cases} \underline{\delta}_X = \underline{\delta}_I & t_H - \underline{\tau}_A \\ \underline{\delta}_X = \underline{\delta}_I e^{\underline{\sigma}(t_H - \underline{\tau}_A)} & t_H - \underline{\tau}_A \end{cases} \tag{2.24}$$

The effect of NK cells is incorporated into the interfering action of $\underline{F}$ as $\underline{\kappa}_F \underline{I F}$. The influence of cytotoxic CD8+ T cells is represented by defining the time of emergence ($\underline{\tau}_A$) and the migration factor ($\underline{\gamma}$). Other unknown sources of IIS and AIS responses are added to the infected cell equation ($\underline{\delta}_X \underline{I}$) with a constant value ($\underline{\delta}_I$) for IIS and a transient parameter with the growth rate of $\underline{\sigma}$ for the AIS.

$$\frac{d\underline{V}}{dt_H} = \underline{\beta}_E \underline{I} - \underline{\delta}_V \underline{V} - \underline{\kappa}_V \underline{V A} \tag{2.25}$$

The $\underline{V}$ production rate is represented as $\underline{\beta}_E$ and the death rate of infection is defined by $\underline{\delta}_V$. Also, the effect of the antibodies ($\underline{\mathrm{A}}$), i.e., produced by the mature B cells, on the virus reproduction deactivation is represented by the rate of ($\underline{\kappa}_V$).

Subsequently, the $\underline{D}_M$ processes antigen and present it on the AIS components.

$$\frac{d\underline{D}_M}{dt_H} = \underline{\beta}_D \underline{D}_M \left(1 - \frac{\underline{D}_M}{\underline{K}_D}\right) \underline{V} - \underline{\delta}_D \underline{D}_M \tag{2.26}$$

$$\frac{d\underline{T}_H}{dt_H} = \frac{\underline{\pi}_{H1} \underline{D}_M}{\underline{\pi}_{H2} + \underline{D}_M} \left(1 - \frac{\underline{T}_H}{\underline{K}_H}\right) - \left(\frac{\underline{\delta}_{H1} \underline{D}_M}{\underline{\delta}_{H2} + \underline{D}_M}\right) \underline{T}_H \tag{2.27}$$

$$\frac{d\underline{T}_C}{dt_H} = \frac{\underline{\pi}_{C1} \underline{D}_M}{\underline{\pi}_{C2} + \underline{D}_M} \left(1 - \frac{\underline{T}_C}{\underline{K}_C}\right) - \left(\frac{\underline{\delta}_{C1} \underline{D}_M}{\underline{\delta}_{C2} + \underline{D}_M}\right) \underline{T}_H \tag{2.28}$$

$$\frac{d\underline{B}}{dt_H} = \frac{\underline{\pi}_{B1} [\underline{D}_M + \underline{h}(\underline{V} + \underline{T}_H)]}{\underline{\pi}_{B2} + \underline{D}_M + \underline{h}(\underline{V} + \underline{T}_H)} \left(1 - \frac{\underline{B}}{\underline{K}_B}\right) - \underline{\delta}_B \underline{B} - \underline{\delta}_A \underline{B} \tag{2.29}$$

The critical agents simplify the AIS action, i.e., CD8+ T cell ($\underline{T}_C$), CD4+ T cell ($\underline{T}_H$), and B cell ($\underline{B}$). The activation of the AIS components is considered as a function of the dendritic cell ($\underline{D}_M$) count (Lee et al., 2009). The CD8+ T cell starts the apoptosis of infected cells and B cell generates the antibodies to stop the functionality of the virus with T helper cells. Logistic growth is selected for the operation of AIS components and the maximum values for the logistic profiles are adapted from the study by Lee et al. (2009) and compared with the predicted profile for the human infection by Handel et al. (2007).

$$\frac{d\underline{A}}{dt_H} = \underline{\pi}_A \underline{B} - \underline{\delta}_A \underline{A} \tag{2.30}$$

$$\frac{d\underline{F}}{dt_H} = \underline{\beta}_F\underline{I} - \underline{\kappa}_A\underline{F} \tag{2.31}$$

Finally, the antibody and interferon population balance are presented by considering a growth rate ($\underline{\pi}_A$ and $\underline{\delta}_A$, respectively) and death rate ($\underline{\beta}_F$ and $\underline{\kappa}_A$, respectively) for each of them.

The optimized parameters with detailed description and the reported data from previous works have been provided in Table 2.1. Some of the parameters lack the physical meaning and the optimization variables were set up with the range of 1e-2 to 1e+3 compared to the data reported by the previous studies. A genetic algorithm (GA) is used to optimize the HCD mathematical system with a vast number of constraints. GA is classified as a probabilistic optimization algorithm, which is characterized by methods that encounter with the complicated relation between a solution and its fitness (Weise, 2009). The evolution usually starts from a population of randomly generated individuals. The fitness of every individual is evaluated, and the best individuals are selected from the current population. Next, each genome is modified by replacing one or more individuals with new solutions, which are created either by combining two individuals (crossover) or by changing an individual (mutation) to form a new generation (Edgar et al., 2001). Practically, by considering the appropriate generation, the population explorer of the possible domain of an optimal solution is obtained. In this research, non-sorting genetic algorithm II (NSGA-II) is selected to solve the developed optimization problem. Based on the results of the non-sorting genetic algorithm, Pareto-front is developed, and a single set of parameters is selected based on developed Pareto-front and the technique for order of preference by similarity to ideal solution (TOPSIS) as an efficient decision-making method. The objectives are the absolute error between the experimental data and the HCD model for the viral titer and the IFN count (see 2.5.2). Optimized parameters, i.e., at the biologically feasible range, are changed regarding each other and the data probing has been investigated on the global domain. The optimization and decision-making processes are executed using MATLAB ("optimtool") and in-house 4^{th} order Runge-Kutta method ODE solver.

Table 2.1: The description of optimized HCD model parameters and the reported values by previous studies.

Parameter	Definition	Reference Values	Optimized Value
$\underline{\beta}_T$	Infection rate	9.9e-2† ml (day.TCID$_{50}$)$^{-1}$ 4.7e-5$^{\ddagger *}$ (RNA copy)$^{-1}$ml NS day^{-1} 7e-5§ day^{-1}(EID$_{50}$/ml)$^{-1}$	9.89e-3 ml (day TCID$_{50}$)$^{-1}$
$\underline{\phi}$	IFN-induced antiviral efficacy	3.3e-1$^{\ddagger *}$ (IFN fold change)$^{-1}$day^{-1}	5.01e-1
$\underline{\zeta}_R$	Reversion rate from refractory	2.6$^{\ddagger *}$ day^{-1}	1.15
$\underline{\kappa}_F$	Killing rate of infected cells by NK cells	4.2$^{\ddagger *}$ (IFN fold change)$^{-1}$day^{-1}	1.24e-2
$\underline{\kappa}_E$	Killing rate of infected cells by CD8+ T cells	1.19e-3§ day^{-1}	1.29e-2
$\underline{\gamma}$	CD8+ T cells migration factor	0.15§	0.925
$\underline{\delta}_I$	Infected cell death rate	5.0e-1† day^{-1} 2‡ day^{-1} 1.2§ day^{-1}	5.02e-1
$\underline{\sigma}$	Death rate increases factor	0.99$^{\ddagger *}$	0.98
$\underline{\tau}_A$	Time at which AIS become fully functional	4.87$^{\ddagger *}$ day	1.5
$\underline{\beta}_E$	Virus production rate	1.2e-5† TCID$_{50}$day^{-1}ml^{-1} 5.3e-3$^{\ddagger *}$ RNA copies (ml NS)$^{-1}$day^{-1}cell^{-1} 1.9 EID$_{50}$day^{-1}ml^{-1}	1.80e-5 TCID50 (day ml)$^{-1}$
$\underline{\delta}_V$	Clearance rate of free virions	8.1e-2† day^{-1} 15$^{\ddagger *}$ day^{-1} 1§ day^{-1}	9.85e-1
$\underline{\kappa}_V$	Rate of IAV neutralization by unit anti-IAV antibody	4e-3§ day^{-1}titer^{-1}	6e-3
$\underline{\beta}_D$	Infection rate of Dendritic cells by unit IAV	1e-2§ day^{-1}(EID$_{50}$/ml)$^{-1}$	1.04e-2
$\underline{K}_D$	Max. value of the Dendritic cells	1e+5§	1e+5
$\underline{\delta}_D$	Death rate of mature dendritic cells	5e-1§ day^{-1}	10e-1
$\underline{\pi}_{H1}$	Max. activation rate of naïve CD4+ T cells	1.5§ day^{-1}	1.85
$\underline{\pi}_{H2}$	No. of Dendritic cells for half-maximal activation of naïve CD4+ T cells	1e+2§	1e+2
$\underline{K}_H$	Max. value of the activated CD4+ T cells	1e+5§	1.1e+5
$\underline{\delta}_{H1}$	Max. clearance rate of effector CD4+ T cells	4e-1§ day^{-1}	0.48
$\underline{\delta}_{H2}$	No. of Dendritic cells for half-maximal clearance of effector CD4+ T cells	1§	1
$\underline{\pi}_{C1}$	Max. activation rate of naïve CD8+ T cells	3§ day^{-1}	2.94
$\underline{\pi}_{C2}$	No. of Dendritic cells for half-maximal activation of naïve CD8+ T cells	1e+2§	9e+2
$\underline{K}_C$	Max. value of the activated CD8+ T cells	1e+5§	1e+5
$\underline{\delta}_{C1}$	Max. clearance rate of effector CD8+ T cells	75e-2§ day^{-1}	0.95
$\underline{\delta}_{C2}$	No. of Dendritic cells for half-maximal clearance of effector CD8+ T cells	1§	1
$\underline{\pi}_{B1}$	Max. activation rate of naïve B cells	3§ day^{-1}	3.02
$\underline{\pi}_{B2}$	No. of Dendritic cells for half-maximal activation of naïve B cells	1e+4§	1e+4
$\underline{K}_B$	Max. value of the activated B cells	1e+5§	1e+5
$\underline{\delta}_B$	Clearance rate of activated B cells	9e-1§ day^{-1}	0.9
$\underline{\pi}_A$	Secretion rate of antibody titer by unit short-lived plasma cell	6e-2§ day^{-1}	0.9
$\underline{\delta}_A$	Clearance rate of antibody	4e-2§ day^{-1}	4e-3
$\underline{\beta}_F$	Production rate of IFN	9.6e-10$^{\ddagger *}$ (IFN fold change) day^{-1}cell^{-1}	6.20e-7
$\underline{\kappa}_A$	Decay rate of IFN	1.9$^{\ddagger *}$ day^{-1}	4.6e-1

† Handel et al., 2007
‡ Pawelek et al., 2012
§ Lee et al., 2009
∗ Avg values reported by Pawelek et al., 2012

2.4 Numerical Setup

2.4.1 Geometry

The subject-specific upper airway geometry has reconstructed from the magnetic resonance imaging (MRI) scan (Zhang et al., 2012b) and the nasal cavity containing two passages, separated by the nasal septum and merged at the posterior nasal aperture, which was gathered from the MRI scan data set by Guilmette et al. (1989). These two geometries were connected at the soft palate between nasopharynx and oropharynx. For the smooth surface reconstruction, the Marching Cubes algorithm (Lorensen and Cline, 1987) was utilized with the volume-conserving smoothing method. Therefore, the upper airway, starting from the nares to the first six bronchial tree generations (G6) was modeled as a single domain. To have a fully developed flow and to prevent the reversed flow at the outlets, extending cylindrical tubes with 36-mm length are connected to the lobar outlets.

2.4.2 Mesh Independence Study: Comparison of Polyhedral and Tetrahedral Elements on the Computational Efficiency

An accurate estimation of transportation and deposition of respired aerosols depend on two major factors, i.e., the accuracy of the reconstructed patient-specific model and the realistic consideration of the computational model parameters and boundary conditions. However, enhancing the computational efficiency while preserving the accuracy of the numerical prediction depends extensively on the discretized domain element's type and size. In this study, the sensitivity of simulation results on mesh elements is evaluated for a patient-specific upper airway model. The tetrahedral mesh elements were widely used previously, however, discretizing patient-specific nasal cavity with the realistic transient inlet velocity profile requires a higher resolution, as NB at rest results in turbulent flow at the epiglottis and nasal meatuses.

The 3D image reconstructed respiratory system exhibits a volume of 173.5 ml and stored as a stereolithographic file for the input of Fluent Meshing V.19.1 (ANSYS Inc., Canonsburg, PA, USA). Several surface mesh resolutions were generated using curvature and proximity size functions with the local mesh refining at the expected regions with turbulent flow, i.e., nasal cavity and epiglottis. The curvature function limits the outward surface normal angle between adjacent elements and it leads to a denser mesh resolution at regions that have a higher degree of curvature such as superior and middle nasal concha and nasopharynx. In contrast, the proximity setting controls the number of elements at the volumetric region between faces that constitute gaps. To resolve the viscous sublayer, quadrilateral prism layers were created through two algorithms, i.e., uniform (defined the height of the first layer) and aspect ratio. Because of the gaps in the nasal cavity, the proximity handling with the preserved control on the first offset height was utilized to prevent the mesh elements collision at these regions. Overall, 19 meshes (7 tetrahedral and 12 polyhedral) were created and summarized (see Table 2.2). Mesh independence tests were performed using a steady airflow rate of 15 m/s at both nostrils, and the Langtry-Menter 4-equation transitional SST model was employed to resolve the laminar-to-turbulent flow transition regime.

The final mesh with tetrahedral-core elements had 48.6 m meshing cells. However, polyhedral-core elements had 18.4 million meshing cells, which showed a 62% reduction in the volume meshing elements. In addition, the elapsed time per iteration had decreased by 54% for the final polyhedral mesh compared to tetrahedral mesh with the same setup and computational resources. The quality of the mesh was measured through average inverse orthogonality and the average aspect ratio. The average orthogonality of the polyhedral meshes is 10 order lower in magnitude compared to tetrahedral meshes, which represent a higher quality and consequently higher accuracy. It was observed that by increasing the mesh resolution, the volume cell aspect-ratio quality between the last prism layer and the first layer of polyhedral elements increased. As a result, the aspect ratio algorithm was utilized with a higher number of layers to control the quality (see Table 2.2 meshes P7 and P6). This study demonstrated that polyhedral mesh is offering an enhanced computation efficiency, i.e., reduction of the volume cells and computational time, higher quality by having a smaller inverse orthogonal quality, and improved stability of the iterative solver due to higher accuracy and increased cell connectivity. Figure 2.3 represents the velocity magnitude field at the final mesh (P7) and the dimensionless velocity magnitude (by the maximum velocity in the field) at different planes. Plane DD' shows the most substantial difference between the velocity magnitude of different meshes, that is because this plane is located at the region with maximum flow disturbance.

For all cases, the simulation was performed on a local 64-bit Dell Precision T7910 workstation with 256 GB RAM and 2x16 3.1GHZ CPUs. The processor affinity was set to maximum using Fluent "TUI" commands to utilize all processing units on both CPUs in the Microsoft Windows system. Double precision and the second-order upwind scheme was defined for the solver, i.e., ANSYS Fluent V.19.1 (ANSYS Inc., Canonsburg, PA), with customized user-defined functions for the discrete phase forces, heat and mass source terms, and deposition and trajectory post-processing in C++.

Element Type	Mesh Name Tag	Cells	Faces	Prism Layers	Average Inverse Orthogonal Quality	Aspect Ratio (AR)	Nasal Cavity Face Average AR	Normalized Elapsed Time per Iteration	Note/Expression
Tetrahedral-Core	T1-b	6,196,131	14,298,752	5	0.2226	4.4222	1.0214	0.4760	
	T2-b	8,219,595	18,840,159	5	0.2116	4.2759	1.0221	0.5333	
	T3-b	8,473,656	19,253,466	5	0.2137	4.0584	1.0237	0.5490	
	T4-b	26,664,787	81,122,457	10	0.2101	2.9971	1.0190	1.6554	
	T1	12,832,186	28,794,205	5	0.1993	3.6761	1.0224	0.6373	
	T2	48,642,629	116,353,435	10	0.2086	2.7270	1.0146	2.1838	Similar setting as Mesh P4
	T5-b	56,479,962	123,246,664	10	0.1995	2.6173	1.0140	3.2444	
Polyhedral-Core	P1-b	2,298,098	10,805,866	5	0.0589	6.7063	1.6647	0.1695	
	P2-b	3,005,552	14,404,419	5	0.0476	6.3844	1.6484	0.2315	
	P3-b	2,937,070	14,187,956	5	0.0513	6.3339	1.6718	0.2294	Increased cell concentration at proximity regions
	P4-b	4,199,258	20,773,426	5	0.0382	5.9569	1.6471	0.3887	
	P1	4,047,942	20,023,122	5	0.0393	6.0010	1.6476	0.3829	Locally refined surface mesh compared to Mesh P4-b
	P2	6,755,273	31,211,451	10	0.0458	5.5970	1.6474	0.4281	Compare the elapsed time with Tet-core Mesh T1-b
	P3	15,539,818	72,466,647	10	0.0219	5.4763	1.5785	0.9939	
	P4	21,541,331	95,863,543	10	0.0202	4.5037	1.4773	1.3446	Smaller prisims compared to Mesh P1
	P5	34,188,995	164,966,165	10	0.0146	5.1065	1.4874	1.6468	Smaller Poly-core growth ratio comaperd to Mesh P2
	P6	15,473,931	31,675,624	12	0.1075	25.3154	27.3391	0.9937	Similar surface mesh as P3, Uniform first layer prism layer is calculated and defined
	P7	18,453,311	85,739,730	12	0.0291	14.5035	1.6010	1	The aspect ratio of the first prism layer is increased compared to P3
	P8	32,146,124	153,466,648	12	0.0120	9.8847	1.4469	1.6010	Similar to P7 with refined volume mesh

Table 2.2: The description of the generated meshes. The final mesh with tetrahedral-core (T2) and polyhedral-core (P7) elements are highlighted.

2.4.3 Initial and Boundary Conditions

2.4.3.1 CFPD Model

Two routes of inhalation were considered, i.e., mouth breathing and nasal breathing. The realistic breathing patterns were defined by regressing the volumetric flow rate per time data set provided by Scheinherr et al. (2015) for MB and Rennie et al. (2011) for NB. Both profiles represent healthy human breathing patterns when at rest. For the MB, 8-term Fourier series was used to fit the experimental data (see Figure 2.4 (b) and Table 2.3 (a)). For the NB, the summation of sines with 7-term was used to perform the best fit to the average data of the volumetric flow rate per time at each nostril (see Figure 2.4 (a) and Table 2.3 (b)).

Table 2.3: Fitted equations for the realistic breathing patterns (MB and NB).

(a) Mouth Breathing

Fourier Series with 8 Terms $Q = a_0 + \sum_{i=1}^{8} a_i cos(iwx) + b_i sin(iwx)$		
i	a_i	b_i
0	-1.462	N/A
1	19.55	60.38
2	-10.90	-0.9638
3	-1.6	7.435
4	-2.737	1.096
5	-2.057	-0.4919
6	-0.4734	0.7077
7	-0.4042	-0.8452
8	0.08115	0.6936
w =1.561		

(b) Nasal Breathing

Sum of Sines with 7 Terms $Q = \sum_{i=1}^{7} a_i sin(b_i x + c_i)$			
i	a_i	b_i	c_i
1	263.7	0.6369	3.015
2	330.7	0.1254	-3.727
3	73.19	4.86	-0.7755
4	48.58	7.822	-0.7588
5	16.06	13.33	0.03013
6	253.6	2.011	-0.4039
7	43.69	10.85	-1.085

At the sneezing event, the dispersed droplets number and diameter in the expelled sneezing event were gathered from the experimental dataset proposed by Duguid (1946). The droplet size distribution was separated into 6 bins that encompass droplets between 1 to 100 μm in diameter. The duration (t_{exp}) and volumetric flow rate (Q_{exp}) of expelled aerosol, i.e., air stream plus sneezed respiratory droplets, were

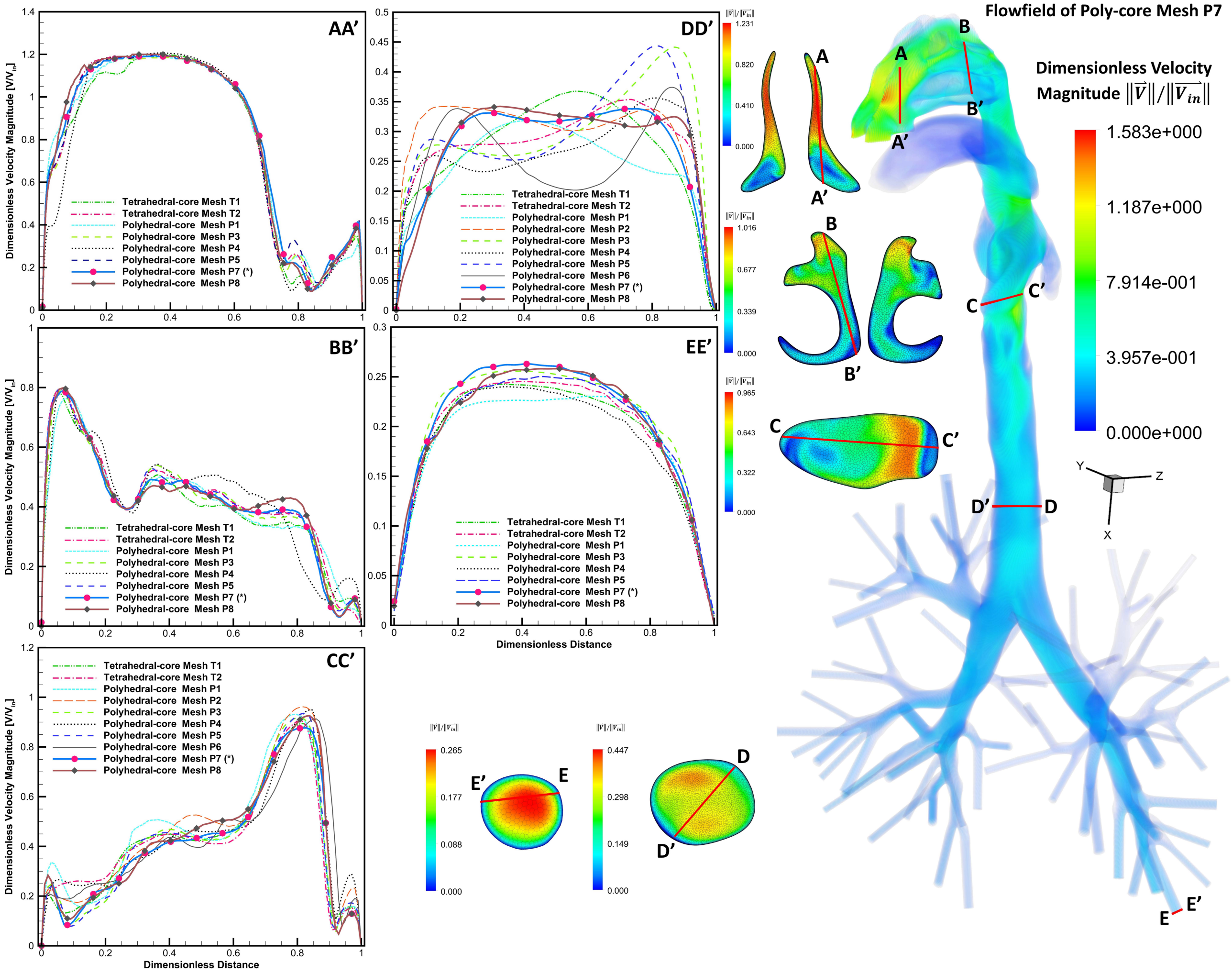

Figure 2.3: The comparision of the generated mesh at five different cross-sections and the velocity magnitude field at the final mesh (polyhedral-core 7).

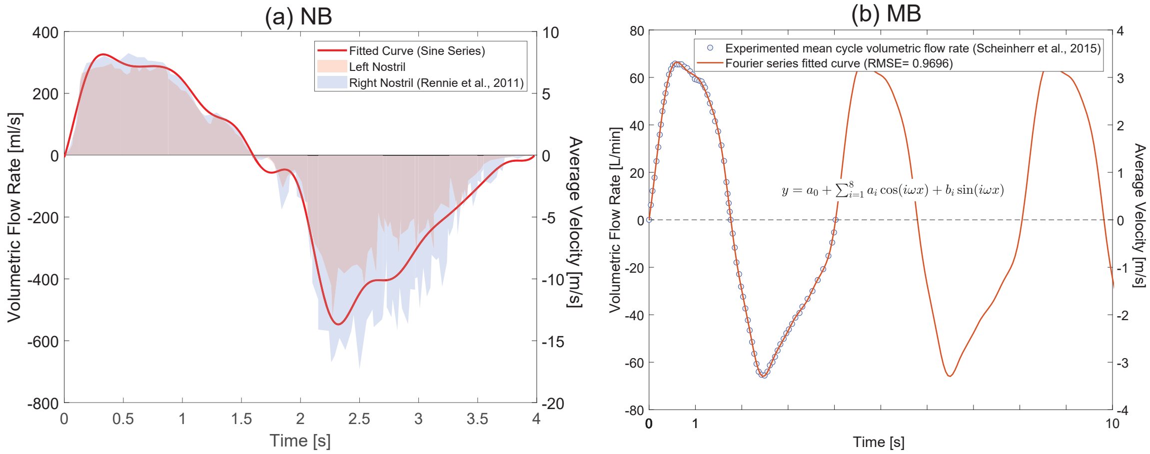

Figure 2.4: Subject-specific nasal and mouth breathing patterns. (a) NB at each nostril: the average data is collected and is fitted with the summation of sines with 7-term; (b) MB is fitted with 8-term Fourier series.

defined as 0.7 s (Han et al., 2013) and 21.5 m^3/s (Scharfman et al., 2016), respectively. To find the distance volume (V_{dis}) between the subjects, a truncated cone with 3 feet height was considered. The properties of the aqueous droplet and the initial values for the CFPD model is given in Table 2.4.

2.4.3.2 HCD Model

For the HCD model, the initial values gathered from the previous studies were used (see Table 2.5). For the calculation of the epithelium cell population at each region, the mean cell size of 2.5e-7 cm^2 reported by Farmer (1991) is considered. The post-deposition analysis of the CFPD model was decided by calculating the number of inhaled droplets that represent one tissue culture 50% infectious dose ($TCID_{50}$) of the IAV virus. Also, the biological decay of the IAV-laden droplet is considered in the experimental studies and is utilized in the model. Tellier (2009) showed 150-650 RNA copies of IAV represent 1 $TCID_{50}$. Yang et al. (2011) had estimated 2.1e+3 and 452 genome copies per $TCID_{50}$ of A/PR/8/34 (H1N1) and A/California/04/2009 (H1N1) strains, respectively. On average, the results showed the 1-hour exposure to 1.6e+4 genome copies per m^3 represents 35.4 ± 21.0 $TCID_{50}$ per m^3. In this study,

Table 2.4: The sneezing event droplet properties and the initial values for the CFPD model.

Sneezing Event	Distribution Bins (Duguid, 1946)	Droplet Diameter (d_d)[μm]	Number of Expelled Droplets
		1-2	26,000
		2-4	160,000
		4-10	420,000
		10-25	26,000
		25-50	58,375
		50-100	14,500
		+100	fall to the ground
	t_{exp} [s]	0.3-0.7	Han et al. (2013)
	Q_{exp} [m^3/s]	21.5	Scharfman et al. (2016) (from Reynolds number)
Properties	Droplet Density $f(T_d, Y_{NaCl})$	Correlation	Simion et al. (2015)
	Diffusivity $f(T)$	Correlation	Treybal (1980)
	Surface Tension $f(T_d, Y_{NaCl})$	Correlation	Weissenborn et al. (1996)
	Mean Free Path [m]	9.85E-08	water vapor - air
	Inlet Temperature [K]	310.15	
	RH%	inlet airflow: 40	airway walls: 99.5
Regional Surface Area [m^2]	Oral Cavity	4.61E-03	
	Nasal Cavity	1.37E-02	
	Oropharynx	2.21E-03	
	Nasopharynx	1.56E-03	
	Glottis	5.00E-03	
	Trachea	6.66E-03	
	Lobes (B1-G6)	4.25E-02	

the experimental data by Ward et al. (2004) is used where it showed that one TCID_{50} ml^3 holds 1000 copies of the viral genome and also each viral particulate ($d_d^0 < 1$ μm) was expected to hold one viral agent (Knight, 1980).

2.5 Model Validations

2.5.1 CFPD model

The CFPD model was previously validated by analyzing the particle trajectory and deposition on the wall boundaries (Haghnegahdar et al., 2018; Feng et al., 2018). In this study, the influence of additional mass and energy source terms on the DP is validated. The validation is performed by evaluating two different scenarios of dilute aqueous droplet evaporation and a dry NaCl particle condensation.

For the droplet evaporation, the in-house simulation is compared with the experimental data by El Golli et al. (1977). The experimental setup used a duct with concurrent airflow stream (at specified T and RH) and aqueous droplet injection with direction parallel to the gravity. Figure 2.5 shows the influence of the droplets initial molality on its evaporation and the comparison between the CFPD model with the experimental data points. The droplets were injected with the initial diameter of 16 μm to the airflow stream with RH=70%. Also, the CFPD model for two cases of pure water and 0.17 molality (m) are visualized. The droplet diameter was scaled-up for the visualization with the factor of 10e+4. For pure water, the onset of evaporation is predicted at t=737.2 ms but, for the cases with a substantial NaCl composition, the evaporation happened majorly for the water component (with a significantly low mass transfer for the salt contents). In this regard, diameter-time profiles show an exponential decrease between the evaporating region and the equilibrium stage. Neglecting the small amount of salt evaporation results in a sudden elimination of the evaporation, i.e., the equilibrium stage for the droplet. The increases in the initial molality at the injection point resulted in faster evaporation of the water contents (as the water component has a lower mass fraction in the solution) and the droplet reached the equilibrium stage in a shorter time.

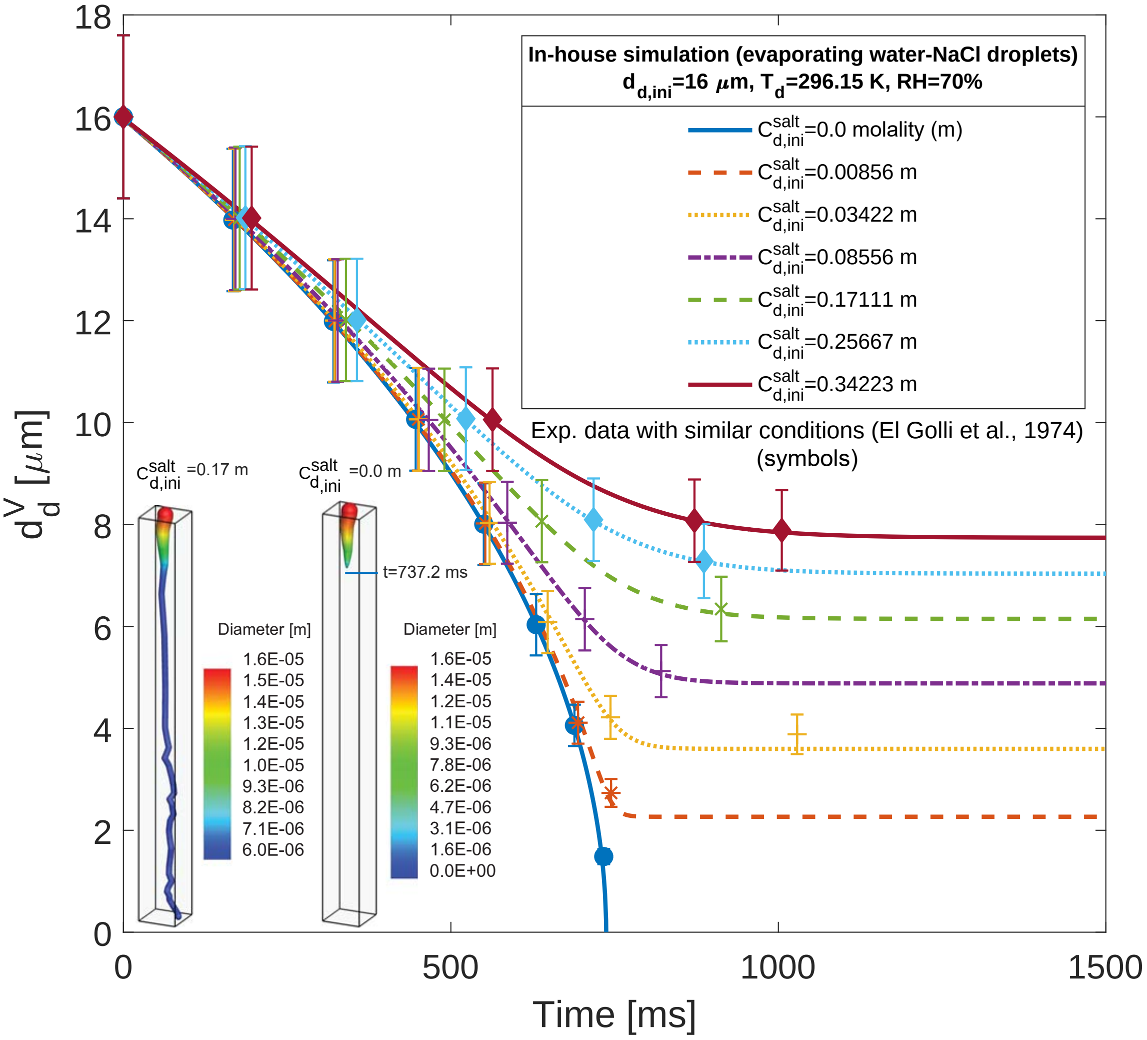

Figure 2.5: Validation of droplet dynamics containing water and NaCl with different molality (m). The CFPD model was performed on a simple rectangular duct, i.e., the experimental setup (El Golli et al., 1977).

Figure 2.6 shows the influence of the airstream RH, i.e., due to changes in the mass fraction of the vapor water, the initial diameter of the droplet, and the difference in the molality of the injected droplet on the droplets evaporation. As it was discussed previously, total evaporation of droplet has happened for the pure water droplets. The influence of the change in RH can be observed by comparing the cases 1 and 3 with a significant difference in RH as 29% and 70%. The increase in airstream

RH results in the lower partial pressure gradient, i.e., the driving force of the mass transfer between the phases. In this regard, the longer time is expected for the droplet to reach the equilibrium stage at airflow with higher RH.

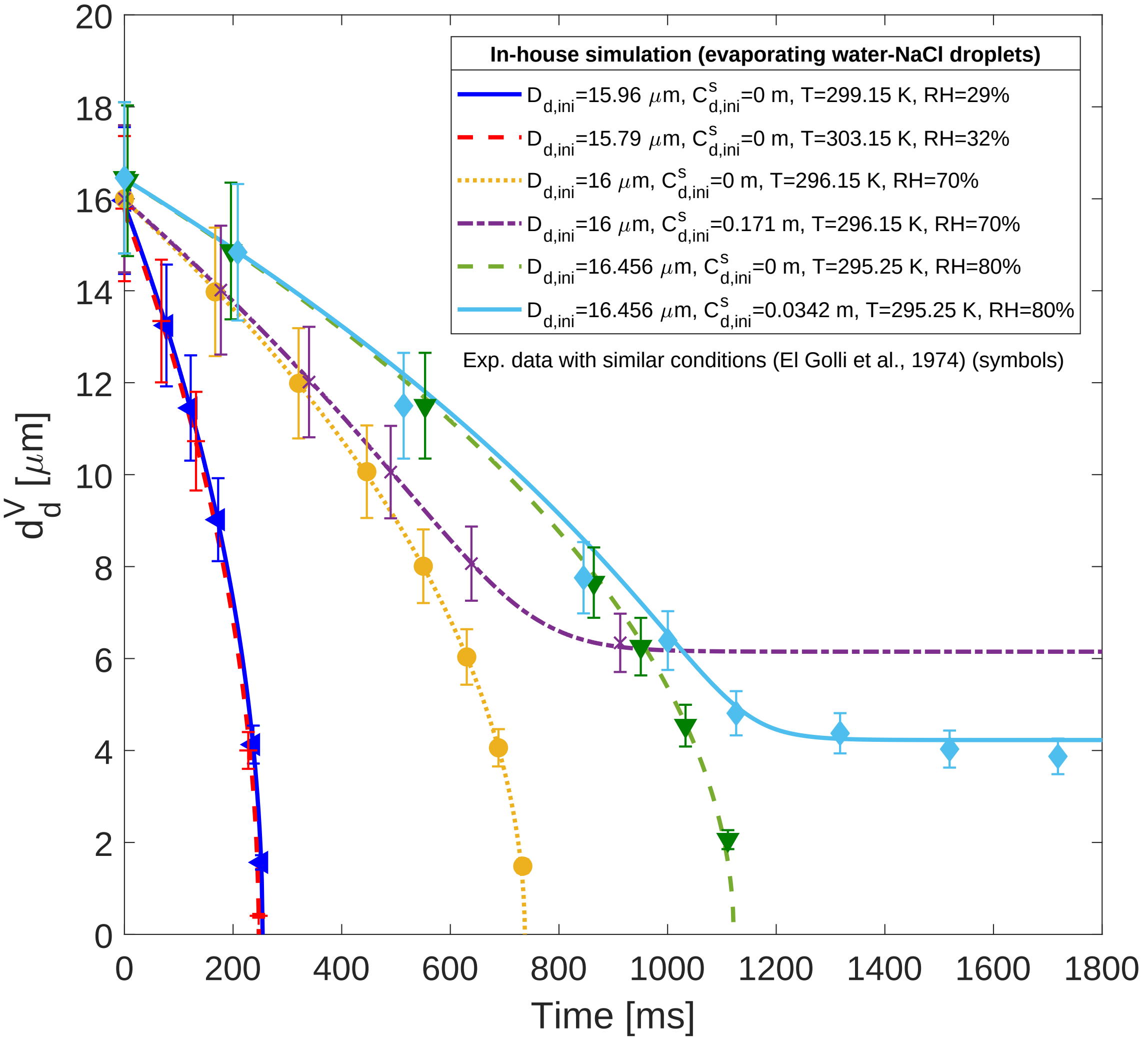

Figure 2.6: Droplet dynamic validation at different molality (m), RH, and T (El Golli et al., 1977).

For the droplet condensation, the in-house simulation is compared with the experimental data by Li et al. (1992). A concurrent airflow stream and the dry NaCl particle injection in the direction parallel to the gravity was considered for the CFPD model. Based on the experimental setup, the particle injection happens through a nozzle located at the upper part of the cylindrical duct (Li et al., 1992) bt the detailed measurement is not provided. As a result, the nozzle is located at the duct inlet for the CFPD model. Figure 2.7 shows the comparison of the particle growth rate versus the initial diameter of the injected droplets into the domain with different airflow RH and temperature. A small increase in RH (from 99% to 99.5%) resulted in a substantial increase in the particle growth. The conversion stage of a dry particle to a supersaturated aqueous droplet can be observed in the CFPD model visualization. The condensation happens in a faster manner compared to the evaporation process because the partial pressure gradient between the dry particle exposed to an airstream with close to saturation condition is significantly higher compared to an aqueous droplet exposed to an airstream with RH=70%.

2.5.2 HCD Model

Figure 2.8 (a) shows the predicted HCD for the target and refractory cells. The validation of the HCD model was performed by comparing the viral titer of the IAV H1N1 infection by Fritz et al. (1999); Hayden et al. (1998) and the average IAV H3N2 viral titer data provided by Hayden et al. (1996) (Figure 2.8 (b)). Also, the IFN data by Fritz et al. (1999) was used for the validation of the interferon profile (Figure 2.8 (c)). Figure 2.8 (b) shows the viral titer data for $TCID_{50}$/ml of nasal wash. One $TCID_{50}$ corresponds to a single infectious virion (Handel et al., 2007). However, more than one virion is needed for infection distribution. As a result the initial value of the virus titer is considered as 5 (Lee et al., 2009) (see Table 2.5).

2.6 Results and Discussion

2.6.1 Airflow Velocity Field

In this study, the momentum transfer is neglected between the DP and continuous phase due to the small diameter of the sneezing event droplets, i.e., the occupying volume fraction. As a result, a one-way coupled scheme holds for the momentum balance,

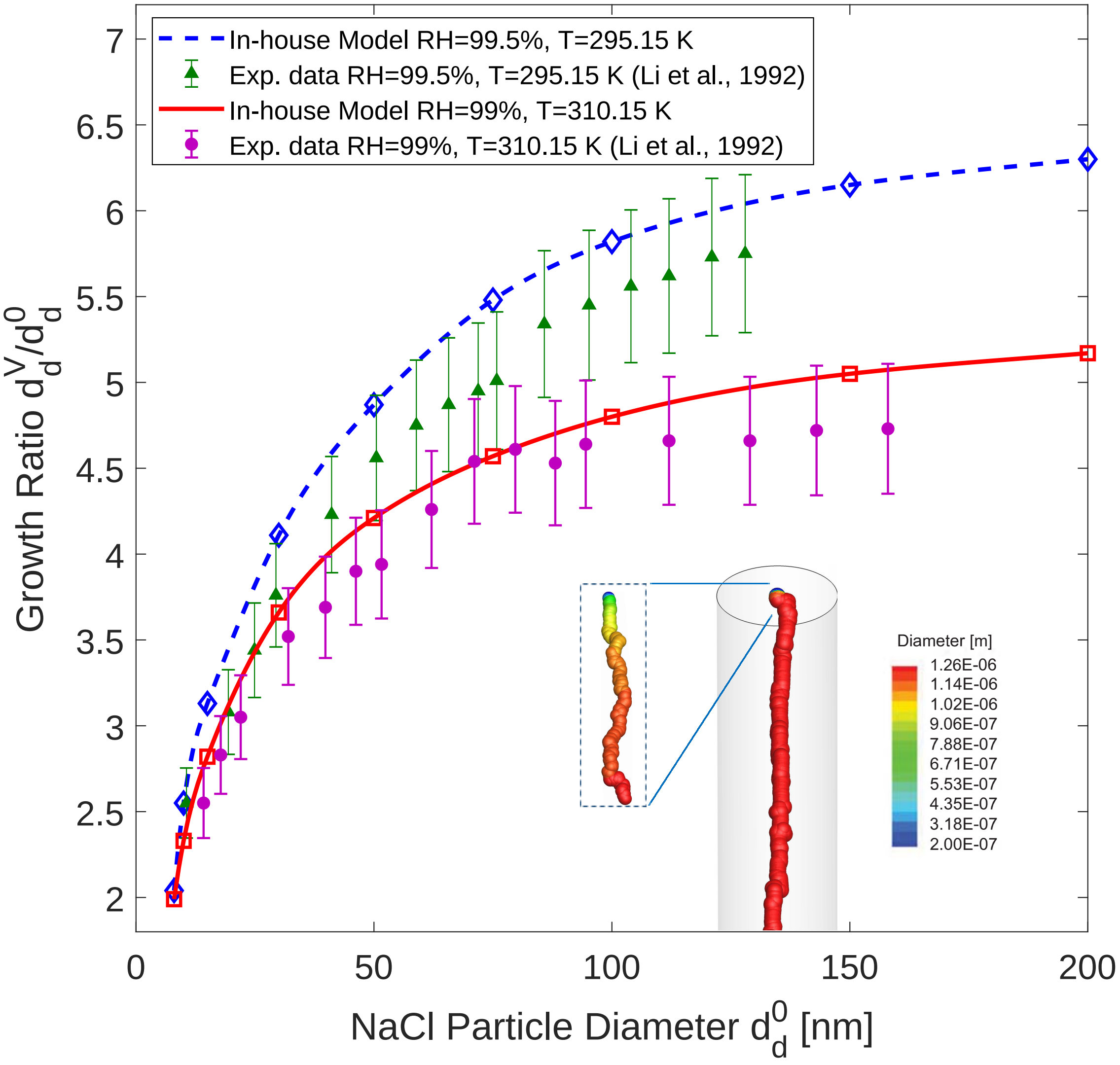

Figure 2.7: The validation of dry NaCl particles hygroscopic growth at different RH and T. The CFPD model setup is provided for the dry NaCl particle with initial diameter d_d^0=200 nm released to the domain with RH=99.5% and T=295.15 K.

Table 2.5: The HCD model initial values and the definition of the simulated variables.

Variable	Definition	Initial Value [unit]
$\underline{T_T}$	Uninfected epithelial cells	4E+8† [cells]
$\underline{R}$	Epithelial cells in the refractory state	0‡ [cells]
$\underline{I}$	Infected epithelial cells	0† [cells]
$\underline{V}$	Virus titer	Regional Deposition form the CFPD model 5 [TCID$_{50}$ ml^{-1}]
$\underline{D_M}$	Mature Dendritic cells	1E+3§ [cells]
$\underline{T_H}$	Effector CD4^{+} T cells	0§ [cells]
$\underline{T_C}$	Effector CD8^{+} T cells	0§ [cells]
$\underline{B}$	Activated B cells	0§ [cells]
$\underline{A}$	Antiviral antibody titer	110.2§ [titers]
$\underline{F}$	Interferon	10* [IFN fold change]

† Handel et al. (2007)
‡ Pawelek et al. (2012)
§ Lee et al. (2009)
∗ Fritz et al. (1999)

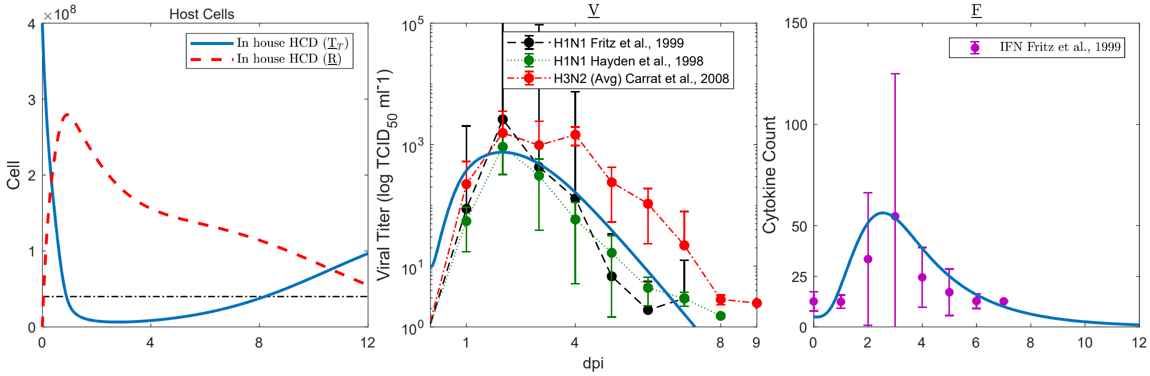

Figure 2.8: The HCD model: (a) the predicted profile for the targeted cell, infected cell, and refractory cell, (b) comparison and validation with mean viral titer [TCID$_{50}$ml^{-1}], and (c) comparision with IFN data provided by Fritz et al. (1999), Hayden et al. (1998), and Hayden et al. (1996).

i.e., the DP was influenced by the airflow but not vice versa. However, the two-way coupled scheme stands for species mass transfer and energy transfer between humid air and droplets. Figures 2.9 and 2.10 show the volume rendering of the normalized velocity magnitude ($\left\|\vec{V}\right\|$) field and $\left\|\vec{V}\right\|$ contours at the specified cross-sections. For the MB, the normalization is based on $\left\|\vec{V}_{max}\right\|$=14.5 m/s generated at t=0.56 s on the onset of the epiglottis and the laryngeal jet core. The NB normalizations were calculated by having $\left\|\vec{V}_{max}\right\|$=23.5 m/s at the time of peak exhalation velocity profile (t=2.35 s) at the inferior nasal aperture both in the left and right nasal passages.

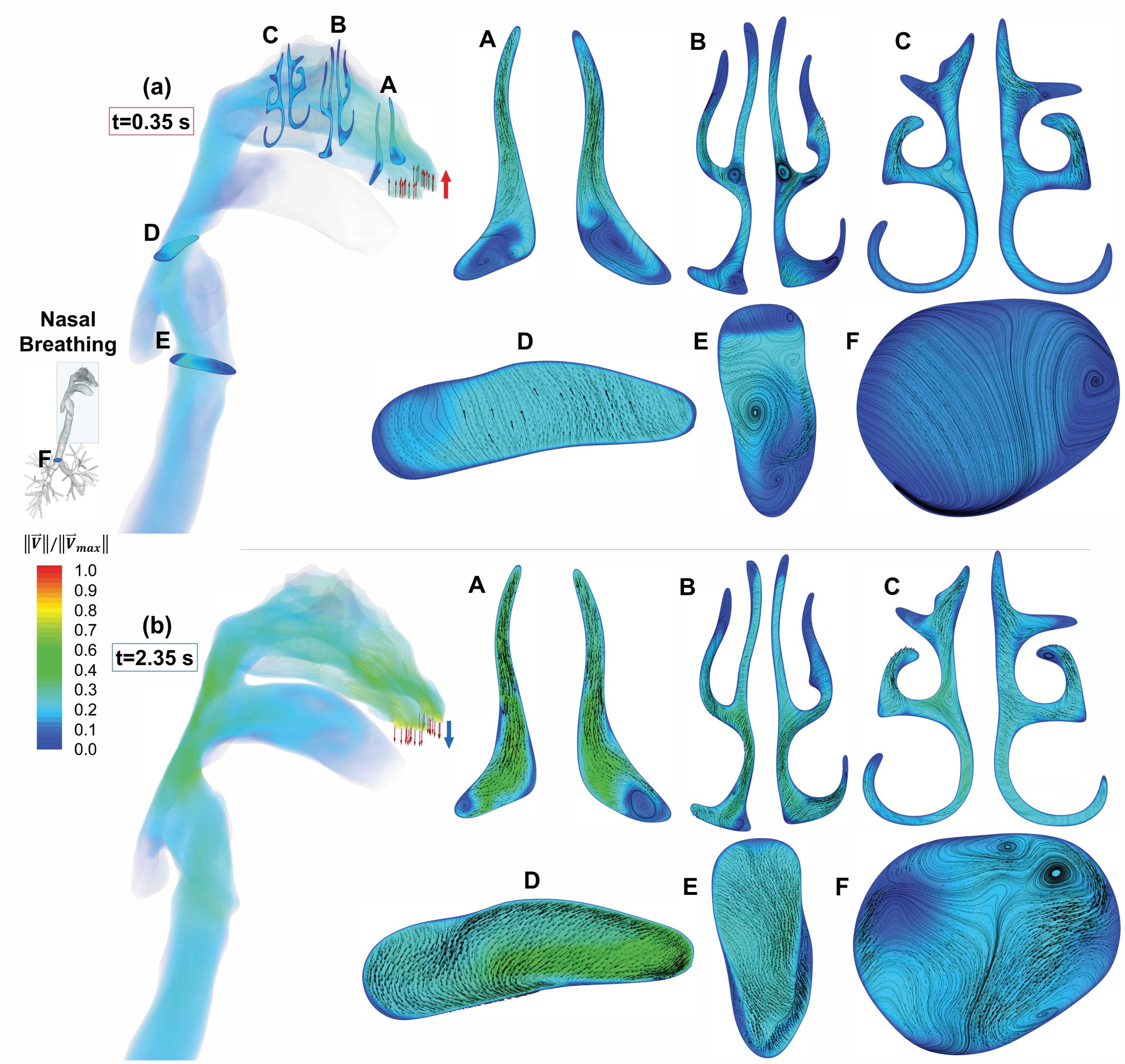

Figure 2.9: Local airflow velocity profile and the volume rendering of the velocity field in a subject-specific upper airway during the nasal breathing at t=0.35 s (peak inhalation velocity) and t=2.35 s (peak exhalation velocity).

For the NB case, the mainstream $\left\|\vec{V}\right\|$ distributions are visualized at six cross-sections and the secondary flows are shown by in-plane streamlines and tangential vectors (see Figure 2.9). The upper row shows the results at the peak velocity during the inhalation period (t=0.35 s), and the lower row shows the results at the peak exhalation period (t=2.35 s). The nasal inlet jet is hitting the superior conchae and the lower pressure induced next to the inferior conchae resulted in the flow disruption and clockwise (CW) vortices were visible at cross-section A (Figure 2.9 (a)-A). At t=0.35 s the Reynolds number (Re) at right nostril is 3,695 and recirculations are formed at the cavity between the inferior turbinate and the nasal septum. Moving forward in the nasal passages, the middle turbinate appears which changed L-shaped passage (see Figure 11 (a)-A) to Y-shaped (see Figure 11 (a)-B) spacing. The flow was separated into three fissures. The pressure drop at the cavity next to the bifurcating point of the Y-shaped opening caused the recirculations to form, i.e., CW in the left passage and counter-clockwise (CCW) in the right passage (Figure 2.9 (a)-B). Towards the posterior nasal apertures, the two passages deform to ξ-shaped passage when superior turbinate appears and the recirculation intensities were dissipated (Figure 2.9 (a)-C). These two passages merge into the nasopharynx. The velocity vectors showed the backward direction as the merged flow from the nasal cavity hits the posterior wall of the oropharynx (Figure 2.9 (a)-D). The same patterns exist until the mainstream airflow entered the trachea. At the glottis, due to the pressure drop at the dead volumes of the laryngopharynx (piriform recesses) a CCW recirculation region is formed (Figure 2.9 (a)-E), being accompanied by the laryngeal jet. Trachea, i.e., a straight cylindrical duct protected with cartridges, helped the flow to retain its laminar profile as Re changes from 2628 at the glottis to 1,760 at the beginning of the primary bifurcation (Figure 2.9 (a)-D and F).

At the peak of nasal exhalation, the flow develops from airstream discharges from the lung and Re is 3,871 at cross-section F (Figure 2.9 (b)-F). As a result, incipient turbulence is expectable. The vortices formed, and the flow deviated to the anterior wall of the trachea (Figure 2.9 (b)-F). As the expiratory flow reached the glottis, the turbulence intensity is reduced and Re is 3,520. In the nasopharynx, the stream separated into two parts by uvula and headed toward the nasal and oral cavity. As the mouth is closed, static pressure differences near the lips provide resistance to the airflow entered the oral cavity, leading to the recirculating flow patterns shown by the volume rendering graph at t=2.35 s. Following the flow in the nasal cavity, the superior section of the nasopharynx, i.e., where the pharyngeal tonsil is located, directed the airflow into the nasal passages. Figure 2.9 (b)-C demonstrated the stream deviated to the inferior meatuses, unlike the airflow patterns observed during the inhalation when the air stream the superior meatuses. The different airflow patterns between nasal inhalation and exhalation significantly influence the IAV-laden droplet transport and deposition in the breathing cycle (Figure 2.9).

Figure 2.10 represents the velocity field at the time stations with the peak inhalation and exhalation flow rates, of the MB profile, i.e., t=0.56 s and t=2.48 s. The uniform velocity inlet was adapted at the mouth during the peak of mouth inhalation that forms a flow with Re=2,450. Because of the relatively low position of the mouth opening, the high-velocity core of the airflow stream stays concentrated near the lower palate, i.e., the space above the tongue. At t=0.56 s, due to low static pressure near the central part of the lower palate induced by the high-velocity airflow, two counter-rotating vertices appear near the upper palate representing the secondary flow patterns at cross-section A (Figure 2.10 (a)-A). Transiting to cross-section B near the 90-degree bend between the oral cavity and pharynx, the triangular lower wall was deformed to a symmetrical geometry with a flat lower wall (Figure 2.10 (a)-B). As a result, the recirculation on the left side of cross-section B was pushed upward leading to the shift of the vortex core on the right side further from the centerline. This flow field created a CW airflow movement in the oropharynx and the flow has

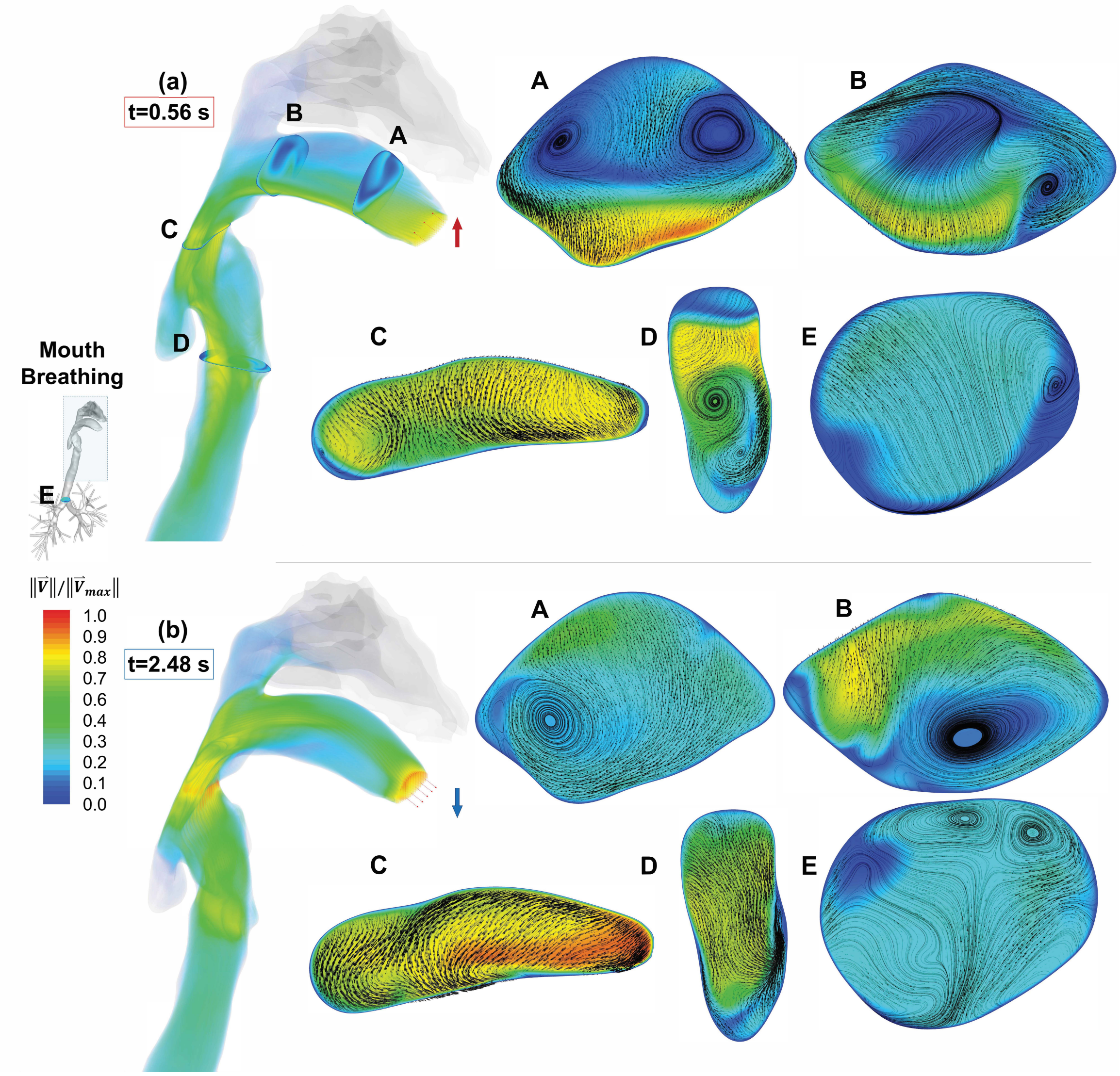

Figure 2.10: Local airflow velocity profile and the volume rendering of the velocity field in a subject-specific upper airway during the mouth breathing at t=0.56 s (peak inhalation velocity) and t=2.48 s (peak exhalation velocity).

deviated to the right upper corner of cross-section C. Entering the trachea, the jet impacts the posterior side and the momentum of the jet core is dissipated accordingly.

During the mouth exhalation phase shown in Figure 2.10 at t=2.48 s, the expiratory laryngeal jet touched the larynx and created a maximum velocity at the constriction of the oropharynx (Figure 2.10 (b)-C). A portion of the flow was discharged into the nasal cavity and resisted in the posterior nasal cavity. Such a phenomenon is due to the momentum loss of the airflow which failed to overcome the static pressure resistance in the nasal cavity. In contrast to the fact that the high-velocity airflow is close to the lower palate during the mouth inhalation phase, the portion of airstream that enters the oral cavity during the exhalation phase strikes the upper palate.

Comparisons between NB and MB cases indicate that the nasal passage can significantly reduce the airflow momentum at the post-nasal region. During the NB inhalation, the core of laryngeal jet has lower turbulence strength that results in a weaker impaction of flow to the posterior tracheal wall compared to the MB case. As a result, lower inertial impaction and droplet deposition is expected for the NB case at the trachea. However, there are similarities between the flow pattern at the subglottal regions between the MB and NB. During the inhalation, the flow pattern at mid trachea is similar between the MB and NB (see Figures 2.9 (a)-E and 2.10 (a)-F). During the exhalation, the secondary flow at mid trachea and glottis are similar between NB and MB. This implicates the similarity of the flow pattern at the subglottal airways regardless of the breathing *via* mouth or nose.

2.6.2 Relative Humidity Distributions

The airflow relative humidity (RH) is calculated by having the local temperature, pressure, and mass fraction of the water vapor. Figure 2.11 shows the RH in percentage for both NB (upper row) and MB (lower row) cases. The contours are at the onset of inhalation (t=0.10 s), the peak inhalation velocity profile (t=0.35 s for NB and t=0.56 s for MB), and at the end of inhalation (t=1.60 s for NB and t=0.56 s for MB). The ambient conditions of water vapor were determined based on the standard condition, i.e., T=310.10 K, P=1 bar, and RH=40%. Initial RH in the pulmonary routes is assumed to be constantly equal to 99.5% and the airway walls were considered nearly saturated at which RH=99.5% (Ferron, 1977). Simulation results show that during the inhalation phase of NB, dry ambient air starts to lower the RH in the nasal cavity. Due to the large surface area to passage length in the nose, saturated airway walls compensate the loss of water vapor resulted from the inhalation. Therefore, at the peak inhalation flow rate (t=0.35 s), RH values are still higher than 90% from nasopharynx to the mid trachea. It can also be observed that the RH distributions are consistent with the airflow velocity contour shown in Figure 2.9. Additionally, compared with the velocity field (see Figure 2.9), RH in recirculation regions are relatively higher because of the longer residence time of the trapped dry airs than those in the mainstreams. At the peak inhalation flow rate, RH was constant in the tracheobronchial trees from G1 to G6. Also, because of the reduced convection effect at the end of nasal inhalation (t=1.60 s), RH in the upper airways (shown in Figure 2.11 (a)) recovers to 99.5% due to the water vapor diffusion from the saturated airway walls.

For the MB case, at t=0.10 s, the inhaled dry air stream has already influenced the entire oral cavity. As the flow impacts the tongue, it deviates towards the upper palate. At t=0.56 s, i.e., the peak inhalation flow rate, the influence of dry air on the RH has already extended beyond the mid of trachea. Comparing with the velocity profile shown in Figure 2.10 (a)-A, the recirculation zones created by the two vortices near the mouth front results in higher local RH values. At t=0.56 s, the average RH% of airstream at the cross-sections of oropharynx and glottis were calculated as 54.3% and 61.6%, respectively. At the end of mouth inhalation, at t=1.76 s, RH values in the upper airway did not recover as prompt as the NB case, indicating longer holding

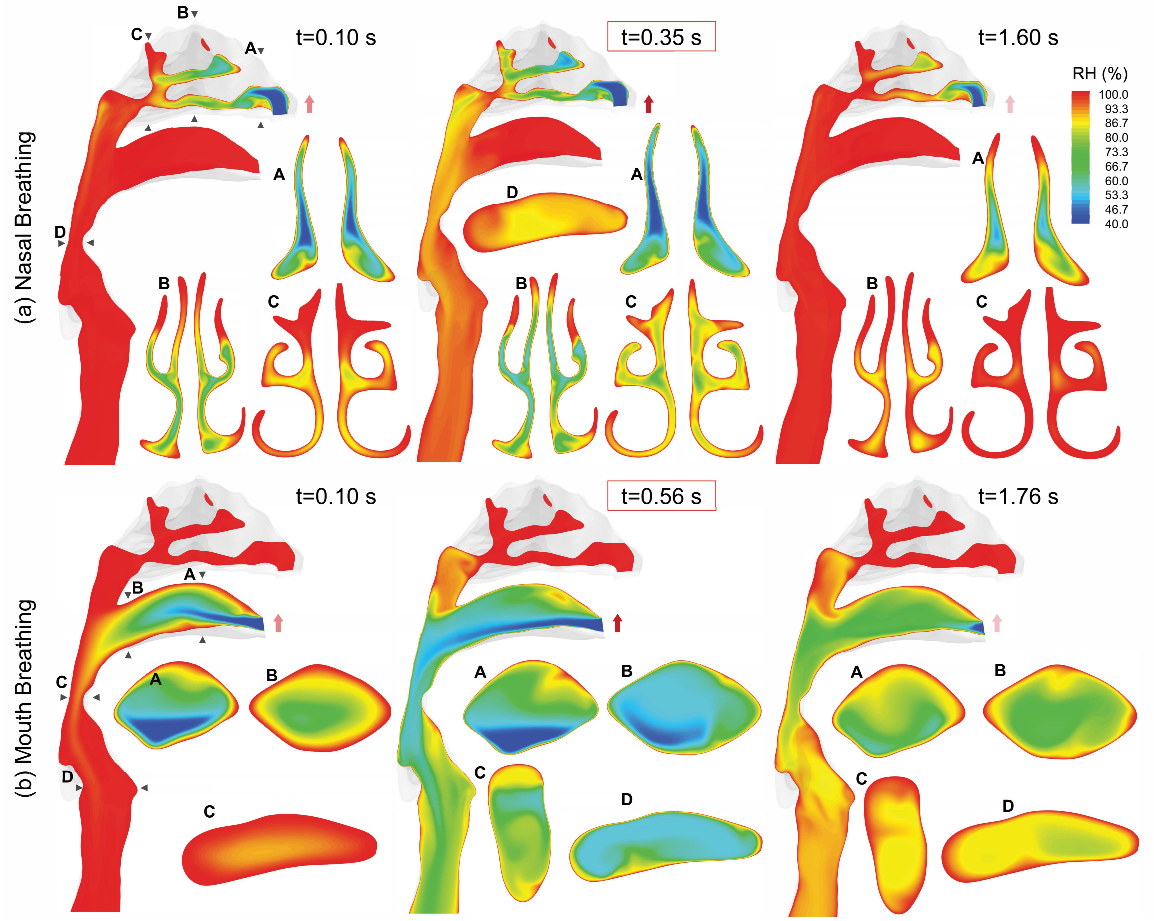

Figure 2.11: Local RH distribution of the respired airflow with RH=40% during nasal breathing and mouth breathing at different times of inhalation period (the walls are set up with RH=99.5%).

time is needed for MB case to have the humid lung environment restored.

Comparisons between NB and MB cases show that the inhaled airflow with lower RH could influence the humidity in pulmonary routes more with MB compared to NB. The high ratio between surface area and passage distance of the nasal cavity provide significant compensation of the humidity and restrict the influence of dry air better than the mouth. Therefore, although the velocity field has a similar pattern at the subglottal regions between NB and MB cases, the transport of the inhaled stream is not identical.

2.6.3 IAV-laden Droplet Size Dynamics and Deposition Pattern

Droplet composition alters the partial pressure gradient and the thermodynamic equilibrium between phases. The airflow velocity, temperature, and water vapor fields determine the balance of heat and mass between phases. Figure 2.12 shows the suspended droplet position at t=1.6 s for NB and t=1.76 s for MB cases, i.e., close to the rest period between the inhalation-exhalation cycle, for pure water droplets, 6.8% NaCl water droplets., and 10.4% NaCl water droplets. In Figure 2.12, droplets are colored based on their diameters and to better compare the droplet size dynamics, only 7 μm droplets are shown. For NB of pure water droplets, it can be observed that droplets were undergoing evaporation. Fast droplet size reduction due to water evaporation happens in the nasal cavity, because of the relatively lower regional RH (see Figure 2.11 (a)). Specifically, RH decreased majorly in the nasal cavity during the inhalation phase of NB, and significant water liquid droplets evaporation occurred in supperglottal regions. In contrast, during MB inhalation of the pure water droplets, RH is much lower in the entire upper airway compared to the NB case, evaporation continues at high rates because of the higher partial pressure differences of water. Specifically, the highest mass exchange occurred in the oropharynx and continued in the trachea. As a result, lower droplet diameters can be observed in the MB case rather than the NB case (see Figures 2.12 (a) and (d)).

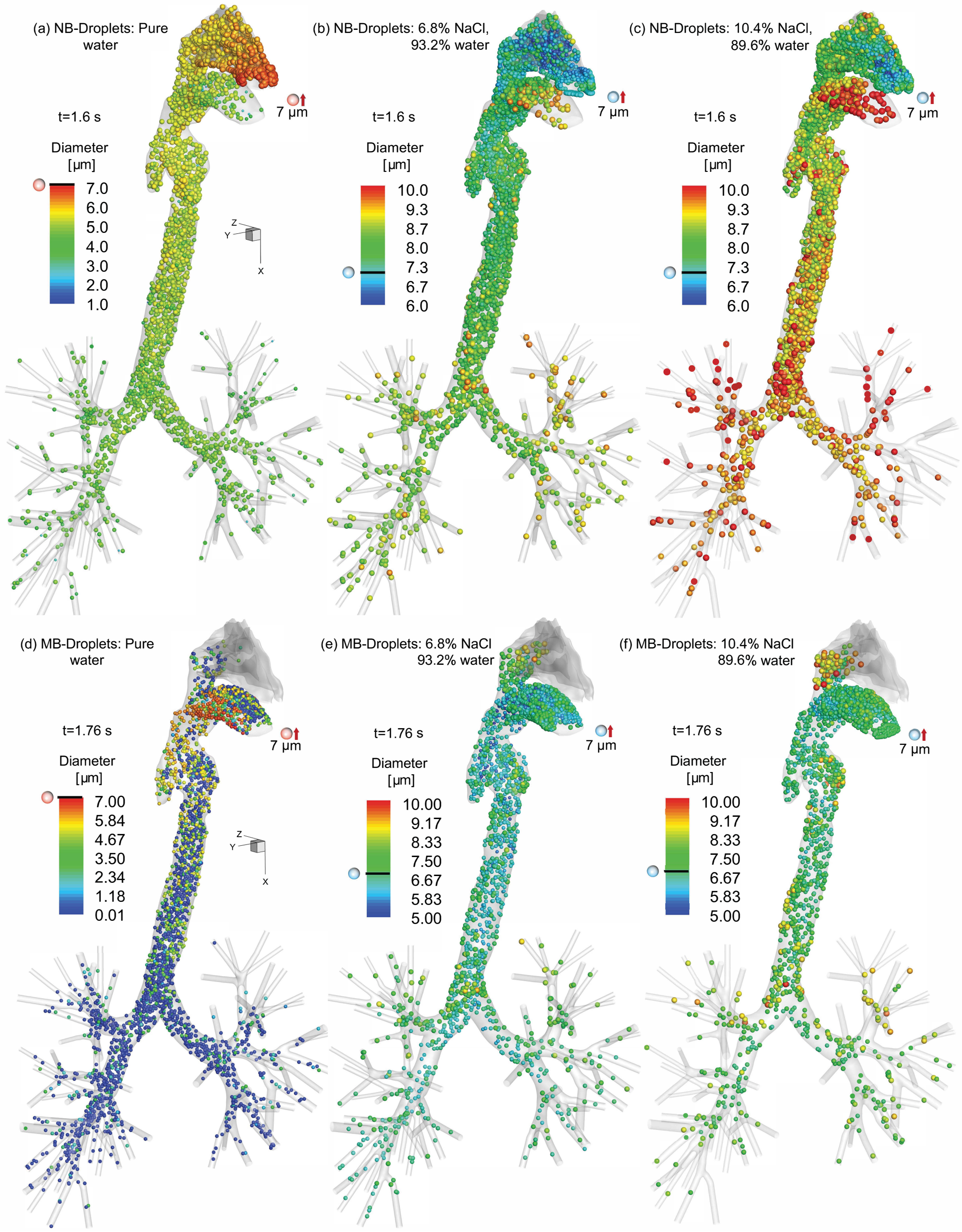

Figure 2.12: The droplet position as it goes under hygroscopic growth or shrinkage during NB and MB, at t=1.60 s (only 7 μm droplets are visualized).

For droplets containing 6.8% NaCl, inhaled by NB (see Figure 2.12 (b)), a decrease in droplet diameter due to the evaporation was observed near the nostrils as the inlet jet increases the droplets Reynolds number and consequently the heat and mass transfer due to the higher Sh and Nu, respectively. Also, lower RH of the inlet flow resulted in an elevated mass exchange between the droplets and the surrounding gas mixture. As droplets transport into the regions with higher RH, ambient water vapor condensate and droplet size increases.

During the inhalation (see Figure 2.12 (b)), some droplets entered and stayed in the nasal cavity with a higher diameter than other droplets. Since droplets suspending in the domain has the same residence time, i.e., 1.6 s, such differences in size growth is due to the higher condensation mass rate induced by higher local RH in the oral cavity (RH=99.5%). A similar trend could be observed for the MB 6.8% NaCl containing droplets (see Figure 2.12 (e)). However, due to the lower RH field, the partial pressure gradient as the driving force of the condensation was not as strong as the NB case. Therefore, the average droplet diameter is lower compared to the NB case. A similar observation is visible for the 10.4% NaCl containing droplets compared to those with 6.8% NaCl. However, because the higher NaCl containing droplets can absorb more water to reach the saturation concentration, the higher size growth happens for droplets with 10.4% NaCl compared to those with 6.8% NaCl content (compare Figures 2.12 (b) and (c) for the NB case and Figures 2.12 (e) and (f) for the MB case).

Deposition patterns of droplets during the inhalation phase and the exhalation phase for four cases of MB and NB with droplets containing pure water or 10.4% NaCl are separately visualized in Figure 2.13. The droplets are colored based on the final diameter at deposition sites. During MB of the pure water droplets, the 20-80 μm droplets deposit mainly at the back of the oral cavity and oropharynx due to dominant inertial impaction effect. Additionally, dispersed deposition patterns of nanoscale droplets can be found in the oral cavity due to the dominant influence of Brownian motion and secondary flow. Moreover, the oral cavity is the main deposition site for droplets with smaller initial size. Indeed, small droplets that did not deposit in the oral cavity will evaporate continuously and change entirely to the vapor phase. Deposition patterns of droplets also show a gradual decrease in the droplet diameters from the pharynx to lower airways due to the continuous evaporations of water liquid. During the expiration, the droplets lost more masses and nanoscale droplet deposit in the oral cavity. Similarly, during NB of pure water droplets, the impaction of large droplets happened at the superior conchae right at the top of nares and due to the narrower passage at the nasal cavity. Deposition includes droplets with all sizes. As a result of high filtration efficiency of the nasal cavity, only the smaller droplets were transferred to the pharynx and distal sections. On the contrary, for droplets with 10.4% NaCl, the deposition patterns show a more uniform size of deposited droplets.

The hygroscopic growth and shrinkage of droplets is a key mechanism that can influence the droplet trajectory and deposition locations (Feng et al., 2016). To investigate such effect on deposition patterns, the regional and total droplet deposition fractions (DF) (Haghnegahdar et al., 2018) are provided in Figure 2.14, with 6 different cases (also see Section 2.2 for case details). NB cases show higher DF in the nasal cavity compared to MB cases, indicating the better filtration efficiency of nose compared to mouth. Furthermore, the better filtration performance of nose prohibits IAV-droplet entering the pharynx, which can be demonstrated by the lower DF in pharynx compared to MB cases. In addition, the total DF of NB was slightly higher compared to MB due to an increased deposition of small droplets when they pass the narrow nasal passages. DF comparisons for droplets with different NaCl composition, i.e., 0.0%, 6.8%, and 10.4%, showed an increase in the total deposition with the increase in NaCl concentration. Due to the higher initial NaCl concentration in droplets, higher water vapor absorption and higher droplet growth are expected. Hence, the deposition would increase in the upper airways. However, for pure water droplets, the DF at the primary region of contact, i.e., the oral cavity for MB and nasal cavity for NB, was higher compared to higher NaCl concentration droplets.

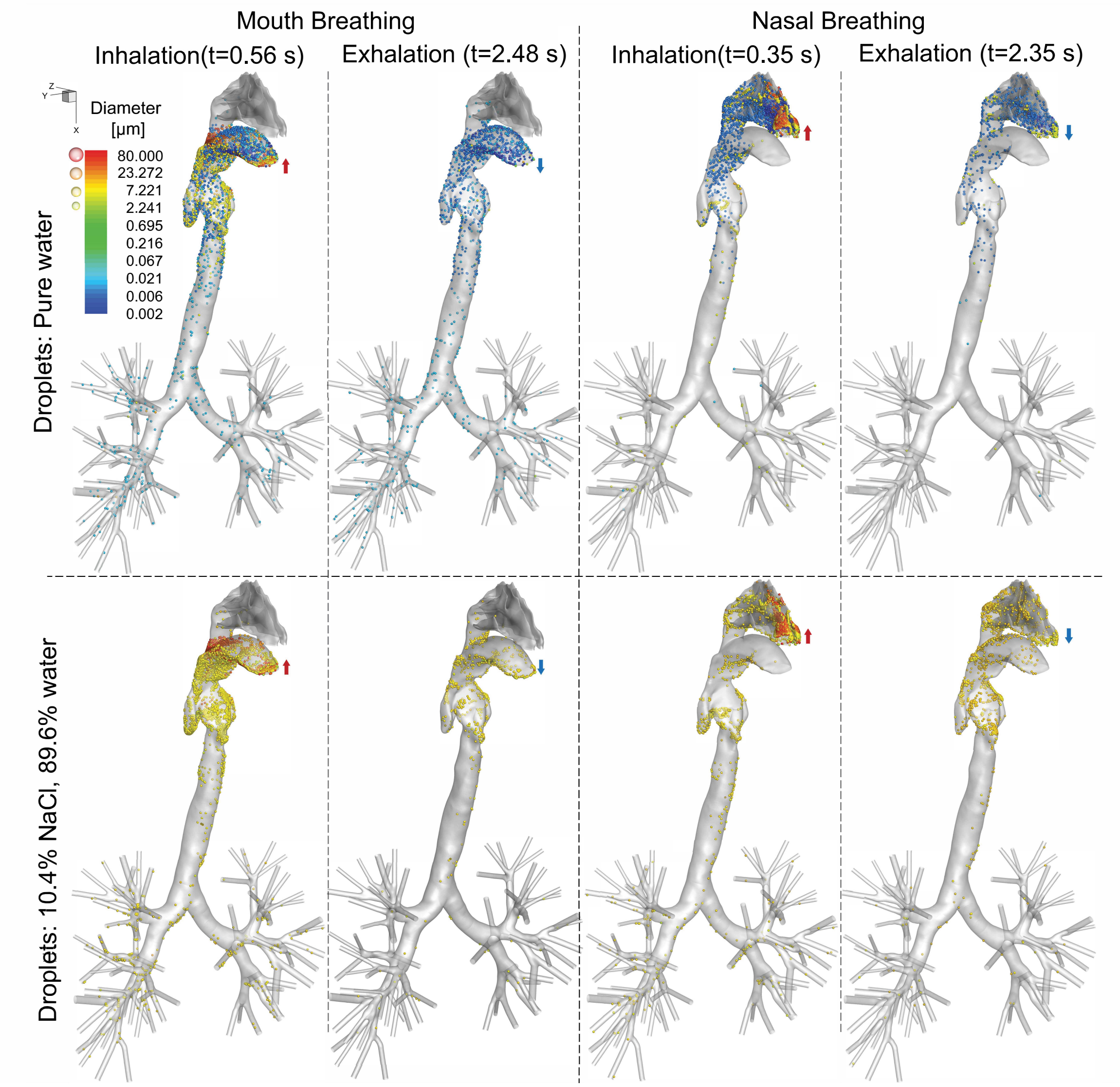

Figure 2.13: The deposition pattern of the pure water and isotonic aqueous droplets (Y_{NaCl}=10.4%) with polydispersed inlet injection during NB and MB.

This pattern was due to the flow fluctuation and droplet dynamics at the beginning of the mouth and nasal passages. As the droplet with NaCl content entered the cavities, first it evaporates, i.e., because of the inlet jet lower RH and increased droplet Reynolds number, and then gradually grow as it moves in the airways. This locally lower droplet size resulted in lower deposition compared to the case with zero NaCl composition, i.e., progressively losing mass and at the upper airway and not only at the mouth opening or nares. Also, comparing the cases with different NaCl content showed a lower locally vaporization of droplets with higher NaCl mass fraction at the beginning of the mouth or nasal cavities which is acceptable as the lower water content for the droplets with 10.4% NaCl results in faster vaporization.

Specifically, the statistical regional and total DF comparisons show that for MB cases, with a 53% increase in the NaCl content (from 6.8% to 10.4% NaCl), the total deposition increases by 6.72%. The pharynx DF increases by 8.85% and the oral cavity DF increases by 2.22%. However, comparisons between the 6.8% NaCl containing droplets and pure water droplets show that the increase in NaCl composition leads to an increase of the total DF by 2.2% and the increase of the pharyngeal DF by 26.54%. Also, it results in a 10.6% decrease of the regional DF in the oral cavity.

Similarly for NB cases, with a 53% increase in the NaCl content (from 6.8% to 10.4% NaCl), the total deposition increases by 6.89%. The pharynx DF increases by 14.3% and the nasal cavity DF increases by 5.22%. However, comparisons between the 6.8% NaCl containing droplets and pure water droplets show that the increase in NaCl composition leads to an increase of the total DF by 1.4% and the increase of the pharyngeal DF by 39.74%. Also, it results in a 5.95% decrease of the nasal cavity DF.

Average diameters of the deposited droplets in the MB cases are lower than NB cases. There are a few possible reasons: (1) The nasal cavity trapped larger droplets more efficiently than the oral cavity; (2) the relatively lower RH in upper airways

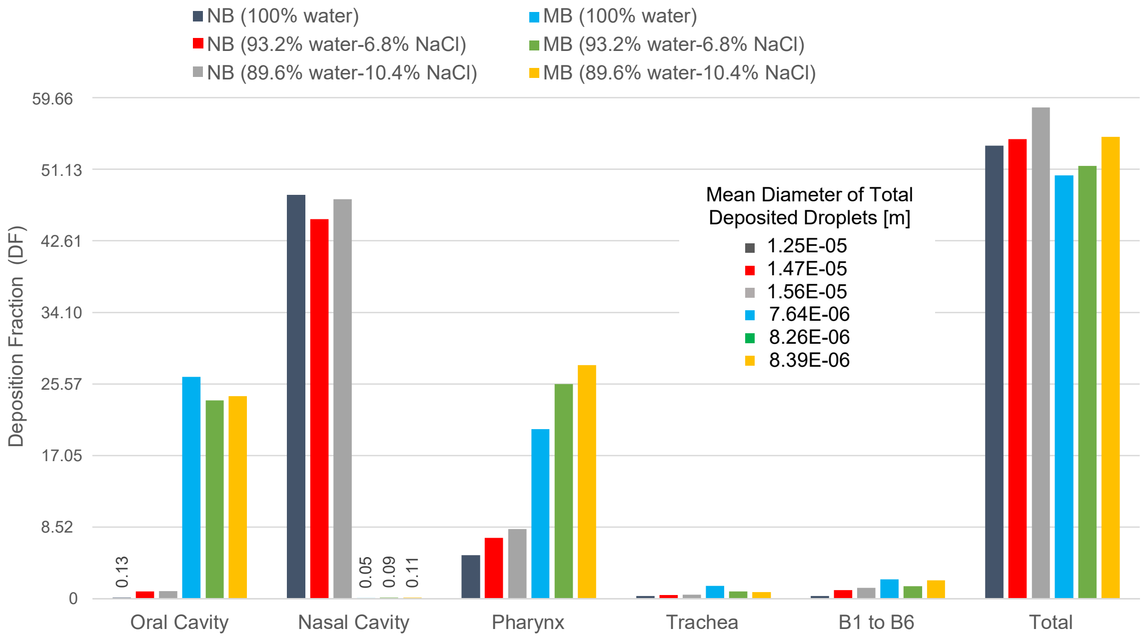

Figure 2.14: The average diameter of deposited droplets and histogram of the deposition fraction (DF).

of MB cases restrict the condensation rate while enhance the evaporation rate. In contrast, due to the lower size of droplets, the number of escaped droplets to the distal sections of the lung was higher for mouth breathers, which result in higher IAV-laden droplets to enter and infect lower airways. It worths mentioning that during the evaporation process, the NaCl concentration in droplets increases. This higher level of salt would be toxic to the IAV agents (Yang and Marr, 2012). In this study, this effect is neglected as the evaporation is majorly happened for the pure water containing droplets and the local vaporization of NaCl containing droplets at the inlets was not significant (see Figures 2.12 and 2.13).

2.6.4 Within-Host Dynamics of IAV

The conjunction of the IAV-laden CFPD and post-deposition HCD provides in-demand healthcare information. The local within-host cell dynamics and the virus replication help to determine the local infection site and the immune system response in the respiratory system. The deposition of the IAV-laden droplets shows the population of active virus agents at regional sites in upper airways. Exposure to a sneezing event with a distance of 3 feet prompted an acute infection for IAV (Knight, 1980). However, previous studies neglect the inhalation routes by the recipient to airborne sneezing IAV droplets. Figure 2.15 shows the host cells ($\underline{T}_T$ and $\underline{R}$) dynamics and 50% human infectious dose [HID_{50}] in the unit of $TCID_{50}$ per secretion volume, and produced IFN ($\underline{F}$). A period of 12 dpi was simulated using the HCD model, during the NB at the nasal cavity (NC) and pharynx (PY), and during the MB at the oral cavity (OC) and pharynx (PY). The local threshold of clinical symptoms was determined as the time once 10% of the epithelium are desquamated (Bocharov and Romanyukha, 1994) until $\underline{I}$ has reached 5% of its lowest population.

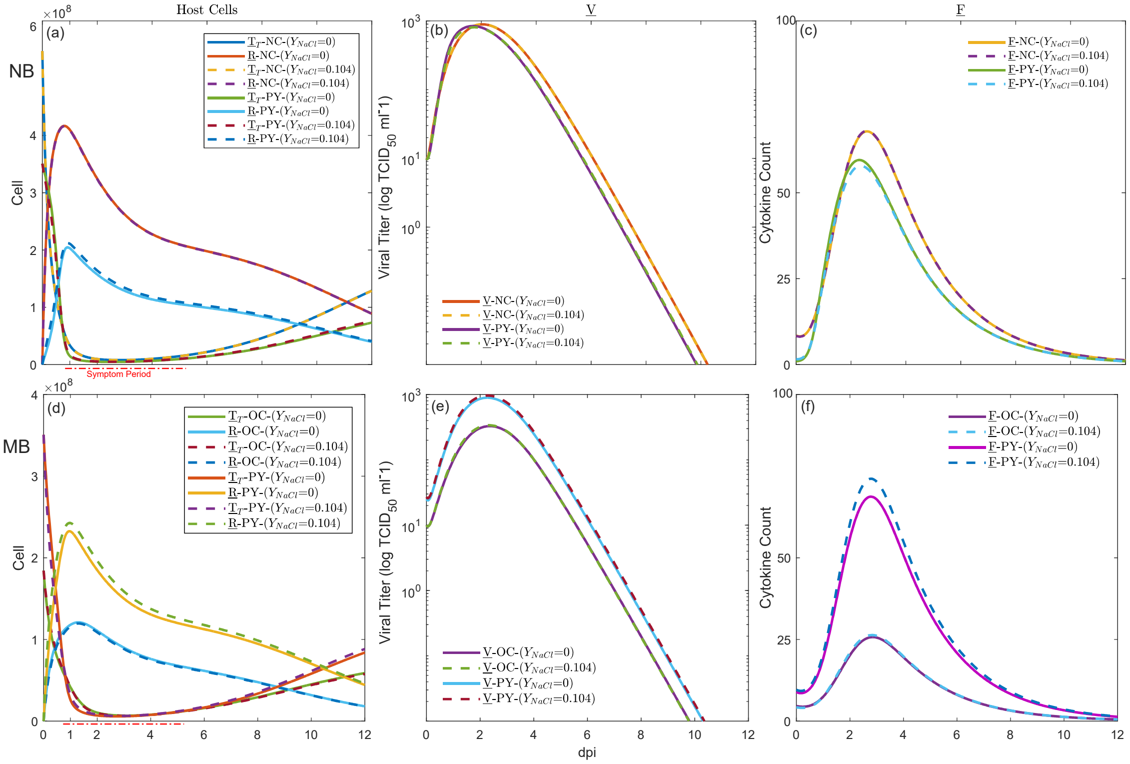

Figure 2.15: The regional HCD estimation and virus titer using the multiscale model: (a-c) HCD during NB at the nasal cavity (NC) and pharynx (PY) for droplets with different salt content (Y_{NaCl}=0 and Y_{NaCl}=0.104), (d-f) HCD during MB at oral cavity (OC) and PY for droplets with different salt content (Y_{NaCl}=0 and Y_{NaCl}=0.104).

During the NB, the highest DFs are in NC and PY regardless of the droplet composition. The numbers of virus-laden droplets deposited at the NC were close for cases with $Y_{NaCl} = 0$ and $Y_{NaCl} = 0.104$, but at the PY droplets with $Y_{NaCl} = 0.104$ had 38% higher DF compared to those with $Y_{NaCl} = 0$. Higher DF induced a higher viral load to the local epithelium, but the difference is negligible as the number of viral particulates representing one TCID_{50} determines the connection between the CFPD and HCD models. The local HCD of NC and PY show that the higher DF and epithelial cells at NC contributes to 2 times higher conversion of susceptible cells to refractory state (Figure 2.15 (a)). More IFNs were released at NC with 1.14 times higher amount with longer duration (0.35 days) compared to PY (Figure 2.15 (c)). However, the $\underline{T}_T$ profile shows a similar minimum value between PY and NC because the higher surface area at the NC contributes to a higher population of immune system agents and the infection was prevented from causing severe damage to the tissue layers (Figure 2.15 (b)). Also, the virus titer shows comparable infection severity at PY and NC during NB. As IIS and AIS removed the virus progenies, the cells were shifting back to the susceptible state, and the total apoptosis of epithelium at 12 dpi are 76.4% and 78.7% of the initial cell population at NC and PY respectively (see Figure 2.15 (a)). The regional respiratory symptom threshold was determined at 0.91 to 5.24 dpi and 0.85 to 5.26 dpi at NC and PY, respectively. The systemic symptom was predicted with 1-day delay compared to respiratory symptoms based on symptom score data provided by Knight (1980); Carrat et al. (2008). As a result, the systemic symptom threshold at NC was between 1.91 to 6.24 dpi and similarly 1.85 to 6.26 dpi at PY during NB. The duration of symptom at the PY is longer than NC as the AIS and IIS combated the pathogens with higher availability in NC (higher ratio between passage surface area and passage length).

Once the IAVs are inhaled *via* MB, the highest DFs are in OC and PY. Similar to NB cases, the difference in droplet composition does not impose a significant change on the local viral load. The comparison of local HCD in OC and PY show a higher epithelial cell population in PY but similar DFs. The maximum population of the refractory cell is 1.87 times higher and IFN cytokine release is 2.01 times more at PY compared to OC (see Figures 2.15 (d) and (e)). The duration of IFN release was similar due to the similarity between the surface area at PY and OC. An identical $\underline{T}_T$ minimum value between PY and NC due to similarity on the viral load and consequently immune systems agents response (Figure 2.15 (d)). The virus titer showed a similar trend but slightly higher peak infection titer at PY compared to OC due to the 15.3% higher DF of virus-laden droplets with $Y_{NaCl} = 0.104$ at PY, showing elevated infection at PY and OC during MB. By increasing the IIS and AIS agents populations, the refractory cells shifted back to the susceptible state, and the total apoptosis of epithelium at 12 dpi was predicted as 74.7% and 68.6% of the initial cell population at PY and OC respectively (see Figure 2.15 (d)). The local respiratory symptom threshold was determined at 0.62 to 5.44 dpi and 0.66 to 5.56 dpi at the posterior of OC and PY, respectively. The threshold of the systemic symptom at the posterior OC was predicted from 1.62 to 6.44 dpi and similarly for PY from 1.66 to 6.26 dpi at PY during NB.

The IAV-laden droplet respiration through MB and NB lead to different deposition patterns and distinctive infection patterns in the short-term dpi. In this study, the mucus clearance in OC and NC were neglected. In both cases, the virus titer decreases to lower below the value at 5.6 dpi which represents an increased level of relief for flu symptoms (see Figures 2.15 (b) and (e)). Comparatively, infections in PY induced by the inhaled IAV-laden droplets *via* NB and MB show higher infection titers. The clinical symptom was predicted to appear in the OC faster than NC due to the lower surface area and hence, lower immune system agents population. It also indicates a more extended recovery period. As demonstrated by the present *in-silico* study, low strain (H1N1 and H3N2) IAV replication happened in the upper airway tissues which agreed with experiments. Therefore, higher accumulation of activated dendritic cells as representative of adaptive immune system activation can be identified in PY regions.

2.7 Conclusions

A multiscale *in silico* epidemiological study was performed to evaluate the transportation, deposition, and local replication of the low-strain IAV in a subject-specific human respiratory system. Two routes of exposure through oral and nasal breathings with realistic respiratory waveforms were incorporated. The hygroscopic growth and shrinkage of droplets with different NaCl content were estimated using the CFPD model. The proposed model showed the feasibility of an experimentally validated multiscale CFPD-HCD model in predicting the local virus replication and population variations of the relative tissue agents. The quantitative conclusions are as follows:

- As demonstrated by the present *in-silico* study, low-strain (H1N1 and H3N2) IAV replication occurs at the upper airway tissues which are in agreement with experiments.

- For the mouth breathing case, the droplet deposition fraction in the oral cavity was 26.4%, 23.7%, and 24.1% respectively for droplets with NaCl mass fraction of 0, 0.068, and 0.104. No monotonic trend of the regional deposition is identified with the NaCl mass fraction increase.

- For the nasal breathing case, the droplet deposition fraction in the nasal cavity was 48.1%, 45.2%, and 47.6% respectively for the droplets with NaCl mass fraction of 0, 0.068, and 0.104.

- As a result of high filtration efficiency of the nasal cavity, only the smaller droplets were transferred to the pharynx and distal sections. Specifically, the pharynx deposition fraction was significantly lower during the mouth breathing (5.22%, 7.21%, and 8.34% respectively for the droplets with NaCl mass fraction of 0, 0.068, and 0.104) compared to the nasal breathing (20.2%, 25.5%, and 27.8% respectively for the droplets with NaCl mass fraction of 0, 0.068, and 0.104).

- Because of the elevated penetration of inhaled airflow rate with lower RH (with RH=40%) for the mouth breathing case, total deposited droplets had a smaller diameter compared to the nasal breathing case.
- Higher accumulation of activated dendritic cells as representative of adaptive immune system activation was identified in the pharynx and oral cavity during the mouth breathing and similarly in the pharynx and nasal cavity during the nasal breathing.
- In the absence of mucus clearance, the average onset of systemic symptom was estimated at 1.88 dpi for the nasal breathing and 1.64 dpi during the mouth breathing exposure conditions. It shows the faster infection distribution and immune system response during the mouth breathing exposure.

2.8 Limitations and Future Work

The biological system can be affected by a vast number of factors that makes the numerical simulation highly complex and challenging. Dobrovolny et al. (2013) have reported that no single model can predict the viral and host response dynamics separately. Hence, more complex 3D cell culture media are required to consider the intercellular communication in the realistic physiology of the tissue. Furthermore, more informative data regarding the host cell and immune system response must be used for the model training by employing the machine learning techniques. Currently, most of the developed HCD models are underfitting the training data as the numbers of the virus titer data are limited. To develop a more conclusive multiscale model, other future research tasks include:

- To consider the subject-specific human airway configurations for individual diseased subjects, e.g., acute bronchitis and COPD patients.

- To employ the glottal adduction motion as it can significantly change the droplet deposition patterns.

- To include the movement of the periciliary fluid layer by ciliary propulsions and in tissue spatial distribution of the cell population, e.g., T cell movement within lymph nodes, through employing the agent-based model.

- To include the resuspension of viral droplets from the wall film of the periciliary fluid layer by employing the shear stress induced friction by the respired air as this resuspension of discrete droplets would elevate the transport of the viral agent in the lungs. The same framework can be employed for the evaluation of HID_{50} in the human expelled breath at different times post-infection.

REFERENCES

Abraham, K., Andres, S., Palavinskas, R., Berg, K., Appel, K. E., and Lampen, A. (2011). Toxicology and risk assessment of acrolein in food. *Molecular nutrition & food research*, 55(9):1277–1290.

Akpinar-Elci, M., Travis, W., Lynch, D., and Kreiss, K. (2004). Bronchiolitis obliterans syndrome in popcorn production plant workers. *European Respiratory Journal*, 24(2):298–302.

Alarcon, R. (1976). Studies on the in vivo formation of acrolein: 3-hydroxypropylmercapturic acid as an index of cyclophosphamide (nsc-26271) activation. *Cancer treatment reports*, 60(4):327–335.

Alfi, M. and Talbot, P. (2013). Health-related effects reported by electronic cigarette users in online forums. *Journal of medical Internet research*, 15(4).

Allen, J. G., Flanigan, S. S., LeBlanc, M., Vallarino, J., MacNaughton, P., Stewart, J. H., and Christiani, D. C. (2015). Flavoring chemicals in e-cigarettes: diacetyl, 2, 3-pentanedione, and acetoin in a sample of 51 products, including fruit-, candy-, and cocktail-flavored e-cigarettes. *Environmental health perspectives*, 124(6):733–739.

Allen, J. G., Flanigan, S. S., LeBlanc, M., Vallarino, J., MacNaughton, P., Stewart, J. H., and Christiani, D. C. (2016). Flavoring chemicals in e-cigarettes: diacetyl, 2, 3-pentanedione, and acetoin in a sample of 51 products, including fruit-, candy-, and cocktail-flavored e-cigarettes. *Environmental health perspectives*, 124(6):733.

Allen, M. D. and Raabe, O. G. (1985). Slip correction measurements of spherical solid aerosol particles in an improved millikan apparatus. *Aerosol Science and Technology*, 4(3):269–286.

Antia, R., Bergstrom, C. T., Pilyugin, S. S., Kaech, S. M., and Ahmed, R. (2003). Models of cd8+ responses: 1. what is the antigen-independent proliferation program. *Journal of theoretical biology*, 221(4):585–598.

ATSDR (2007). Toxicological profile for acrolein. *US Department of Health and Human Services, Public Health Service Atlanta, GA*.

Baccam, P., Beauchemin, C., Macken, C. A., Hayden, F. G., and Perelson, A. S. (2006). Kinetics of influenza a virus infection in humans. *Journal of virology*, 80(15):7590–7599.

Bailey, M., Kreyling, W., Andre, S., Batchelor, A., Collier, C., Drosselmeyer, E., Ferron, G., Foster, P., Haider, B., Hodgson, A., et al. (1989). An interspecies comparison of the lung clearance of inhaled monodisperse cobalt oxide particles—part i: Objectives and summary of results. *Journal of aerosol science*, 20(2):169–188.

Beauchemin, C. A. and Handel, A. (2011). A review of mathematical models of influenza a infections within a host or cell culture: lessons learned and challenges ahead. *BMC public health*, 11(1):S7.

Behar, R. Z. and Talbot, P. (2015). Puffing topography and nicotine intake of electronic cigarette users. *PloS one*, 10(2):e0117222.

Belka, M., Lizal, F., Jedelsky, J., Jicha, M., and Pospisil, J. (2017). Measurement of an electronic cigarette aerosol size distribution during a puff. In *EPJ Web of Conferences*, volume 143, page 02006. EDP Sciences.

Benowitz, N. L., Jacob, P., Jones, R. T., and Rosenberg, J. (1982). Interindividual variability in the metabolism and cardiovascular effects of nicotine in man. *Journal of Pharmacology and Experimental Therapeutics*, 221(2):368–372.

Blumenkrantz, D. (2014). The cellular and molecular basis of transmission of influenza viruses.

Bocharov, G. and Romanyukha, A. (1994). Mathematical model of antiviral immune response iii. influenza a virus infection. *Journal of Theoretical Biology*, 167(4):323–360.

Boianelli, A., Nguyen, V. K., Ebensen, T., Schulze, K., Wilk, E., Sharma, N., Stegemann-Koniszewski, S., Bruder, D., Toapanta, F. R., Guzmán, C. A., et al. (2015). Modeling influenza virus infection: a roadmap for influenza research. *Viruses*, 7(10):5274–5304.

Bush, M. L., Frederick, C. B., Kimbell, J. S., and Ultman, J. S. (1998). A cfd–pbpk hybrid model for simulating gas and vapor uptake in the rat nose. *Toxicology and applied pharmacology*, 150(1):133–145.

Canini, L. and Carrat, F. (2011). Population modeling of influenza a/h1n1 virus kinetics and symptom dynamics. *Journal of virology*, 85(6):2764–2770.

Carrat, F. and Flahault, A. (2007). Influenza vaccine: the challenge of antigenic drift. *Vaccine*, 25(39):6852–6862.

Carrat, F., Vergu, E., Ferguson, N. M., Lemaitre, M., Cauchemez, S., Leach, S., and Valleron, A.-J. (2008). Time lines of infection and disease in human influenza: a review of volunteer challenge studies. *American journal of epidemiology*, 167(7):775–785.

Chen, X., Feng, Y., Zhong, W., and Kleinstreuer, C. (2017). Numerical investigation of the interaction, transport and deposition of multicomponent droplets in a simple mouth-throat model. *Journal of Aerosol Science*, 105:108–127.

Cheng, Y.-S., Zhou, Y., and Chen, B. T. (1999). Particle deposition in a cast of human oral airways. *Aerosol Science & Technology*, 31(4):286–300.

Cobb, N. K., Byron, M. J., Abrams, D. B., and Shields, P. G. (2010). Novel nicotine delivery systems and public health: the rise of the "e-cigarette".

Conklin, D. J., Malovichko, M. V., Zeller, I., Das, T. P., Krivokhizhina, T. V., Lynch, B. H., Lorkiewicz, P., Agarwal, A., Wickramasinghe, N., Haberzettl, P., et al. (2017). Biomarkers of chronic acrolein inhalation exposure in mice: Implications for tobacco product-induced toxicity. *Toxicological Sciences*.

CORESTA (2014). Routine analytical machine for e-cigarette aerosol generation and collection - definitions and standard conditions. *CORESTA recommended method No. 81*.

Corley, R. A., Kabilan, S., Kuprat, A. P., Carson, J. P., Jacob, R. E., Minard, K. R., Teeguarden, J. G., Timchalk, C., Pipavath, S., Glenny, R., et al. (2015). Comparative risks of aldehyde constituents in cigarette smoke using transient computational fluid dynamics/physiologically based pharmacokinetic models of the rat and human respiratory tracts. *Toxicological Sciences*, 146(1):65–88.

Corley, R. A., Kabilan, S., Kuprat, A. P., Carson, J. P., Minard, K. R., Jacob, R. E., Timchalk, C., Glenny, R., Pipavath, S., Cox, T., et al. (2012). Comparative computational modeling of airflows and vapor dosimetry in the respiratory tracts of rat, monkey, and human. *Toxicological Sciences*, 128(2):500–516.

Cox, N. and Subbarao, K. (2000). Global epidemiology of influenza: past and present. *Annual review of medicine*, 51(1):407–421.

Daly, B. J. and Harlow, F. H. (1970). Transport equations in turbulence. *The Physics of Fluids*, 13(11):2634–2649.

Darquenne, C. (2012). Aerosol deposition in health and disease. *Journal of aerosol medicine and pulmonary drug delivery*, 25(3):140–147.

Dautzenberg, B. and Bricard, D. (2015). Real-time characterization of e-cigarettes use: the 1 million puffs study. *J Addict Res Ther*, 6(2).

Dawkins, L. E., Kimber, C. F., Doig, M., Feyerabend, C., and Corcoran, O. (2016). Self-titration by experienced e-cigarette users: blood nicotine delivery and subjective effects. *Psychopharmacology*, 233(15-16):2933–2941.

De Andrea, M., Ravera, R., Gioia, D., Gariglio, M., and Landolfo, S. (2002). The interferon system: an overview. *European Journal of Paediatric Neurology*, 6:A41–A46.

De Woskin, R., Greenberg, M., Pepelko, W., and Strickland, J. (2003). Toxicological review of acrolein (cas no. 107-02-08) in support of summary information on the integrated risk information system (iris). *Washington, DC: US Environmental Protection Agency*.

Dobrovolny, H. M., Reddy, M. B., Kamal, M. A., Rayner, C. R., and Beauchemin, C. A. (2013). Assessing mathematical models of influenza infections using features of the immune response. *PloS one*, 8(2):e57088.

Drew, D. A. (1976). Two-phase flows: constitutive equations for lift and brownian motion and some basic flows. *Archive for Rational Mechanics and Analysis*, 62(2):149–163.

Dugan, V. G., Blanton, L., Elal, A. I. A., Alabi, N., Barnes, J., Brammer, L., Burns, E., Cummings, C. N., Davis, T., Flannery, B., et al. (2017). Update: Influenza activity-united states, october 1–november 25, 2017. *MMWR. Morbidity and mortality weekly report*, 66(48):1318.

Duguid, J. (1946). The size and the duration of air-carriage of respiratory droplets and droplet-nuclei. *Epidemiology & Infection*, 44(6):471–479.

Eames, I., Tang, J., Li, Y., and Wilson, P. (2009). Airborne transmission of disease in hospitals.

Edgar, T. F., Himmelblau, D. M., and Lasdon, L. S. (2001). *Optimization of chemical processes*. McGraw-Hill,.

Effros, R. M., Hoagland, K. W., Bosbous, M., Castillo, D., Foss, B., Dunning, M., Gare, M., Lin, W., and Sun, F. (2002). Dilution of respiratory solutes in exhaled condensates. *American Journal of Respiratory and Critical Care Medicine*, 165(5):663–669.

El Golli, S., Arnaud, G., Bricard, J., and Treiner, C. (1977). Evaporation of volatile solvent from saline multi-component droplets carried in a stream of air. *Journal of Aerosol Science*, 8(1):39–54.

Farmer, S. (1991). *The airway epithelium: physiology, pathophysiology, and pharmacology*, volume 55. Marcel Dekker.

Farsalinos, K. E., Kistler, K. A., Gillman, G., and Voudris, V. (2014). Evaluation of electronic cigarette liquids and aerosol for the presence of selected inhalation toxins. *Nicotine & Tobacco Research*, 17(2):168–174.

Farsalinos, K. E., Voudris, V., and Poulas, K. (2015). E-cigarettes generate high levels of aldehydes only in 'dry puff'conditions. *Addiction*, 110(8):1352–1356.

Farsalinos, K. E., Voudris, V., Spyrou, A., and Poulas, K. (2017). E-cigarettes emit very high formaldehyde levels only in conditions that are aversive to users: a replication study under verified realistic use conditions. *Food and Chemical Toxicology*, 109:90–94.

Feng, Y. and Kleinstreuer, C. (2013). Analysis of non-spherical particle transport in complex internal shear flows. *Physics of Fluids*, 25(9):091904.

Feng, Y., Kleinstreuer, C., Castro, N., and Rostami, A. (2016). Computational transport, phase change and deposition analysis of inhaled multicomponent droplet–vapor mixtures in an idealized human upper lung model. *Journal of Aerosol Science*, 96:96–123.

Feng, Y., Zhao, J., Kleinstreuer, C., Wang, Q., Wang, J., Wu, D. H., and Lin, J. (2018). An in silico inter-subject variability study of extra-thoracic morphology effects on inhaled particle transport and deposition. *Journal of Aerosol Science*.

Ferron, G. (1977). The size of soluble aerosol particles as a function of the humidity of the air. application to the human respiratory tract. *Journal of Aerosol Science*, 8(4):251–267.

Fritz, R. S., Hayden, F. G., Calfee, D. P., Cass, L. M., Peng, A. W., Alvord, W. G., Strober, W., and Straus, S. E. (1999). Nasal cytokine and chemokine responses in experimental influenza a virus infection: results of a placebo-controlled trial of intravenous zanamivir treatment. *The Journal of infectious diseases*, 180(3):586–593.

Gloede, E., Cichocki, J. A., Baldino, J. B., and Morris, J. B. (2011). A validated hybrid computational fluid dynamics-physiologically based pharmacokinetic model for respiratory tract vapor absorption in the human and rat and its application to inhalation dosimetry of diacetyl. *Toxicological Sciences*, 123(1):231–246.

Goniewicz, M. L., Gawron, M., Smith, D. M., Peng, M., Jacob, P., and Benowitz, N. L. (2017). Exposure to nicotine and selected toxicants in cigarette smokers who switched to electronic cigarettes: a longitudinal within-subjects observational study. *Nicotine & Tobacco Research*, 19(2):160–167.

Goniewicz, M. L., Hajek, P., and McRobbie, H. (2014). Nicotine content of electronic cigarettes, its release in vapour and its consistency across batches: regulatory implications. *Addiction*, 109(3):500–507.

Goniewicz, M. L., Knysak, J., Gawron, M., Kosmider, L., Sobczak, A., Kurek, J., Prokopowicz, A., Jablonska-Czapla, M., Rosik-Dulewska, C., Havel, C., et al. (2013). Levels of selected carcinogens and toxicants in vapour from electronic cigarettes. *Tobacco control*, pages tobaccocontrol–2012.

Guilmette, R. A., Wicks, J. D., and Wolff, R. K. (1989). Morphometry of human nasal airways in vivo using magnetic resonance imaging. *Journal of Aerosol Medicine*, 2(4):365–377.

Gupta, D. and Peters, M. H. (1985). A brownian dynamics simulation of aerosol deposition onto spherical collectors. *Journal of Colloid and Interface Science*, 104(2):375–389.

Haghnegahdar, A. and Feng, Y. (2017). The translocation of nicotine from human lung to systemic regions due to e-cigarette aerosol inhalation: a numerical study. *5th International Conference on Computational and Mathematical Biomedical Engineering (CMBE), Pittsburgh, PA, USA.*

Haghnegahdar, A., Feng, Y., Chen, X., and Lin, J. (2018). Computational analysis of deposition and translocation of inhaled nicotine and acrolein in the human body with e-cigarette puffing topographies. *Aerosol Science and Technology*, 52(5):483–493.

Hamborsky, J., Kroger, A., Wolfe, S., for Disease Control, C., Prevention, et al.

(2015). *Epidemiology and prevention of vaccine-preventable diseases.* US Department of Health & Human Services, Centers for Disease Control and Prevention.

Han, Z., Weng, W., and Huang, Q. (2013). Characterizations of particle size distribution of the droplets exhaled by sneeze. *Journal of The Royal Society Interface*, 10(88):20130560.

Hancioglu, B., Swigon, D., and Clermont, G. (2007). A dynamical model of human immune response to influenza a virus infection. *Journal of theoretical biology*, 246(1):70–86.

Handel, A., Longini Jr, I. M., and Antia, R. (2007). Neuraminidase inhibitor resistance in influenza: assessing the danger of its generation and spread. *PLoS Computational Biology*, 3(12):e240.

Hayden, F. G., Fritz, R., Lobo, M. C., Alvord, W., Strober, W., and Straus, S. E. (1998). Local and systemic cytokine responses during experimental human influenza a virus infection. relation to symptom formation and host defense. *The Journal of clinical investigation*, 101(3):643–649.

Hayden, F. G., Treanor, J. J., Betts, R. F., Lobo, M., Esinhart, J. D., Hussey, E. K., et al. (1996). Safety and efficacy of the neuraminidase inhibitor gg167 in experimental human influenza. *Journal of the American Medical Association*, 275(4):295–299.

Hinds, W. C. (2012). *Aerosol technology: properties, behavior, and measurement of airborne particles.* John Wiley & Sons.

Holder, B. P. and Beauchemin, C. A. (2011). Exploring the effect of biological delays in kinetic models of influenza within a host or cell culture. *BMC Public Health*, 11(1):S10.

Hufford, M. M., Richardson, G., Zhou, H., Manicassamy, B., García-Sastre, A., Enelow, R. I., and Braciale, T. J. (2012). Influenza-infected neutrophils within the infected lungs act as antigen presenting cells for anti-viral cd8+ t cells. *PloS one*, 7(10):e46581.

ICRP (1994). Human respiratory tract model for radiological protection. *ICRP publication 66. Annals of the ICRP*, 24:1–3.

ISO (2015). Human respiratory tract model for radiological protection. *ISO/TR 19478-2. ISO and Health Canada intense smoking parameters - Part 2: Examination of factors contributing to variability in the routine measurement of TPM, water and NFDPM smoke yields of cigarettes.*

Jayaraju, S., Brouns, M., Lacor, C., Belkassem, B., and Verbanck, S. (2008). Large eddy and detached eddy simulations of fluid flow and particle deposition in a human mouth–throat. *Journal of Aerosol Science*, 39(10):862–875.

Kane, L. E. and Alarie, Y. (1978). Evaluation of sensory irritation from acrolein-formaldehyde mixtures. *The American Industrial Hygiene Association Journal*, 39(4):270–274.

Kimbell, J., Gross, E., Joyner, D., Godo, M., and Morgan, K. (1993). Application of computational fluid dynamics to regional dosimetry of inhaled chemicals in the upper respiratory tract of the rat. *Toxicology and applied pharmacology*, 121(2):253–263.

Kimbell, J., Overton, J., Subramaniam, R., Schlosser, P., Morgan, K., Conolly, R., and Miller, F. (2001). Dosimetry modeling of inhaled formaldehyde: binning nasal flux predictions for quantitative risk assessment. *Toxicological Sciences*, 64(1):111–121.

Kimbell, J. S. and Subramaniam, R. P. (2001). Use of computational fluid dynamics models for dosimetry of inhaled gases in the nasal passages. *Inhalation Toxicology*, 13(5):325–334.

Klager, S., Vallarino, J., MacNaughton, P., Christiani, D. C., Lu, Q., and Allen, J. G. (2017). Flavoring chemicals and aldehydes in e-cigarette emissions. *Environmental science & technology*, 51(18):10806–10813.

Kleinstreuer, C. and Feng, Y. (2013). Lung deposition analyses of inhaled toxic aerosols in conventional and less harmful cigarette smoke: a review. *International journal of environmental research and public health*, 10(9):4454–4485.

Klenk, H.-D., Matrosovich, M., and Stech, J. (2008). Avian influenza: Molecular mechanisms of pathogenesis and host range. *Animal Viruses: Molecular Biology*, page 253.

Knight, V. (1980). Viruses as agents of airborne contagion. *Annals of the New York Academy of Sciences*, 353(1):147–156.

Korteweg, C. and Gu, J. (2008). Pathology, molecular biology, and pathogenesis of avian influenza a (h5n1) infection in humans. *The American journal of pathology*, 172(5):1155–1170.

Kreidenweis, S., Koehler, K., DeMott, P., Prenni, A., Carrico, C., and Ervens, B. (2005). Water activity and activation diameters from hygroscopicity data-part i: Theory and application to inorganic salts. *Atmospheric Chemistry and Physics*, 5(5):1357–1370.

Kreyling, W., Hodgson, A., Guilmette, R., Scarlett, C., Badmin, A., and Stradling, G. (1998). Interspecies comparison of lung clearance using monodisperse terbium oxide particles. *Radiation protection dosimetry*, 79(1-4):241–243.

Kutzman, R. S., Popenoe, E. A., Schmaeler, M., and Drew, R. T. (1985). Changes in rat lung structure and composition as a result of subchronic exposure to acrolein. *Toxicology*, 34(2):139–151.

Kutzman, R. S., Wehner, R. W., and Haber, S. B. (1984). Selected responses of hypertension-sensitive and resistant rats to inhaled acrolein. *Toxicology*, 31(1):53–65.

Kyerematen, G. A., Morgan, M. L., Chattopadhyay, B., Bethizy, J. D., and Vesell, E. S. (1990). Disposition of nicotine and eight metabolites in smokers and non-smokers: identification in smokers of two metabolites that are longer lived than cotinine. *Clinical Pharmacology & Therapeutics*, 48(6):641–651.

Lambert, A. R., O'shaughnessy, P. T., Tawhai, M. H., Hoffman, E. A., and Lin, C.-L. (2011). Regional deposition of particles in an image-based airway model: large-eddy simulation and left-right lung ventilation asymmetry. *Aerosol Science and Technology*, 45(1):11–25.

Lange, E., Kalthoff, D., Blohm, U., Teifke, J. P., Breithaupt, A., Maresch, C., Starick, E., Fereidouni, S., Hoffmann, B., Mettenleiter, T. C., et al. (2009). Pathogenesis and transmission of the novel swine-origin influenza virus a/h1n1 after experimental infection of pigs. *Journal of General Virology*, 90(9):2119–2123.

Langtry, R. B. and Menter, F. R. (2009). Correlation-based transition modeling for unstructured parallelized computational fluid dynamics codes. *AIAA journal*, 47(12):2894–2906.

Larson, E. W., Dominik, J. W., Rowberg, A. H., and Higbee, G. A. (1976). Influenza virus population dynamics in the respiratory tract of experimentally infected mice. *Infection and immunity*, 13(2):438–447.

Le, D., Miller, J. D., and Ganusov, V. V. (2015). Mathematical modeling provides kinetic details of the human immune response to vaccination. *Frontiers in cellular and infection microbiology*, 4:177.

Lee, H. Y., Topham, D. J., Park, S. Y., Hollenbaugh, J., Treanor, J., Mosmann, T. R., Jin, X., Ward, B. M., Miao, H., Holden-Wiltse, J., et al. (2009). Simulation and prediction of the adaptive immune response to influenza a virus infection. *Journal of virology*, 83(14):7151–7165.

Li, A. and Ahmadi, G. (1992). Dispersion and deposition of spherical particles from point sources in a turbulent channel flow. *Aerosol science and technology*, 16(4):209–226.

Li, W., Montassier, N., and Hopke, P. (1992). A system to measure the hygroscopicity of aerosol particles. *Aerosol science and technology*, 17(1):25–35.

Lisko, J. G., Tran, H., Stanfill, S. B., Blount, B. C., and Watson, C. H. (2015). Chemical composition and evaluation of nicotine, tobacco alkaloids, ph, and selected flavors in e-cigarette cartridges and refill solutions. *Nicotine & Tobacco Research*, 17(10):1270–1278.

Liu, L., Li, Y., Nielsen, P. V., Wei, J., and Jensen, R. L. (2017). Short-range airborne transmission of expiratory droplets between two people. *Indoor air*, 27(2):452–462.

Longest, P. W. and Vinchurkar, S. (2007). Validating cfd predictions of respiratory aerosol deposition: effects of upstream transition and turbulence. *Journal of biomechanics*, 40(2):305–316.

Lorensen, W. E. and Cline, H. E. (1987). Marching cubes: A high resolution 3d surface construction algorithm. In *ACM siggraph computer graphics*, volume 21, pages 163–169. ACM.

Ma, B. and Lutchen, K. R. (2009). Cfd simulation of aerosol deposition in an anatomically based human large–medium airway model. *Annals of biomedical engineering*, 37(2):271.

Male, D., Brostoff, J., Roth, D., and Roitt, I. (2006). *Immunology. 7th ed.* Elsevier.

Manigrasso, M., Buonanno, G., Fuoco, F. C., Stabile, L., and Avino, P. (2015). Aerosol deposition doses in the human respiratory tree of electronic cigarette smokers. *Environmental Pollution*, 196:257–267.

Margham, J., McAdam, K., Forster, M., Liu, C., Wright, C., Mariner, D., and Proctor, C. (2016). Chemical composition of aerosol from an e-cigarette: A quantitative comparison with cigarette smoke. *Chemical research in toxicology*, 29(10):1662–1678.

McAuley, T. R., Hopke, P., Zhao, J., and Babaian, S. (2012). Comparison of the effects of e-cigarette vapor and cigarette smoke on indoor air quality. *Inhalation toxicology*, 24(12):850–857.

McNeill, A., Brose, L., Calder, R., Hitchman, S., Hajek, P., and McRobbie, H. (2015). E-cigarettes: an evidence update. *Public Health England*, 3.

Menter, F., Langtry, R., and Völker, S. (2006a). Transition modelling for general purpose cfd codes. *Flow, turbulence and combustion*, 77(1):277–303.

Menter, F. R. (1994). Two-equation eddy-viscosity turbulence models for engineering applications. *AIAA journal*, 32(8):1598–1605.

Menter, F. R., Langtry, R. B., Likki, S., Suzen, Y., Huang, P., and Völker, S. (2006b). A correlation-based transition model using local variables—part i: model formulation. *Journal of turbomachinery*, 128(3):413–422.

Mikhailov, E., Vlasenko, S., Niessner, R., and Pöschl, U. (2004). Interaction of aerosol particles composed of protein and saltswith water vapor: hygroscopic growth and microstructural rearrangement. *Atmospheric Chemistry and Physics*, 4(2):323–350.

Miller, J. and Mitchell, G. (1969). Thymus and antigen-reactive cells. *Immunological Reviews*, 1(1):3–42.

Miller, R., Harstad, K., and Bellan, J. (1998). Evaluation of equilibrium and non-equilibrium evaporation models for many-droplet gas-liquid flow simulations. *International Journal of Multiphase Flow*, 24(6):1025–1055.

Mishra, A., Chaturvedi, P., Datta, S., Sinukumar, S., Joshi, P., and Garg, A. (2015). Harmful effects of nicotine. *Indian journal of medical and paediatric oncology: official journal of Indian Society of Medical & Paediatric Oncology*, 36(1):24.

Morris, J. B., HAssETT, D. N., and Blanchard, K. T. (1993). A physiologically based pharmacokinetic model for nasal uptake and metabolism of nonreactive vapors. *Toxicology and applied pharmacology*, 123(1):120–129.

Morris, P. B., Ference, B. A., Jahangir, E., Feldman, D. N., Ryan, J. J., Bahrami, H., El-Chami, M. F., Bhakta, S., Winchester, D. E., Al-Mallah, M. H., et al. (2015). Cardiovascular effects of exposure to cigarette smoke and electronic cigarettes. *Journal of the American College of Cardiology*, 66(12):1378–1391.

Nowak, M. and May, R. M. (2000). *Virus dynamics: mathematical principles of immunology and virology: mathematical principles of immunology and virology*. Oxford University Press, UK.

Oguin, T. H., Sharma, S., Stuart, A. D., Duan, S., Scott, S. A., Jones, C. K., Daniels, J. S., Lindsley, C. W., Thomas, P. G., and Brown, H. A. (2014). Phospholipase d facilitates efficient entry of influenza virus, allowing escape from innate immune inhibition. *Journal of Biological Chemistry*, 289(37):25405–25417.

Ou, C., Li, Y., Wei, J., Yen, H.-L., and Deng, Q. (2017). Numerical modeling of particle deposition in ferret airways: A comparison with humans. *Aerosol Science and Technology*, 51(4):477–487.

Pawelek, K. A., Huynh, G. T., Quinlivan, M., Cullinane, A., Rong, L., and Perelson, A. S. (2012). Modeling within-host dynamics of influenza virus infection including immune responses. *PLoS computational biology*, 8(6):e1002588.

Petrie, S. M., Guarnaccia, T., Laurie, K. L., Hurt, A. C., McVernon, J., and McCaw, J. M. (2013). Reducing uncertainty in within-host parameter estimates of influenza infection by measuring both infectious and total viral load. *PLoS One*, 8(5):e64098.

Pinilla, L. T., Holder, B. P., Abed, Y., Boivin, G., and Beauchemin, C. A. (2012). The h275y neuraminidase mutation of the pandemic a/h1n1 influenza virus lengthens the eclipse phase and reduces viral output of infected cells, potentially compromising fitness in ferrets. *Journal of virology*, 86(19):10651–10660.

Ramôa, C. P., Hiler, M. M., Spindle, T. R., Lopez, A. A., Karaoghlanian, N., Lipato, T., Breland, A. B., Shihadeh, A., and Eissenberg, T. (2015). Electronic cigarette nicotine delivery can exceed that of combustible cigarettes: a preliminary report. *Tobacco control*, pages tobaccocontrol–2015.

Ramsey, J. C. and Andersen, M. E. (1984). A physiologically based description of the inhalation pharmacokinetics of styrene in rats and humans. *Toxicology and applied pharmacology*, 73(1):159–175.

Rennie, C. E., Gouder, K. A., Taylor, D. J., Tolley, N. S., Schroter, R. C., and Doorly, D. J. (2011). Nasal inspiratory flow: at rest and sniffing. In *International forum of allergy & rhinology*, volume 1, pages 128–135. Wiley Online Library.

Robinson, D. E., Balter, N. J., and Schwartz, S. L. (1992). A physiologically based pharmacokinetic model for nicotine and cotinine in man. *Journal of pharmacokinetics and biopharmaceutics*, 20(6):591–609.

Robinson, R., Hensel, E., Morabito, P., and Roundtree, K. (2015). Electronic cigarette topography in the natural environment. *PLoS One*, 10(6):e0129296.

Rosenbaum, S. E. (2016). *Basic pharmacokinetics and pharmacodynamics: An integrated textbook and computer simulations*. John Wiley & Sons.

Schaffer, F., Soergel, M., and Straube, D. (1976). Survival of airborne influenza virus: effects of propagating host, relative humidity, and composition of spray fluids. *Archives of virology*, 51(4):263–273.

Scharfman, B., Techet, A., Bush, J., and Bourouiba, L. (2016). Visualization of sneeze ejecta: steps of fluid fragmentation leading to respiratory droplets. *Experiments in Fluids*, 57(2):24.

Scheinherr, A., Bailly, L., Boiron, O., Lagier, A., Legou, T., Pichelin, M., Caillibotte, G., and Giovanni, A. (2015). Realistic glottal motion and airflow rate during human breathing. *Medical engineering & physics*, 37(9):829–839.

Schroeter, J. D., Asgharian, B., Price, O. T., Kimbell, J. S., Kromidas, L., and Singal, M. (2016). Simulation of the phase change and deposition of inhaled semi-volatile liquid droplets in the nasal passages of rats and humans. *Journal of Aerosol Science*, 95:15–29.

Shahab, L., Goniewicz, M. L., Blount, B. C., Brown, J., McNeill, A., Alwis, K. U., Feng, J., Wang, L., and West, R. (2017). Nicotine, carcinogen, and toxin exposure in long-term e-cigarette and nicotine replacement therapy usersa cross-sectional studye-cigarettes and toxin exposure. *Annals of internal medicine*, 166(6):390–400.

Sharma, V. and McNeill, J. H. (2009). To scale or not to scale: the principles of dose extrapolation. *British journal of pharmacology*, 157(6):907–921.

Smith, A. M. and Perelson, A. S. (2011). Influenza a virus infection kinetics: quantitative data and models. *Wiley Interdisciplinary Reviews: Systems Biology and Medicine*, 3(4):429–445.

Smith, J., Van Ness, H., and Abbott, M. (1996). Chemical engineering thermodynamics. *Sat*, 18:1–3.

Steinhauer, D. A. (1999). Role of hemagglutinin cleavage for the pathogenicity of influenza virus. *Virology*, 258(1):1–20.

Struve, M. F., Wong, V. A., Marshall, M. W., Kimbell, J. S., Schroeter, J. D., and Dorman, D. C. (2008). Nasal uptake of inhaled acrolein in rats. *Inhalation toxicology*, 20(3):217–225.

Tamura, S.-i. and Kurata, T. (2004). Defense mechanisms against influenza virus infection in the respiratory tract mucosa. *Jpn J Infect Dis*, 57(6):236–47.

Tellier, R. (2009). Aerosol transmission of influenza a virus: a review of new studies. *Journal of the Royal Society Interface*, page rsif20090302.

Thompson, W. W., Weintraub, E., Dhankhar, P., Cheng, P.-Y., Brammer, L., Meltzer, M. I., Bresee, J. S., and Shay, D. K. (2009). Estimates of us influenza-associated deaths made using four different methods. *Influenza and other respiratory viruses*, 3(1):37–49.

Van Riel, D., Munster, V. J., De Wit, E., Rimmelzwaan, G. F., Fouchier, R. A., Osterhaus, A. D., and Kuiken, T. (2006). H5n1 virus attachment to lower respiratory tract. *Science*, 312(5772):399–399.

Wang, G.-W., Guo, Y., Vondriska, T. M., Zhang, J., Zhang, S., Tsai, L. L., Zong, N. C., Bolli, R., Bhatnagar, A., and Prabhu, S. D. (2008). Acrolein consumption exacerbates myocardial ischemic injury and blocks nitric oxide-induced pkcε signaling and cardioprotection. *Journal of molecular and cellular cardiology*, 44(6):1016–1022.

Wang, Y., James, P., et al. (1999). On the effect of anisotropy on the turbulent dispersion and deposition of small particles. *International Journal of Multiphase Flow*, 25(3):551–558.

Ward, C., Dempsey, M., Ring, C., Kempson, R., Zhang, L., Gor, D., Snowden, B., and Tisdale, M. (2004). Design and performance testing of quantitative real time pcr assays for influenza a and b viral load measurement. *Journal of Clinical Virology*, 29(3):179–188.

Weise, T. (2009). Global optimization algorithms-theory and application. *Self-published*, 2.

Whitaker, S. (1972). Forced convection heat transfer correlations for flow in pipes, past flat plates, single cylinders, single spheres, and for flow in packed beds and tube bundles. *AIChE Journal*, 18(2):361–371.

(WHO), W. H. O. (2012). Standard operating procedure for intense smoking of cigarettes.

Wilcox, D. C. et al. (1998). *Turbulence modeling for CFD*, volume 2. DCW industries La Canada, CA.

Worth Longest, P. and Xi, J. (2008). Condensational growth may contribute to the enhanced deposition of cigarette smoke particles in the upper respiratory tract. *Aerosol Science and Technology*, 42(8):579–602.

Yang, W., Elankumaran, S., and Marr, L. C. (2011). Concentrations and size distributions of airborne influenza a viruses measured indoors at a health centre, a day-care centre and on aeroplanes. *Journal of the Royal Society Interface*, page rsif20100686.

Yang, W. and Marr, L. C. (2011). Dynamics of airborne influenza a viruses indoors and dependence on humidity. *PloS one*, 6(6):e21481.

Yang, W. and Marr, L. C. (2012). Mechanisms by which ambient humidity may affect viruses in aerosols. *Appl. Environ. Microbiol.*, 78(19):6781–6788.

Zens, K. D. (2017). *Generation of T Cell Responses and Immunological Memory Following Influenza Infection and Vaccination in Early Life and Adulthood*. Columbia University.

Zhang, Z., Kim, C. S., and Kleinstreuer, C. (2006). Water vapor transport and its effects on the deposition of hygroscopic droplets in a human upper airway model. *Aerosol Science and Technology*, 40(1):1–16.

Zhang, Z. and Kleinstreuer, C. (2003). Low-reynolds-number turbulent flows in locally constricted conduits: a comparison study. *AIAA journal*, 41(5):831–840.

Zhang, Z., Kleinstreuer, C., and Feng, Y. (2012a). Vapor deposition during cigarette smoke inhalation in a subject-specific human airway model. *Journal of Aerosol Science*, 53:40–60.

Zhang, Z., Kleinstreuer, C., and Hyun, S. (2012b). Size-change and deposition of conventional and composite cigarette smoke particles during inhalation in a subject-specific airway model. *Journal of Aerosol Science*, 46:34–52.

APPENDIX A

ANSYS fluent user-defined functions (UDF) for the post-deposition calculation of formaldehyde in the human nasal cavity.

```
/**********************************************************************
Copyright (C) 2018, Ahmadreza Haghnegahdar
Department of Chemical Engineering
Oklahoma State University, Stillwater, OK

Project:
    Computational Fluid Particle Dynamics + Physiologically Based
        Toxicokinetic model V.2 > [tissue and blood layers]
        To calculate the absorption and translation of Formaldehyde

Macros/Functions:
    [UDM_names] assigns the user-memory names.
    [MixedBC_Form] defines the thermodynamic equilibrium between the gas mixture
        in airways and the chemical concentration in the epithelium.
    [CFPD_PBTK_v_2_FORM] do the in tissue calculation and save the data.
    [tridiagonal] the tridiagonal matrix to solve the partial differential
        equation (PDE).

Developer:
Ahmadreza Haghnegahdar - AUG 2018
**********************************************************************/
#include "udf.h"
#include <stdio.h>
#include <stdlib.h>
```

```
#include <math.h>
#include "para.h"
#include "sg.h" /* for the secondary gradient source macro */

#define extra_memories 21 /* Number of previously reserved UDMs, +1 is in this UDF*/
#define ID_of_extended_wall 53 /*ID of the extended wall*/

/* Names enumerates of the user-defined scalars*/
enum{
   PG, /*Propylene Glycol*/
   VG, /*Vegetable Glycerin*/
   NIC,   /*Nicotine*/
   FORM,  /*Formaldehyde*/
   ACR,  /*Acrolein*/
   DIACYL  /*Diacetyl*/
};
/* Store data in UDMI s*/
/*
Region    Airway ||       Tissue       ||        Blood       ||
d_index          ||   0 | 1 | ... | 49  || 50 | 51 | ... | 149 ||
NODE      C_air  ||    0| 2 | ... | 50 || 51 | 52 | ... | 150 ||
UDMI        UDSI ||   21| 22| ... | 70  || 71 | 72 | ... | 170 ||
*/
/*********************** Formaldehyde ****************/
/* Formaldheyde has 150+30=80 UDMI after those defined for Diacetyl */
#define x_steps_t 150 /*It cannot be lower than 4.3667=(xt_max/xb_max) times of x_steps_b*/
#define x_steps_b 30
#define n (x_steps_t + x_steps_b)
#define xt_max 6.55e-5          /* tissue thickness [m]*/
#define xb_max 1.5e-5           /* blood thickness [m]*/
#define deltax_t ((xt_max - 0.) / (real)x_steps_t)
```

```
#define deltax_b deltax_t       /*(xb_max / (real)x_steps_b)*/
#define P_t_air_form 101.5 /* tissue:air partition coefficient [m3/m3] */

DEFINE_EXECUTE_ON_LOADING(UDM_names, libname)
{
   /*Formaldehyde*/
   Set_User_Memory_Name(n + extra_memories, "Face [UDSI*rho*P_form/deltax^2]");
   for (i = n + extra_memories + 1; i < 2*n + extra_memories + 1; i++)
   {
      const char tissue[] = "Tissue_F: ";
      const char blood[] = "Blood_F: ";
      char tissue_print[FILENAME_MAX];
      char blood_print[FILENAME_MAX];
      if (i < n + extra_memories + 1 + x_steps_t)
      {
         sprintf(tissue_print, "%s%d", tissue, (i - (n + extra_memories + 1)));
         Set_User_Memory_Name(i, tissue_print);
      }
      else
      {
         sprintf(blood_print, "%s%d", blood, i - (n + extra_memories + 1) -
             x_steps_t);
         Set_User_Memory_Name(i, blood_print);
      }
   }
   Set_User_Scalar_Name(0, "PG");
   Set_User_Scalar_Name(1, "VG");
   Set_User_Scalar_Name(2, "NIC");
   Set_User_Scalar_Name(3, "FORM");
   Set_User_Scalar_Name(4, "ACR");
   Set_User_Scalar_Name(5, "DIACYL");
   Message0("\nUDMIs and UDSIs are titled.\n");
}
```

```
DEFINE_PROFILE(MixedBC_Form, thread, nv)
{
   face_t f;
   Thread *t0 = thread->t0;
   real A[ND_ND], dG[ND_ND], dr0[ND_ND], es[ND_ND], dr, A_by_es;
   real absrp;
   absrp = 8.07e+7;   /* 1/m */
   /*C_UDSI_DIFF(c, t, FORM) */
   real Af;
   real beta0, gamma;
   real temp1, temp2;
   if (!Data_Valid_P() || !FLUID_THREAD_P(t0)) return;   /* Do nothing if areas
       are not computed yet or not next to fluid. */
   begin_f_loop(f, thread)
   {
      cell_t c0 = F_C0(f, thread);    /* identify the cell thread adjacent to the
          face thread f */
      if (N_TIME == 0) /*initialization*/
      {
         C_UDMI(c0, t0, n + extra_memories) = 0.0;
      }
      BOUNDARY_FACE_GEOMETRY(f, thread, A, dr, es, A_by_es, dr0);
      Af = NV_MAG(A);
      gamma = 1.;
      if (NULLP(T_STORAGE_R_NV(t0, SV_UDSI_G(FORM))))
         beta0 = 0; /* if gradient is not allocated and stored yet, bypass the
             following macro (it happens when case/data files are being read */
      else
         BOUNDARY_SECONDARY_GRADIENT_SOURCE(beta0, SV_UDSI_G(FORM), dG, es,
             A_by_es, gamma);
      /* temporary variables used in the profile expression */
      temp1 = gamma * A_by_es / dr;
```

```
    temp2 = absrp * Af;
    real delta_x = deltax_t / 2.;
    real Y_inf;
    if (N_TIME == 0)
    {
      Y_inf = 0.; /*It should be a fraction of the baseline*/
    }
    else if (N_TIME == 1)
    {
      Y_inf = (temp1*C_UDSI_M1(c0, t0, FORM) - beta0 + temp2 * Y_inf) / (temp2
          + temp1);
    }
    real Y0 = (temp1*C_UDSI(c0, t0, FORM) - beta0 + temp2 * Y_inf) / (temp2 +
        temp1);
    F_PROFILE(f, thread, nv) = Y0;
    real C0 = P_t_air_form * Y0 * C_R(c0, t0); /* Input from the CFPD model:
        mass fraction to concentration*/
    C_UDMI(c0, t0, n + extra_memories) = C0 / pow(delta_x, 2.); /*Input of the
        FEM at DEFINE_EXECUTE_AT_END*/
  }
  end_f_loop(f, thread)
}

DEFINE_EXECUTE_AT_END(CFPD_PBTK_v_2_FORM)
{
  /* Input data */
  /* Formaldehyde*/
  /* Airway(1), Epithelium + Mucus(2), Subepithelium(3) */

  /****************** General Input Data ******************/
  /*   Epithelium + Mucus   Subepithelium
  surface area(cm2)
  Oral      103.1   103.1
```

```
Pharyx / Larynx 100.0   100.0
Trachea       59.7    59.7
Main Bronchi  39.8    39.8
Bronchi + bronchiole 163.6 163.6
thickness(L, cm)
Oral       0.0065     0.0015
Pharyx / Larynx 0.0065     0.0015
Trachea       0.0066     0.0015
Main Bronchi  0.0066     0.0015
Bronchi + bronchioles 0.0066  0.0015
*/
real Q_b = 9.86766667e-5;          /* Cardiac output [m3/s]*/
real adjust3[3] = { 0.01,0.02,1. };   /*nose=1%, all(broncial& trachea)=2%,
    aleveoalr=100%*/
Q_b = Q_b * adjust3[1];
/***************** Epithelium + Mucus(2) *****************/

real V_maxC1 = 1.96e+4*1e-6;       /* reaction V_max [kg/m3/s]*/
real adjust1[3] = { 1., 1.41, 1.051 };  /* V_maxC1 nose, bronchioles, other */
V_maxC1 = V_maxC1 * adjust1[1];       /* Adjusted V_maxC1*/
real K_m1 = 201e-3;                /* reaction rate [Kg/m3]*/
real V_maxC2 = 0.             ;  /* reaction V_max [kg/m3/s]*/
real adjust2[3] = { 1, 3.81, 0.65 };  /* V_maxC2 nose, bronchioles, other */
V_maxC2 = V_maxC2 * adjust2[1];       /* Adjusted V_maxC2*/
real K_m2 = 1.;                    /* reaction rate [Kg/m3] - it should be
    zero, but doesnt matter as long as V_maxC2 is zero (Numerator)*/
real D_t = 2.6 / 60. * 1e-8;       /* tissue mass diffusivity [m2/s]*/
D_t = 8.08e-6;
real surfarea_t = 59.7e-4;         /* tissue surface area [m2]*/
real V_t = surfarea_t * xt_max;       /* volume of region [m3]*/
/****************** Subepithelium(3) *******************/
real P_b_t = 1.;                /* blood:tissue partition coefficient [m3/m3]
    */
```

```
real D_b = 1.62e-5;                /* blood mass diffusivity [m2/s]*/
real K_f = 1.8e-2;                 /* reactivity [1/s]*/
real K_b = 1.07e-7;                /* non specific binding [1/s]*/
real surfarea_b = surfarea_t;      /* blood surface area [m2]*/
real V_b = surfarea_b * xb_max;       /* volume of region [m3]*/
real delta_t = 0.05;            /*Just to avoid -INF for steady case*/
real guard_SU = 1.; /* Steady and Unsteady Guard in diagonal elements*/
if (RP_Get_Boolean("pressure/unsteady?")) /* if UNSTEADY case*/
{
  delta_t = CURRENT_TIMESTEP;        /* dt for unsteady; 1 for steady case*/
}
else                          /* if STEADY case*/
{
  guard_SU = 0.;
}

double a[n - 1];                /* Stack allocation*/
double b[n - 1];
double c[n - 1];
double d[n - 1];
double max_finder2[n - 1];

int i;
if (N_TIME == 0)                /* initialization*/
{
  for (i = 0; i < n; i++)
  {
    a[i] = 0.0;
    b[i] = 0.0;
    c[i] = 0.0;
    d[i] = 0.0;
    max_finder2[i] = 0.0;
  }
```

```
  }

  int myboolean = 0;
  int face_number = 0;

  Domain *domain = Get_Domain(1);
  face_t f;
  cell_t c0;
  Thread *thread, *t0;

#if !RP_HOST
  thread_loop_f(thread, domain)   /* loops over all face threads in a domain*/
  {
    if (THREAD_TYPE(thread) == THREAD_F_WALL && THREAD_ID(thread) !=
        ID_of_extended_wall) /* check if it is a wall */
               /* and exclude the extended_wall */
    {
      begin_f_loop(f, thread)
      {
        if (PRINCIPAL_FACE_P(f, thread))
        {
          c0 = F_C0(f, thread);   /* Get the cell id of cell adjacent to the
             face*/
          t0 = THREAD_T0(thread);  /* Get the Thread id of the cells adjacent
             to the face*/

          real C0_by_deltax = C_UDMI(c0, t0, n + extra_memories);

          if (N_TIME == 0)      /* initialization*/
          {
            for (i = n + extra_memories + 1; i < 2*n + extra_memories+1; i++)
            {
              C_UDMI(c0, t0, i) = 0.0;
```

```
   }
}
else
{
   for (i = n + extra_memories + 1; i < 2*n + extra_memories+1; i++)
   {
      d[i - (n + extra_memories +1)] = C_UDMI(c0, t0, i); /*
          Initlize from previous time_step*/
   }
}

for (i = 0; i < n; i++)
{
   if (i == 0)
   {
      a[i] = 0.;
      b[i] = 2.*D_t / pow(deltax_t, 2.) + K_f + K_b + V_maxC1 /
          (K_m1 + d[i])
         + V_maxC2 / (K_m2 + d[i]) + guard_SU / delta_t;
      c[i] = -D_t / pow(deltax_t, 2.);
   }
   else if (i < x_steps_t)
   {
      a[i] = -D_t / pow(deltax_t, 2.);
      b[i] = 2.*D_t / pow(deltax_t, 2.) + K_f + K_b + V_maxC1 /
          (K_m1 + d[i])
         + V_maxC2 / (K_m2 + d[i]) + guard_SU / delta_t;
      c[i] = -D_t / pow(deltax_t, 2.);
   }
   else if (i == x_steps_t)
   {
      a[i] = -D_t / pow(deltax_t, 2.);
      b[i] = (D_t / deltax_t + D_b / deltax_b) / ((deltax_t +
```

```
            deltax_b) / 2.) + K_f
           + K_b + V_maxC1 / (K_m1 + d[i]) + V_maxC2 / (K_m2 + d[i])
           + guard_SU / delta_t;
        c[i] = -D_t * P_b_t / deltax_b / ((deltax_t + deltax_b) / 2.);
    }
    else if (i == x_steps_t + 1)
    {
        a[i] = -D_b / P_b_t / deltax_t / ((deltax_t + deltax_b) / 2.);
        b[i] = 2.*D_b / pow(deltax_b, 2.) + K_f + K_b + Q_b / V_b +
            guard_SU / delta_t;
        c[i] = -D_b / pow(deltax_b, 2.);
    }
    else if (x_steps_t + 1 < i < x_steps_b)
    {
        a[i] = -D_b / pow(deltax_b, 2.);
        b[i] = 2.*D_b / pow(deltax_b, 2.) + K_f + K_b + Q_b / V_b +
            guard_SU / delta_t;
        c[i] = -D_b / pow(deltax_b, 2.);
    }
    else if (i == x_steps_b)
    {
        a[i] = -2.* D_b / pow(deltax_b, 2.);
        b[i] = 2.* D_b / pow(deltax_b, 2.) + K_f + K_b + Q_b / V_b +
            guard_SU / delta_t;
        c[i] = 0.;
    }
}
for (i = 0; i < n; i++)
{
    if (i == 0)
    {
        d[i] /= delta_t;
        d[i] += D_t * C0_by_deltax;
```

```
                  }
                  else
                  {
                     d[i] /= delta_t;
                  }
               }

               tridiagonal(a, b, c, d, n);
               if ((n - 1) != sizeof(d) / sizeof(*d)) /* Check if [d] length has
                   changed*/
               {
                  myboolean = 1;
                  face_number++;
               }
               for (i = 0 + n + extra_memories + 1; i < 2*n + extra_memories+1; i++)
               {
                  C_UDMI(c0, t0, i) = d[i - (n + extra_memories + 1)];

                  if (C_UDMI(c0, t0, i) > max_finder2[i - (n + extra_memories + 1)])
                     max_finder2[i - (n + extra_memories + 1)] = C_UDMI(c0, t0, i);
               }
            }
         }
         end_f_loop(f, thread)
      }
      if (myboolean == 1)
      {
         CX_Message("\n Error! [d] dimensions mismatch. Tridiag input had size of:
             %i, but output has size of : %i at %i faces of Thread %i.",
            (n - 1), sizeof(d) / sizeof(*d), face_number, THREAD_ID(thread));
      }
      myboolean = 0;
   }
```

```
#endif

#if !RP_HOST
   /*Print MAX face -in tissue layers at each time step in a text file*/
   for (i = 0 + (n + extra_memories + 1); i < 2*n + extra_memories +1; i++)
   {
      max_finder2[i - (n + extra_memories + 1)] = PRF_GRSUM1(max_finder2[i - (n +
          extra_memories + 1)]);
   }
#endif
   for (i = 0 + (n + extra_memories + 1); i < 2*n + extra_memories +1; i++)
   {
      node_to_host_real_1(max_finder2[i - (n + extra_memories + 1)]);
   }

#if !RP_NODE
   FILE *svfile2;
   if (N_TIME == 0)
   {
      svfile2 = fopen("MAX_FACE_form.txt", "wb");  /* to clear the previous file*/
      fclose(svfile2);
   }
   svfile2 = fopen("MAX_FACE_form.txt", "a");      /* appending */
   if (N_TIME == 0)
   {
      for (i = 0 + (n + extra_memories + 1); i < 2*n + extra_memories +1; i++)
      {
         if (i == 0 + extra_memories)
         {
            fprintf(svfile2, "Time %i", i - (n + extra_memories + 1));
         }
         else
         {
```

```
            fprintf(svfile2, " %i", i - (n + extra_memories + 1));
         }
      }
      fprintf(svfile2, "\n");
   }

   for (i = 0 + (n + extra_memories + 1); i < 2*n + extra_memories + 1; i++)
   {
      if (i == 0 + (n + extra_memories + 1))
      {
         fprintf(svfile2, "%llu %e", N_TIME, max_finder2[i - (n + extra_memories +
             1)]);
      }
      else
      {
         fprintf(svfile2, " %e", max_finder2[i - (n + extra_memories + 1)]);
      }
   }
   fprintf(svfile2, "\n");
   fclose(svfile2);
#endif
   Message0("The Max face_formaldehyde UDMs are printed in the MAX_FACE_form.txt
       file.\n");
}

void tridiagonal(real* a, real* b, real* c, real* d, int num)
{
   /*Ahmadreza Haghnegahdar - 2018*/
   /*
   Inputs:
   n   - number of unknowns and equations (length of vector d)
   [d] - initially contains the vector [x from the previous time step] [0 : n-1]
   [a] - Subdiagonal [0 : n-2]
```

```
[b] - The main diagonal [0 : n-1]
[c] - Superdiagonal [0 : n-2]

Outputs:
[d] - The solution at the current time step [0 : n-1]
*/

/*
Example:
|b0 c0 0 0 ||x0|  |d0|
|a1 b1 c1 0 ||x1| _ |d1|
|0  a2 b2 c2||x2|   |d2|
|0  0  a3 b3||x3|  |d3|

1st row:
    b0x0 +     c0x1 = d0
->   x0 + (c0/b0)x1 = d0/b0
*->     x0 +     h0x1 = r0
where        h0 = c0/b0
             r0 = d0/b0

middle row (2nd):
a1x0 + b1x1 + c1x2 = d1
from 1st row: -(a1x0 + a1h0x1   = a1r0)
------------------------------
-> (b1 - a1h0)x1 + c1x2 = d1 - a1r0
*->         x1 + h1x2 = r1
where          h1 = c1/(b1 - a1h0)
               r1 = (d1 - a1r0)/(b1 - a1h0)

middle row (3rd):
a2x1 + b2x2 + c2x3 = d2
from 2nd row: -(a2x1 + a2h1x2   = a2r1)
```

```
------------------------------
-> (b2 - a2h1)x2 + c2x3 = d2 - a2r1
*->          x2 + h2x3 = r2
where          h2 = c2/(b2 - a2h1)
r2 = (d2 - a2r1)/(b2 - a2h1)

last row:
a3x2 + b3x3 = d3
from 3rd row:   -(a3x2 + a3h2x3 = a3r2)
------------------------------
->    (b3 - a3h2)x3 = d3 - a3r2
*->             x3 = r3
where         r3 = (d3 - a3r2)/(b3 - a3h2)



In this way: all subdiagonals are changed to zeros
all Main Diagonals are ones
all superdiagonals are h [0 : n-1]

Condition: ||bi|| > ||ai|| + ||ci||

in this version, c matrix is reused instead of hand d matrix is reused instead
    of r and x matrices to report results*/



int i;
for (i = 0; i < num; i++)
{
   if (i == 0)     /* For the first row*/
   {
      c[0] = c[0] / b[0]; /* h[0 : n-1] = c[0 : n-1] (one iteration behind) */
      d[0] = d[0] / b[0]; /* d[0 : n-1] = r[0 : n-1] (one iteration behind) */
   }
```

```
    else
    {
      c[i] = c[i] / (b[i] - a[i] * c[i - 1]);
      d[i] = (d[i] - a[i] * d[i - 1]) / (b[i] - a[i] * c[i - 1]);
    }
  }
  for (i = num - 2; i >= 0; i--) /*The back substitution */
  {             /* d[0 : n-1] = x[0 : n-1] (solution) (one iteration ahead) */
    d[i] -= c[i] * d[i + 1];
  }
}
```

APPENDIX B

ANSYS fuent text user interface (TUI) to modify the droplet minimum diameter and mass.

```
(rpsetvar 'dpm/lowest-diameter 1e-8)

(rpsetvar 'dpm/lowest-mass 1e-20)

(dpm-parameters-changed) /*execute to modify DPM settings*/

(models-changed)
```

APPENDIX C

ANSYS fuent UDF for realistic mouth breathing pattern.

```
/*********************************************************************
Copyright (C) 2018, Ahmadreza Haghnegahdar

Department of Chemical Engineering

Oklahoma State University, Stillwater, OK


  Realistic Mouth Breathing Pattern

  Reference: Scheinherra et al., 2015


Developer:

Ahmadreza Haghnegahdar - AUG 2018

*********************************************************************/

#include "udf.h"

#include <math.h>


#define inhalation_time 1.7606 /*sec*/

#define exhalation_time 4.0254 /*sec*/

DEFINE_PROFILE(MOUTH_realistic_breathing_pattern_uniform, thread, position)

{

  real x[ND_ND]; /*This will hold the position vector */

  real r;

  face_t f;

  real xc = 0.0; /*Coordinates of inlet circle center */

  real yc = 0.0;

  real zc = 0.0;

  real radius = 0.01; /*mouth-Inlet Radius > 1 cm */
```

```
real Area = 0.00010558566; /*m*/
real t_model = RP_Get_Real("flow-time");
real t_size = RP_Get_Real("physical-time-step");
double V_fit;
double Q_fit;
/*Defining the Breathing pattern profile - Fitting by polynimial (ploy1-9 are
compared and the one with lowest RMSE is selected)*/
/* The fitted curve is validated for 20 B_cycle with RMSE=0.66 > 20*4.0254
sec ~ 8 sec */
real a0 = -1.462;
real a1 = 19.55;
real b1 = 60.38;
real a2 = -10.9;
real b2 = -0.9638;
real a3 = -1.6;
real b3 = 7.435;
real a4 = -2.737;
real b4 = 1.096;
real a5 = -2.057;
real b5 = -0.4919;
real a6 = -0.4734;
real b6 = 0.7077;
real a7 = -0.4042;
real b7 = -0.8452;
real a8 = 0.08115;
real b8 = 0.6936;
real w = 1.561;
Q_fit = a0 + a1 * cos(t_model * w) + b1 * sin(t_model * w) + a2 * cos(2 *
    t_model * w) + b2 * sin(2 * t_model * w) + a3 * cos(3 * t_model * w) + b3 *
    sin(3 * t_model * w) + a4 * cos(4 * t_model * w) + b4 * sin(4 * t_model *
    w) + a5 * cos(5 * t_model * w) + b5 * sin(5 * t_model * w) + a6 * cos(6 *
    t_model * w) + b6 * sin(6 * t_model * w) + a7 * cos(7 * t_model * w) + b7 *
    sin(7 * t_model * w) + a8 * cos(8 * t_model * w) + b8 * sin(8 * t_model *
```

```
      w);
   V_fit = Q_fit * 0.001 / 60.0 / Area; /*to m^3, to sec*/

   begin_f_loop(f, thread)
   {
      /*
      /* parabolic inlet condition - for cylindrical mouth inlet */
      F_CENTROID(x, f, thread);
      r = sqrt(pow((x[0] - xc), 2) + pow((x[1] - yc), 2) + pow((x[2] - zc), 2));
      F_PROFILE(f, thread, position) = 2.0 * V_fit * (1.0 - pow(r, 2) /
      pow(radius, 2)); /*u fitted from >> 2*u_average = u_max */
      */
      /* uniform inlet condition - with exhalation time*/
      F_PROFILE(f, thread, position) = V_fit;
   }
   end_f_loop(f, thread)
}
```

APPENDIX D

ANSYS fluent UDF for realistic nasal breathing pattern.

```
/*********************************************************************
Copyright (C) 2018, Ahmadreza Haghnegahdar
Department of Chemical Engineering
Oklahoma State University, Stillwater, OK

   Realistic Nasal Breathing Pattern
   Reference: Rennie et al., 2011

Developer:
Ahmadreza Haghnegahdar - AUG 2018
**********************************************************************/
#include "udf.h"
#include <math.h>

#define inhalation_time 1.60 /*sec*/
#define exhalation_time 3.98 /*sec*/
DEFINE_PROFILE(NASAL_realistic_breathing_pattern_uniform, thread, position)
{
   real x[ND_ND]; /*This will hold the position vector */
   real r;
   face_t f;
   real xc = 0.0; /*Coordinates of inlet circle center */
   real yc = 0.0;
   real zc = 0.0;
   /*surface areas [m2]
```

```
inlet_nose_left:37 3.9244705e-05 /*left nostril */
inlet_nose_right : 39 3.9904616e-05 /*right nostril */
*/
real surf_average = (3.9244705e-05 + 3.9904616e-05) / 2.;
real t_model = RP_Get_Real("flow-time");
real t_size = RP_Get_Real("physical-time-step");
double V_fit;
double Q_fit;
/*It is valid between 0 to 3.98 sec >> after this do the loop*/
if (t_model > exhalation_time && t_model < exhalation_time * 2)
{
t_model = t_model - exhalation_time;
}
else if (t_model > exhalation_time * 2)
{
Message0("\nWARNING: The fitted profile is not valid for the times > 3.98*2
seconds.\n");
}
real a1 = 263.7;
real b1 = 0.6369;
real c1 = 3.015;
real a2 = 330.7;
real b2 = 0.1254;
real c2 = -3.727;
real a3 = 73.19;
real b3 = 4.86;
real c3 = -0.7755;
real a4 = 48.58;
real b4 = 7.822;
real c4 = -0.7588;
real a5 = 16.06;
real b5 = 13.33;
real c5 = 0.03013;
```

```
   real a6 = 253.6;
   real b6 = 2.011;
   real c6 = -0.4039;
   real a7 = 43.69;
   real b7 = 10.85;
   real c7 = -1.085;
   Q_fit = a1 * sin(b1*t_model + c1) + a2 * sin(b2*t_model + c2) + a3 *
       sin(b3*t_model + c3) + a4 * sin(b4*t_model + c4) + a5 * sin(b5*t_model +
       c5) + a6 * sin(b6*t_model + c6) + a7 * sin(b7*t_model + c7);
   V_fit = Q_fit * 1e-6 / surf_average; /*to m2/s*/
   begin_f_loop(f, thread)
   {
      /*
      /* parabolic inlet condition - for cylindrical mouth inlet */
      F_CENTROID(x, f, thread);
      r = sqrt(pow((x[0] - xc), 2) + pow((x[1] - yc), 2) + pow((x[2] - zc), 2));
      F_PROFILE(f, thread, position) = 2.0 * V_fit * (1.0 - pow(r, 2) /
      153
      pow(radius, 2)); /*u fitted from >> 2*u_average = u_max */
      */
      /* uniform inlet condition - with exhalation time*/
      F_PROFILE(f, thread, position) = V_fit;
   }
   end_f_loop(f, thread)
}
```

VITA

AHMADREZA HAGHNEGAHDAR

Candidate for the Degree of

Master of Science

Thesis: DEVELOPMENT OF A MULTISCALE NUMERICAL MODEL WITH TWO HUMAN PULMONARY HEALTH APPLICATIONS

Major Field: Chemical Engineering

Education:

Completed the requirements for the degree of Master of Science with a major in Chemical Engineering at Oklahoma State University, Stillwater, OK in December 2018.

Completed the requirements for the degree of Bachelor of Science with a major in Chemical Engineering at Shiraz University, Shiraz, Iran in June 2015.

Publications:

Haghnegahdar, A., Feng, Y., Chen, X., & Lin, J. (2018). Computational analysis of deposition and translocation of inhaled nicotine and acrolein in the human body with e-cigarette puffing topographies. Aerosol Science and Technology, 52(5), 483-493.

Feng, Y., Xu, Z., & **Haghnegahdar, A.** (2016). Computational Fluid-Particle Dynamics Modeling for Unconventional Inhaled Aerosols in Human Respiratory Systems. In Aerosols-Science and Case Studies. InTech.